Technische Universität München
Max-Planck-Institut für Quantenoptik

A Single-Photon Switch and Transistor based on Rydberg Blockade

Simon Elias Baur

Vollständiger Abdruck der von der Fakultät für Physik der Technischen Universität München zur Erlangung des akademischen Grades eines

Doktors der Naturwissenschaften (Dr. rer. nat.)

genehmigten Dissertation.

Vorsitzender:		Univ.–Prof. Dr. W. Zwerger
Prüfer der Dissertation:	1.	Hon.–Prof. Dr. G. Rempe
	2.	Univ.–Prof. Dr. M. Stutzmann
	3.	Prof. Ch. Adams, Ph.D., Durham University / UK (nur schriftliche Beurteilung)

Die Dissertation wurde am 30.09.2014 bei der Technischen Universität München eingereicht und durch die Fakultät für Physik am 04.05.2015 angenommen.

Abstract

This thesis reports the experimental realisation of a single-photon switch and transistor. To this end, Rydberg blockade in electromagnetically induced transparency (EIT) is used to create an interaction between two light pulses at the single photon level. In the experiment, a gate pulse containing one incoming photon on average is stored as a Rydberg excitation in an ultracold atomic gas using EIT. Subsequently a target light pulse is sent through the atomic ensemble. Without the gate pulse, the medium would be transparent due to EIT and the transmission would be high. If a gate excitation has been stored, however, Rydberg blockade suppresses the transmission of the target light pulse. The stored gate photon can be retrieved after the transmission of the target light. A retrieved photon heralds successful storage. In the corresponding postselected subensemble the transmission of the target light is reduced by an extinction factor of 0.05. This reduction is robust if the number of incoming gate photons or target photons is varied.

In a conceptually improved version of the experiment, a single-photon transistor is realised that shows a gain above unity. The gain quantifies the change in the transmitted target photon number per incoming gate photon. For one incoming gate photon on average, a gain of 20 is observed. The improved experiment uses a Förster resonance, the benefit of which becomes directly evident in an improved gain and extinction.

If a Rydberg excitation is created during the gate pulse, then the transmission of the target light pulse drops substantially. By setting a discrimination threshold for the number of detected target photons, it is possible to detect in a single shot with a fidelity of 86% whether a Rydberg excitation was created during the gate pulse. Since the gate excitation is not retrieved by the target light, this detection method is nondestructive.

Contents

1. Introduction

1.1. Switching with Single Photons

The transistor is the device that lies at the heart of signal processing. The invention of the electronic transistor [1–3] led to a remarkable development in computing over the past decades. Since the 1960s, the minimal energy cost of computation has been a prominent issue and power dissipation has been identified as one of the main limitations for increasing computational power [4–6]. Inspired by the prospect that optical technologies allow for high bandwidths at low power dissipation, the concept of an all-optical computer was born [7, 8]. The key requirement for many of the proposed designs is the availability of all-optical transistors [9, 10]. This creates a fundamental interest in the ultimate low-power limit of such a device which is reached when a single photon at the input of the transistor is sufficient to change the output of the transistor.

A single-photon transistor operates at the level of single quanta. It therefore marks the boundary between a world where classical physics suffices for the description of nature and a world that is governed by the rules of quantum physics. These quantum laws can provide us with capabilities that go beyond the possibilities of classical information processing. Arguably the first example of practical relevance was the quantum key distribution protocol BB84 which showed that quantum laws can be used for cryptography [11]. This laid the basis for research in the field of quantum communication [12]. Although some technologies that have emerged from this field have already been commercialised, the realisation of long distance quantum communication channels is still the subject of current research. In particular, the proposal that quantum repeaters could overcome the problem of light attenuation in optical fibres has attracted a great deal of attention [13].

Concurrent to the developments in the field of quantum communication, the idea of a quantum computer, that could be used to solve certain computational problems more efficiently than any classical computer, took shape [14]. The most famous example for such a problem is prime factorization that could be solved in polynomial time using Shor's algorithm on a quantum computer [15, 16]. Similarly, other quantum algorithms have been identified that promise to outperform their classical counterparts. Most notably, the Grover search algorithm was proven to be superior to any algorithm running on a classical computer [17]. For a historical account of the beginnings of quantum computing and communication see for example Ref. [18]

Various quantum systems are being investigated to determine their feasibility for quantum information purposes, including neutral atoms [19], ions [20], quantum dots in semiconductors [21], colour centres in diamond [22, 23], nuclear spins [24] and superconducting materials [25]. The aim of many of these experiments is to develop building blocks of a universal quantum computer [26]. The most prominent building block is the two qubit gate [27]. However, special-purpose quantum computers that can only serve for a limited range of applications are also being explored. A contentious example is that of a quantum annealer [28, 29], which is already commercially available.

Single photons also offer a possible platform for quantum information processing owing to some of their unique properties [30]. Due to their comparably weak coupling to the environment their quantum properties are well protected against decoherence. At the same time their degrees of freedom can be easily controlled using standard optical components. Two qubit gates for photons have already been realised [31–34] following a proposal to use linear optics and single ancillary photons [35]. However, inherently probabilistic schemes of this kind are very hard to scale to large systems [36]. By contrast, the realization of a deterministic quantum gate for photons is a goal that is yet to be achieved.

Traditionally, all-optical switching with a large number of photons has been dominated by methods from nonlinear optics like optical bistability [37] or nonlinear media in optical interferometers [38]. In recent years, considerable progress has been made towards lower light levels by using nonlinear optical waveguides and fibres [39–41]. Beyond classical nonlinear optics, other systems have emerged, that exhibit high optical nonlinearities even for relatively low photon numbers. For example, a single quantum emitter such as one molecule [42] can be very easily saturated and can therefore be used to create interactions between photons. In order to increase the coupling between the light and the quantum emitter, high finesse optical resonators are used in the field of cavity quantum electrodynamics [43]. Here, neutral atoms [44–46] or single quantum dots in solid state systems [47–49] serve as the quantum emitters.

A different avenue pursued in implementing photon-photon interactions is the use of atomic ensembles. Here, for instance, optical instabilities can be used for all-optical switching [50]. Many ideas, however, are based on electromagnetically induced transparency (EIT) [51], a phenomenon where a normally opaque medium is made transparent by the application of a laser field. EIT can be accompanied by a drastic change in group velocity, making it possible to generate slow and fast light. EIT is related to laser-induced coherent phenomena in 3-level atoms which have been studied since the 1960s (see e.g. Refs. [52, 53]) such as coherent population trapping [54, 55]. In 1991, EIT in optically thick samples was observed [56]. "This experiment has been often considered the starting point for ... [the development that] later prompted the beautiful demonstration of Slow and Fast Light" [53]. Related proposals predicted that large optical nonlinearities can be achieved with EIT [57–60]. By confining light into a hollow core fibre loaded with atoms, optical switching with ~ 100 photons could

be observed [61] using EIT. The drastic change in group velocity that can be created with EIT [62] can be used to efficiently convert light into an atomic excitation [63, 64]. An effective interaction between light pulses can then be created, for example, by elastic collisions between the atoms [65–67]. Similarly, normal mode splitting in an optical cavity can be used to implement an all-optical transistor. All-optical switching with 2.5 to 5 incoming photons was achieved in this way in a recent experiment [68].

1.2. Rydberg Blockade

A promising approach to single-photon switching, that has emerged recently and is employed in this thesis, is to combine EIT with the exaggerated properties of Rydberg atoms in order to create interactions between photons. Due to their large radius, Rydberg atoms are very sensitive to their environment and, in particular, to the presence of other Rydberg atoms. In fact, in rubidium the van der Waals interaction between two Rydberg atoms is typically enhanced by 20 orders of magnitude compared to two ground state atoms.

The exaggerated properties of Rydberg atoms compared to ground state atoms have been studied for a long time [69]. The seminal proposal [70] to use their long-range dipole-dipole interaction for implementing quantum gates between two neutral atoms generated a lot of new interest in Rydberg atoms [19]. The central idea is that two atoms which are close to each other cannot be simultaneously excited to a Rydberg state. This Rydberg blockade forms the basis of many other proposals. In particular, it has been established that quantum information processing using Rydberg blockade can also be performed in atomic ensembles [71]. In addition, it was suggested that Rydberg blockade can be used for the creation of single-atom and single-photon sources [72], the generation of many-particle entanglement [73–76] or the implementation of a quantum simulator [77].

Inspired by these prospects, a lot of experimental effort has been dedicated to studying Rydberg blockade. Rydberg blockade was first observed in 2004 as a suppression of excitation to Rydberg states in an atomic gas [78, 79] and later in sub-Poissonian atom counting statistics [80, 81]. Shortly afterwards, it was shown, that a Förster resonance can be used to enhance Rydberg blockade [82]. Furthermore, it was experimentally demonstrated that Rydberg blockade can be observed in the coherent excitation of Rydberg atoms [83–87]. In 2010, entanglement [88] and the first quantum gate for neutral atoms [89] was achieved using Rydberg atoms.

Early during this development, it was realised that EIT can be used to map the properties of Rydberg atoms onto light fields [71], thereby creating interactions between photons. Based on this, it was suggested that deterministic photonic quantum gates can be realised using Rydberg blockade in EIT [90–93]. In addition, correlated states of light can be generated [92, 94, 95].

The manner in which interactions between photons arise in EIT with Rydberg states can be understood with the following consideration. If a photon enters a medium that is made transparent by Rydberg EIT, it becomes a Rydberg polariton. This is a propagating excitation consisting of a photonic component and a Rydberg component. Since Rydberg atoms interact strongly with each other, Rydberg polaritons do so as well. As a consequence of the interaction, the medium becomes absorptive if more than one polariton propagates in it. The transmission of more than one photon is therefore blocked. This is the optical manifestation of Rydberg blockade.

The starting point of investigating interactions between Rydberg polaritons was the demonstration of EIT with Rydberg states [96]. This was followed by the first observation of Rydberg blockade in EIT in the form of a suppression of on-resonance EIT transmission [97]. Evidence for non-classical behaviour in Rydberg EIT was first given by the measurement of photon-antibunching [98–100] and later by the demonstration of photon-polariton entanglement [101]. Furthermore, in a correlation measurement of the transmitted light in Rydberg EIT a conditional phase shift and polarisation entanglement was observed [102].

1.3. This Thesis

During this thesis work, we used Rydberg blockade in EIT to implement the first single-photon switch [103]. This is an all-optical switch where a single gate photon suffices to switch the transmission of a target light pulse. To this end, a gate light pulse, containing one photon on average, is stored in an ultracold ensemble of ^{87}Rb atoms using EIT. In the absence of the gate pulse, the medium is transparent for a subsequent target light pulse due to EIT. However, if a gate excitation is stored, Rydberg blockade will suppress the transmission of the target light pulse. On average, we observe a reduction of the target transmission by a factor of 0.81. The stored gate photon can be retrieved from the atomic ensemble after the transmission of the target light. A retrieved photon heralds successful storage. The corresponding postselected subensemble shows a reduction of the transmission by a factor of 0.05.

For the realization of the single-photon switch, it was first necessary to characterise as well as improve EIT and storage of light with Rydberg states in our system. Furthermore, the observation of Rydberg blockade was a key step on the way to realising the single-photon switch. Rydberg blockade was verified by detecting photon-antibunching with $g^{(2)}(0) = 0.18$ and observing saturation effects in EIT.

In a conceptually improved experiment a single-photon transistor was demonstrated [104]. Like the single-photon switch, this device operates with one incoming gate photon. In addition, it shows a gain above unity.[1] Gain quantifies

[1] Note that a single-photon transistor does not violate the no-cloning theorem [105] despite the fact that it operates with single quanta of light and shows gain.

the change in the transmitted target photon number per incoming gate photon. Gain or fan-out is important for practical applications as it quantifies how many subsequent stages can be driven [10]. In addition to having gain, all-optical transistors should be cascadable [10], which means that the output of the transistor must be compatible with the input of the next stage. In the optical domain, this means that the gate and the target light have to be operated at the same wavelength.

The single-photon transistor presented in this thesis exhibits a gain of ~ 20 [104]. It benefits considerably from the use of a Förster resonance. Evidence for this is provided by experimental data showing that the gain is enhanced near the Förster resonance.

As a first application, the mechanism that forms the basis of the transistor is used for the nondestructive detection of a Rydberg excitation. Here we exploit that the successful storage of a gate photon in a Rydberg state leads to a large reduction in the detected target photon number. This allows us to estimate in a single shot with a fidelity of above 0.86 whether a Rydberg excitation was created during the gate pulse.

This thesis is organised as follows: Chap. 2 introduces the theoretical background of EIT and the storage of light, as well as Rydberg atoms. Chap. 3 describes the experimental apparatus. Chap. 4 is dedicated to various characterization measurements relating to EIT, storage of light in Rydberg states, and Rydberg blockade. In Chap. 5, experimental results demonstrating a single-photon switch are presented. Chap. 6 reports the experimental observation of a single-photon transistor exhibiting gain. Finally, Chap. 7 concludes with an outlook.

During an earlier stage of this thesis work, we experimentally studied the switching of light pulses with thousands of photons using four wave mixing in a Bose-Einstein condensate [67]. The results are extensively covered in a previous dissertation [106]. Therefore they are only briefly summarised in App. D.

2. Theoretical Background

This chapter discusses the theoretical foundations of the experiments presented in this thesis. Chap. 2.1 gives a short introduction into electromagnetically induced transparency (EIT) and the storage of light in ultra-cold atomic ensembles. Chap. 2.2 outlines important properties of Rydberg atoms. In addition, the dipole-dipole interaction between Rydberg atoms is discussed with regard to the performed experiments. At the end of this chapter the concept of Rydberg blockade is explained in the context of EIT.

2.1. Storage of Light using Electromagnetically Induced Transparency

Electromagnetically induced transparency (EIT) is a quantum interference effect which makes a normally opaque medium transparent due to the presence of a light field called control field. In addition the dispersive properties of the medium are strongly altered leading to a drastic slow down and compression of incoming light pulses (Chap. 2.1.1). By ramping the intensity of the control field to zero, a light pulse can be stored in the medium and retrieved at a later point in time (Chap. 2.1.2). This chapter largely follows Refs. [51, 63] with special emphasis on the differences to previous works at this experiment [107].

2.1.1. Electromagnetically Induced Transparency

The simplest system in which EIT can be observed is the three-level atom. Fig. 2.1(a) shows an energy level diagram in ladder configuration. It consists of a ground state $|g\rangle$, an excited state $|e\rangle$, and a second long-lived state $|r\rangle$. Population in the states $|e\rangle$ and $|r\rangle$ can decay by spontaneous emission with rates Γ_e and $\Gamma_r \ll \Gamma_e$. A control laser field with angular frequency ω_c couples the states $|e\rangle$ and $|r\rangle$. We study the propagation of a weak signal light field that is near resonant with the transition $|g\rangle \leftrightarrow |e\rangle$. As shown in Fig. 2.1(a) we introduce the detuning of the control and the signal light field, as well as the two-photon-detuning

$$\Delta_s = \omega_s - \omega_{eg}, \qquad \Delta_c = \omega_c - \omega_{re}, \qquad \delta_2 = \Delta_s + \Delta_c. \tag{2.1}$$

ω_{eg} and ω_{re} denote the angular frequencies of the transitions $|g\rangle \leftrightarrow |e\rangle$ and $|e\rangle \leftrightarrow |r\rangle$ respectively. The coupling of a light field to the atom can be expressed

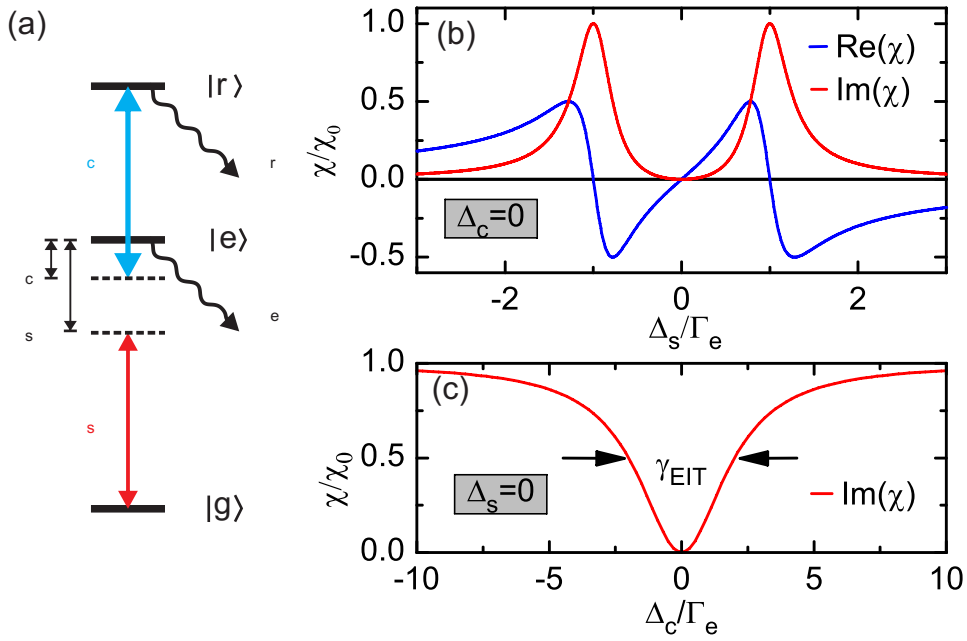

Figure 2.1.: (a) Three-level atom in ladder configuration. A strong coupling field with Rabi frequency Ω_c and detuning Δ_c couples state $|e\rangle$ and $|r\rangle$. A weak signal field with Rabi frequency Ω_s and detuning Δ_s drives the transition $|g\rangle \leftrightarrow |e\rangle$. The two-photon detuning is defined as $\delta_2 = \Delta_s + \Delta_c$. The states $|e\rangle$ and $|r\rangle$ decay by spontaneous emission with rates Γ_e and Γ_r. (b) Susceptibility χ as a function of signal detuning Δ_s for $|\Omega_c| = 2\Gamma_e$ and $\Delta_c = 0$. At $\Delta_s = \delta_2 = 0$, χ is zero and the slope of $\mathrm{Re}(\chi)$ is positive. The signal pulse experiences normal dispersion and and can be slowed down in the medium. (c) Susceptibility χ as a function of control detuning Δ_c for $|\Omega_c| = 2\Gamma_e$ and $\Delta_s = 0$. The FWHM of the line is call EIT linewidth γ_{EIT}.

by the Rabi frequency $\Omega = \boldsymbol{d}_{ij}\boldsymbol{\epsilon}\mathcal{E}/\hbar$. Here $\boldsymbol{d}_{ij}$ denotes the electric dipole matrix element of the transition $|i\rangle \leftrightarrow |j\rangle$, $\boldsymbol{\epsilon}$ the polarisation vector and $\mathcal{E}$ the complex amplitude of the electric field. In an interaction picture and using the rotating wave approximation we obtain the Hamiltonian in a matrix representation with respect to the basis $\{|g\rangle, |e\rangle, |r\rangle\}$ in analogy to Ref. [51]

$$H = -\frac{\hbar}{2}\begin{pmatrix} 0 & \Omega_s^* & 0 \\ \Omega_s & 2\Delta_s & \Omega_c^* \\ 0 & \Omega_c & 2\delta_2 \end{pmatrix}. \tag{2.2}$$

The normalised state

$$|D\rangle \propto \Omega_c^*|g\rangle - \Omega_s|r\rangle \tag{2.3}$$

is obviously an eigenstate of Eq. (2.2) for $\delta_2 = 0$. Since it does not overlap with the fast decaying state $|e\rangle$ it is called a dark state.

In a typical EIT experiment all atoms are initially prepared in state $|g\rangle$ and no light fields are applied at the beginning. Switching on the control field couples

the unpopulated states $|e\rangle$ and $|r\rangle$. The population remains in state $|g\rangle$. For $\Omega_s = 0$ the state $|g\rangle$ is identical to $|D\rangle$. If the signal light pulse enters the medium with slowly varying amplitude, the population adiabatically follows the state $|D\rangle$. As the system remains in the dark state the signal pulse does not experience any absorption. This is known as electromagnetically induced transparency. As long as the two-photon resonance condition $\delta_2 = 0$ is fulfilled, this result does not depend on Δ_c or Ω_c.

To describe the propagation of a signal light pulse in a medium with particle density ϱ we study the electric susceptibility χ. Adiabatic elimination of the weakly populated states $|e\rangle$ and $|r\rangle$ in analogy with Ref. [51] yields an expression[1] for the linear susceptibility

$$\chi = \chi_0 \gamma_{eg} \frac{i(\gamma_{rg} - 2i\delta_2)}{|\Omega_c|^2 + (\gamma_{rg} - 2i\delta_2)(\gamma_{eg} - 2i\Delta_s)}. \tag{2.4}$$

Here we use

$$\chi_0 = \frac{2\varrho |\boldsymbol{d}_{eg}|^2}{\epsilon_0 \hbar \Gamma_e} \tag{2.5}$$

where $\boldsymbol{d}_{eg}$ is the electric dipole matrix element of the signal transition. γ_{rg} describes the dephasing of the states $|g\rangle$ and $|r\rangle$, i.e. a contribution to the time evolution of the density matrix given by $\dot{\rho}_{rg} = -\gamma_{rg}\rho_{rg}/2$. Analogously, $\gamma_{eg} = \Gamma_e + \gamma_{\mathrm{e,dephas}}$ determines the decay of ρ_{eg}, where $\gamma_{\mathrm{e,dephas}}$ accounts for the dephasing of the state $|e\rangle$. Strictly speaking, this is only true for Markovian dephasing that can be described by coupling to a thermal bath [51]. However, it is possible to include finite laser linewidths for Lorentzian line shapes by replacing[2] $\gamma_{rg} \to \gamma_{rg} + \gamma_s + \gamma_c$ and $\gamma_{eg} \to \gamma_{eg} + \gamma_s$ [108] . Here, γ_s and γ_c are the full width at half maximum (FWHM) linewidths of the probe and the control light, respectively. Further it is assumed that there are no correlations between the noise of the two lasers. In the remainder of this chapter, we neglect dephasing, i.e. $\gamma_{rg} = 0$ and $\gamma_{eg} = \Gamma_e$

Fig. 2.1(b) shows the real and imaginary part of χ as a function of the signal detuning Δ_s for the case $\Delta_c = 0$. χ is zero at $\delta_2 = \Delta_s = 0$. Consequently the medium is transparent. This is strictly true for a monochromatic light field. However for a light pulse with a typical duration of the temporal envelope $\Delta\tau_s$, the Fourier limit requires that the pulse has a frequency distribution $\Delta\omega_s$ with

$$\Delta\tau_s \Delta\omega_s \geq 1. \tag{2.6}$$

Hence it is necessary to analyse χ not only at $\delta_2 = 0$, but also in the vicinity of the two-photon resonance.

[1] Formulas in Ref. [51] are for the Λ system. Expressions for the ladder configuration are obtained by replacing $\Delta_c \to -\Delta_c$ and $\Omega_c \to \Omega_c^*$. The sign of $\mathrm{Re}(\chi)$ in Ref. [51] is probably a misprint.

[2] This corresponds to the convolution of χ with two Lorentzians with FWHM of γ_s and γ_c. This is an approximation that, for example, accounts for shot to shot fluctuation of the laser frequencies. Note, that the linewidths in Ref. [108] are half width at half maximum.

To estimate the width of the frequency window with low absorption we expand $\mathrm{Im}(\chi)$ in δ_2 around zero up to the second order. The transmission of the signal intensity through a medium of length L is then given by

$$T = \exp\left(-k_p L \ \mathrm{Im}(\chi)\right) \approx \exp\left(-\frac{4\delta_2^2}{\Delta\omega_{\mathrm{trans}}^2}\right), \quad \Delta\omega_{\mathrm{trans}} = \frac{|\Omega_c|^2}{\sqrt{\Gamma_{eg}\Gamma_e \cdot OD_{\mathrm{cyc}}}}. \tag{2.7}$$

Close to the two-photon resonance, the transmission profile can be approximated by a Gaussian with FWHM of $\Delta\omega_T = \Delta\omega_{\mathrm{trans}}\sqrt{\ln 2}$. Here $OD_{\mathrm{cyc}} = \varrho\sigma_{\mathrm{cyc}}L$ is the optical depth of the medium for a closed transition, $\sigma_{\mathrm{cyc}} = 3\lambda^2/2\pi$ the resonant scattering cross section and $\lambda = 2\pi/k_p$ the wavelength of the signal light. Consequently a signal light pulse with sufficiently narrow bandwidth $\Delta\omega_s \ll \Delta\omega_{\mathrm{trans}}$ can propagate almost without absorption in the medium.

In the context of Rydberg blockade, it is also interesting, how a detuning of the control field affects the transmission of the signal light at $\Delta_s = 0$. Fig. 2.1(c) shows the susceptibility as a function of Δ_c. The dip in $\mathrm{Im}(\chi)$ has a FWHM of

$$\gamma_{\mathrm{EIT}} = \frac{|\Omega_c|^2}{\Gamma_e} \tag{2.8}$$

which is called the single-atom EIT linewidth. Unlike $\Delta\omega_{\mathrm{trans}}$, γ_{EIT} is independent of the atomic density and the length of the medium and is thus useful for quantifying Rydberg blockade in EIT (cf. Chap. 2.2.6).

The group velocity v_{gr} of a light pulse on EIT resonance can be drastically reduced compared to the vacuum speed of light c if $d\,\mathrm{Re}(\chi)/d\omega_s$ is large. This effect is called *slow light*. Experimentally a reduction of the group velocity by 7 orders of magnitude was demonstrated [62]. At two-photon resonance we obtain from Eq. (2.4) [51]

$$v_{\mathrm{gr}} = \frac{c}{1+n_{\mathrm{gr}}}, \qquad \frac{1}{n_{\mathrm{gr}}} = \frac{|\Omega_c|^2}{c\varrho\sigma_{\mathrm{cyc}}\Gamma_{eg}} \tag{2.9}$$

with group index n_{gr}. Consequently the light pulse gets spatially compressed by a factor of v_{gr}/c on entering the medium. The temporal envelope of the light pulse remains unaffected. On leaving the medium the original light pulse is restored.

Further insight into the pulse propagation on two-photon resonance can be gained from a quasiparticle picture in which a signal light pulse propagating along the z direction can be described by a dark-state polariton [63]

$$\Psi(z,t) = \cos\vartheta\tilde{\mathcal{E}}_p(z,t) - \sin\vartheta\sqrt{\varrho}\rho_{rg}(z,t)e^{i\Delta kz} \tag{2.10}$$

with the mixing angle related to the group index v_{gr} by

$$\tan^2\vartheta = n_{\mathrm{gr}}. \tag{2.11}$$

Here $\tilde{\mathcal{E}}_p = \mathcal{E}_p/\sqrt{\hbar\omega_s/2\epsilon_0}$ is the normalised, slowly varying signal field strength and $\Delta k = k_c^{\parallel} + k_p$, where $k_c^{\parallel}$ is the projection of the coupling-field wave vector along the wave vector of the signal field. ρ_{rg} is the single-atom off-diagonal density-matrix element between the states $|r\rangle$ and $|g\rangle$. This quasiparticle is a coherent superposition of an electromagnetic and an atomic component. In the limit of low group velocity $v_{\mathrm{gr}} \ll c$ the mixing angle is $\vartheta \to \pi/2$. This means that the dark-state polariton has an almost purely atomic character.

2.1.2. Storage of Light

So far the control field was assumed to be time-independent. By varying Ω_c in time it is possible to store a signal light pulse in the medium and retrieve it at a later point in time. This can be understood using Eq. (2.9). A reduction in control intensity leads to smaller group velocities. If Ω_c is adiabatically ramped to zero, the signal light pulse can be completely stopped. After a variable dark time τ_d the control laser can be ramped up again and the light pulse resumes propagation finally leaving the medium.

The directed retrieval of the light pulse from the ensemble can also be understood from a different point of view. For simplicity we restrict ourselves to the case where the signal light pulse only contains a single photon and the atomic cloud consists of N atoms. The stored light pulse can then be described by a Dicke state[3] [109, 110]

$$|D_{N-1}^1\rangle = \frac{1}{\sqrt{N}} \sum_{j=1}^{N} e^{i\Delta\boldsymbol{k}\boldsymbol{x}_j} |g_1, ..., r_j, ..., g_N\rangle. \tag{2.12}$$

Here, $\Delta\boldsymbol{k} = \boldsymbol{k}_s + \boldsymbol{k}_c$ is the wave vector of the excitation. Furthermore, the notation $|g_1, ..., r_j, ..., g_N\rangle$ means that the j-th atom is in the Rydberg state (see App. A for details). $\boldsymbol{x}_j$ describes the position of atom j. In this picture, the ramp-up of the control field during retrieval leads to a coherent and collective emission of a photon from the ensemble. The light emitted from all the different atoms interferes destructively except in the direction of the input light pulse. For this to work, the atomic ensemble must be much larger than one wavelength of the signal light. This concept can easily be extended to higher photon numbers.

We will now discuss the question of whether varying Ω_c in time leads to additional absorption. In the dark-state polariton picture the deceleration of a light pulse corresponds to an increase in the mixing angle ϑ. As long as the change in Ω_c is sufficiently slow, the state vector of the system adiabatically follows the dark state (2.10) and no additional absorption occurs. Specifically, the change in Ω_c has to occur on a time scale τ_a given by [110]

$$\tau_a \gg \frac{v_{\mathrm{gr}}^0}{c} \frac{\Gamma_e}{c\sigma_{\mathrm{cyc}}\varrho\Gamma_{eg}}, \tag{2.13}$$

[3] As explained in Chap. 2.2.6, the first Dicke state (2.12) can also be created by utilising Rydberg blockade [71].

where v_{gr}^0 is the group velocity before storage. The second factor on the right side of this equation is less than 1 ps for typical experimental parameters. Since this deceleration process is coherent, it can be reversed. It should be noted that in most practical situations $v_{\mathrm{gr}} \ll c$ and therefore a diabatic switch-off only results in loss of the very small electric component of the polariton [51].

An important quantity in storage experiments is the storage and retrieval efficiency $\eta_{sr} = E_{\mathrm{out}}/E_{\mathrm{in}}$. This is the energy of the light pulse after storage and retrieval E_{out}, relative to the energy of the input light pulse E_{in}. For efficient storage two requirements have to be met. First, the light pulse has to be sufficiently long to fulfil the condition $\Delta\omega_s \ll \Delta\omega_{\mathrm{trans}}$ for high EIT transmission. Second, the duration of the light pulse must be small enough such that it can be fully compressed into the medium, i.e. $v_{\mathrm{gr}}/L < 1/\Delta\tau_s$. Eq. (2.6) yields $v_{\mathrm{gr}}/L < \Delta\omega_s$. Experimentally, high storage efficiency requires high optical depth [111, 112] and an appropriate choice of $|\Omega_c|$.

Efficient retrieval relies on the spatial coherence of the stopped polariton. Various decoherence mechanisms can lead to a decay in the retrieval efficiency over time. One example is a finite spatial coherence length of the gas. During storage, a signal and a control photon are absorbed, leading to a momentum transfer to the atoms in $|r\rangle$ of $\hbar\Delta\boldsymbol{k} = \hbar\boldsymbol{k}_p + \hbar\boldsymbol{k}_c$. Hence they start moving with recoil velocity $\boldsymbol{v}_{\mathrm{rec}} = \hbar\Delta\boldsymbol{k}/m$ relative to the atoms in $|g\rangle$. After moving a distance greater than a coherence length, the retrieval efficiency is significantly reduced. In a thermal gas with temperature T the motion of the atoms yields a spatial coherence length that approximately equals the thermal de-Broglie wavelength $\lambda_{dB} = \hbar\sqrt{2\pi/mk_BT}$, with atom mass m and Boltzmann constant k_B [113]. A more detailed analysis which can be found in App. A shows that η_{sr} decays as a function of the dark time like a Gaussian with $1/e$-time

$$\tau = \frac{\lambda_{dB}}{|\boldsymbol{v}_{\mathrm{rec}}|\sqrt{2\pi}}. \tag{2.14}$$

It should be noted that the dephasing that is responsible for the decay of η_{sr} is not necessarily identical with the dephasing described by γ_{rg} in Eq. (2.4). η_{sr} can, for example, decay like a Gaussian due to the thermal motion of the atoms, whereas dephasing described by γ_{rg} always leads to an exponential decay of coherence.

This also becomes clear by considering finite laser linewidths. As the lasers are switched off during the dark time, the laser linewidths do not affect the decay time in storage and retrieval experiments. However, the laser linewidths do affect the maximal EIT transmission.

Additional potential reasons for the decay of the retrieval efficiency are, for example, spatially inhomogeneous electric or magnetic fields. If $|r\rangle$ is a Rydberg state then collisions with ground state atoms can also cause dephasing. This is discussed in Chap. 4.4.

2.2. Rydberg Atoms

Rydberg atoms are highly excited atoms. They have been extensively studied in the past and many of their properties are well known. This is particularly true for the alkali atom rubidium. The properties relevant for this thesis are summarised in Chap. 2.2.1. A more thorough introduction can be found in Refs. [69, 114]. For a quantitative understanding of Rydberg atoms, detailed knowledge of their valence electron's wavefunction is required. How it can be calculated numerically is shown in Chap. 2.2.2. Rydberg atoms are very sensitive to external electric fields. More details on this can be found in Chap. 2.2.3. The single photon switch and transistor discussed in this thesis is based on the dipole-dipole interaction between Rydberg atoms. Therefore this topic is covered by Chap. 2.2.4. Interestingly, the dipole-dipole interaction can be enhanced by the use of a Förster resonance, as explained in Chap. 2.2.5. Finally, Chap. 2.2.6 introduces the concept of Rydberg blockade and how it can be exploited in EIT with Rydberg states.

2.2.1. Basic Properties

Rubidium atoms are similar to hydrogen, because they have one valence electron, also referred to as the Rydberg electron, orbiting around a positively charged core. In Rydberg atoms the valence electron mostly resides near its classical outer turning point (s. Fig. 2.2(b)) and thus far away from the core. There, it is only sensitive to the net charge of the core which gives a $-1/r$ Coulomb potential. Hence many properties of Rydberg atoms are very similar to those of hydrogen. An important difference between the two of them, however, is that the $^{87}Rb^{+}$ core contains 36 electrons in the inner shells which have finite size. The charge distribution of the $^{87}Rb^{+}$ core plays a role when the electron comes near the core. In this situation, two effects become relevant. First, the screening of the nucleus' charge by the core electrons is reduced and second the electron can polarise the core. As a result of these two effects, the eigenstates of rubidium are more tightly bound than their counterparts in hydrogen. This is particularly relevant for states with low angular momentum quantum numbers l which have a large spatial overlap with the core. The difference in binding energies of Rydberg electrons compared with those of hydrogen can be parameterised by the empirical quantum defects δ_{nlj}. The binding energy is then given by [69]

$$E_{n,l,j} = \frac{-hcR_y}{(n-\delta_{nlj})^2}, \tag{2.15}$$

where for alkali atoms the constant R_y is related to the Rydberg constant $R_\infty = 109737.316\,\mathrm{cm}^{-1}$ via $R_y = R_\infty M/(M+m_e)$. Here M is the mass of the atom's core and m_e the mass of the electron. The quantum defects strongly depend on l. The much weaker dependence on the quantum number of the total angular momentum of the valence electron j is due to the fine structure splitting. By

considering small n-dependent corrections, improved agreement between W and experimental data can be achieved. The quantum defects are obtained by fitting the empirical expression [115]

$$\delta_{nlj} = \delta_0 + \frac{\delta_2}{(n-\delta_0)^2} \tag{2.16}$$

to spectroscopic data. For the s, p, and d states of ^{85}Rb these can be found in Ref. [116] and for the f states of ^{85}Rb in Ref. [117]. δ_0 is approximately 3.13 and 2.65 for the s and p states of rubidium respectively. ^{87}Rb and ^{85}Rb have essentially identical quantum defects. For $l > 3$ the quantum defects are less than $4{\cdot}10^{-3}$ for $n \geq 30$ [117,118]. These states have practically the same energies like their equivalents in hydrogen and are therefore called the hydrogenic states.

The properties of highly excited Rydberg states are mostly governed by their binding energy, which is determined by the effective principal quantum number $n^* = n - \delta_{nlj}$. Hence their scaling behaviour with n^* is similar to hydrogen [119]. Important properties are summarised in Tab. 2.1 and values are given for the $100S_{1/2}$ state of ^{87}Rb. The orbital radius[4] of the Rydberg electron's wavefunction is very large compared to that of the ground state. As a result of the small spatial overlap with the ground state wavefunction, Rydberg states have a fairly long spontaneous lifetime which scales like $(n^*)^3$ and is 1.3 ms for the $100S_{1/2}$ state [120]. The large orbital radius is also associated with large radial matrix elements between neighbouring states. This makes them very sensitive to electric fields and blackbody radiation. The blackbody radiation induces transitions to neighbouring states thus reducing the lifetime of Rydberg states. For the $100S_{1/2}$ state, the lifetime in the presence of spontaneous emission and blackbody radiation at a temperature of $T = 300\,\mathrm{K}$ is $336\,\mu$s [120]. The sensitivity to electric fields results in a very strong van der Waals interaction between Rydberg atoms. This is crucially important to this thesis and is the subject of Chap. 2.2.4. Finally, as the Rydberg electron's wavefunction has little overlap with the atomic nucleus, the hyperfine coupling is small compared to all other relevant energy scales and can usually be neglected.

2.2.2. Radial Wavefunction

To calculate radial matrix elements it is necessary to solve Schrödinger's equation for the valence electron. Using atomic units[5] (a.u.) and the infinite-nuclear-mass approximation, the equation can be written as

$$\left(-\frac{1}{2}\nabla^2 + V(r)\right)\psi(r,\theta,\phi) = E_{n,l,j}\psi(r,\theta,\phi). \tag{2.17}$$

[4] Orbital radius is defined as $\int_0^\infty r R_{n,l}(r) r^2 dr$ with radial wavefunction $R_{n,l}(r)$ as in Chap. 2.2.2.

[5] Atomic units are used throughout Chaps. 2.2.2 to 2.2.5.

Quantitiy	Scaling	^{87}Rb $100S_{1/2}$	Ref.	Chap.
Binding energy E	$(n^*)^{-2}$	$h \cdot 351\,\mathrm{GHz}$	[116]	
Energy difference $E_n - E_{n-1}$	$(n^*)^{-3}$	$h \cdot 7.35\,\mathrm{GHz}$	[116]	
Orbital radius	$(n^*)^2$	$0.74\,\mu\mathrm{m}$	[69]	
$nS_{1/2}$ hyperfine-struct. interval	$(n^*)^{-3}$	$h \cdot 36\,\mathrm{kHz}$	[116]	
Radiative lifetime ($T = 300\,\mathrm{K}$)		$336\,\mu\mathrm{s}$	[120]	
Static electric polarisability α_0		$h \cdot 6.2\,\mathrm{GHz\,V^{-2}cm^2}$	[121]	2.2.3
Van der Waals coefficient C_6	$(n^*)^{11}$	$h \cdot 56\,\mathrm{THz}\,\mu\mathrm{m}^6$	[122]	2.2.4

Table 2.1.: Properties of Rydberg atoms. Their dependence on the effective principal quantum number n^* is analogous to hydrogen and can be expressed by power laws. For high n many properties are strongly altered compared to ground state atoms.

Here r is the distance between the valence electron and the nucleus, and $V(r)$ is the core potential which is spherically symmetric. Consequently the wavefunction $\psi(r, \theta, \phi) = R_{n,l}(r) Y^l_{m_l}(\theta, \phi)$ is separable into a radial part $R_{n,l}(r)$ and an angular part which is given by the spherical harmonics $Y^l_{m_l}(\theta, \phi)$. Inserting this into Eq. (2.17) yields a differential equation for the radial wavefunction of the electron

$$\left[-\frac{1}{2}\left(\frac{\partial^2}{\partial r^2} + \frac{2}{r}\frac{\partial}{\partial r}\right) + \frac{l(l+1)}{2r^2} + V(r)\right] R_{n,l}(r) = E_{n,l,j} R_{n,l}(r). \tag{2.18}$$

$R_{n,l}(r)$ has to fulfil the normalisation condition

$$\int_0^\infty |R_{n,l}(r)|^2 r^2 dr = 1. \tag{2.19}$$

To account for deviations of $V(r)$ from the Coulomb potential of hydrogen, an l-dependent model potential [123]

$$V_l(r) = -\frac{Z_l(r)}{r} - \frac{\alpha_c}{2r^4}\left(1 - e^{(r/r_c)^6}\right) \tag{2.20}$$

can be used, where α_c is the static electric dipole polarisability of the ionic core. The first summand in Eq. (2.20) describes the screened Coulomb potential of the core with radial charge

$$Z_l(r) = 1 + (Z-1)e^{-a_1 r} - r(a_3 + a_4 r)e^{-a_2 r}, \tag{2.21}$$

where Z is the charge number of the nucleus. The second summand in Eq. (2.20) reflects the core polarisability. r_c, a_1, a_2 and a_3 are coefficients that are obtained from fits to experimental data with $\alpha_c = 9.0760\,\mathrm{a.u.}$ kept fixed [123]. To calculate quantities that are only sensitive to the radial wavefunction at large distances from the core, like radial matrix elements for high-n states, the potential can be approximated by

$$V(r) \approx -\frac{1}{r} - \frac{\alpha_c}{2r^4}. \tag{2.22}$$

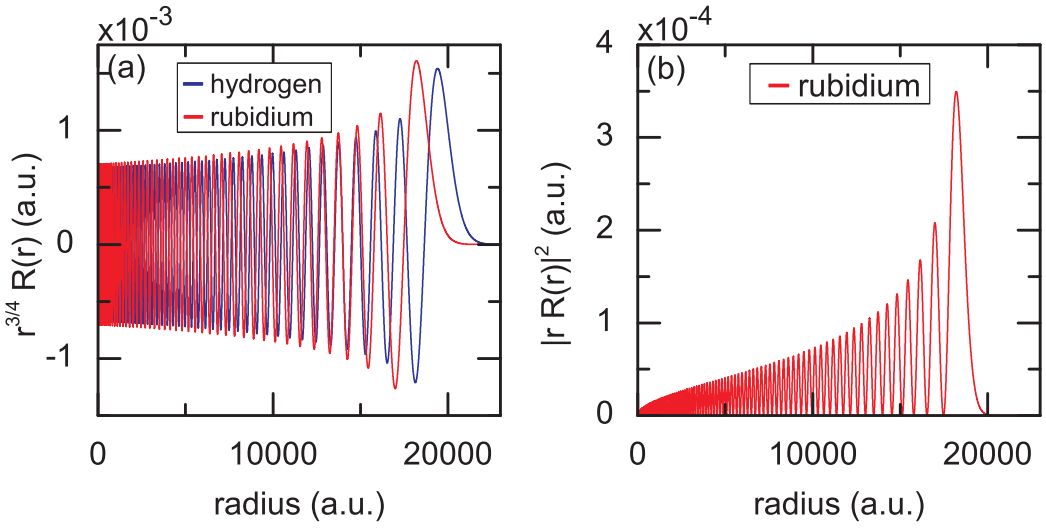

Figure 2.2.: Radial wavefunction of the $100S_{1/2}$ state calculated with Numerov's algorithm. (a) Comparison of the radial wavefunctions[a] of rubidium and hydrogen. The wavefunction for rubidium is shifted towards the core. (b) Corresponding radial probability density for rubidium. The valence electron spends most of the time far away from the core.

[a]The scaling is motivated by the fact that for $(2l+1)^2 < r < (n^*)^2$ the amplitude of $\tilde{R}$ is approximately constant [124].

$R_{n,l}(r)$ can be calculated by numerical integration of Eq. (2.18). To obtain an approximately constant number of grid points per oscillation period of $R_{n,l}(r)$, a square root scaling of r is used. Substituting

$$\tilde{r} = \sqrt{r}, \qquad \tilde{R} = r^{3/4} R_{n,l}(r) \tag{2.23}$$

into Eq. (2.18) we obtain[6] [124]

$$\left(-\frac{\partial^2}{\partial \tilde{r}^2} - 8E_{n,l,j}\tilde{r}^2 + \frac{\left(2l+\frac{1}{2}\right)\left(2l+\frac{3}{2}\right)}{\tilde{r}^2} - 8 - \frac{4\alpha_c}{\tilde{r}^6} \right) \tilde{R} = 0. \tag{2.24}$$

This differential equation can be solved using the Numerov algorithm [125] and binding energies E from Eq. (2.15). Following [126] we perform the integration inwardly with a step size of 0.01, starting at an outer radius $r_o = 2n(n+15)$ which is much larger than the classical turning point of the wavefunction. The boundary conditions we use are $\tilde{R}|_{r_o} = 0$ and $\partial\tilde{R}/\partial\tilde{r}|_{r_o} \lesssim 0$. At small radii the model (2.20) becomes unphysical. For low l we hence stop integration at an inner radius of $r_i = \sqrt[3]{\alpha_c}$ which only causes a small error in calculated matrix elements. For high l, we truncate the wavefunction at an inner radius where the solution starts diverging [126]. To verify the performance of the numerical integration,

[6]The sign of the third summand in Ref. [124] is probably a misprint.

the result can be compared to the analytical solution of Eq. (2.18) for hydrogen. The scalar product between numerical and analytical result typically deviates from unity by less than $4 \cdot 10^{-4}$ for $n \geq 20$.

Fig. 2.2(a) shows the numerically calculated radial wavefunction for the state $100S_{1/2}$ of rubidium and hydrogen. Because of the increased binding energy of rubidium's valence electron compared to hydrogen, the wavefunction is shifted to smaller radii. Fig. 2.2(b) shows the corresponding radial probability density which has a maximum near the classical outer turning radius. Therefore, the valence electron spends most of the time far away from the core.

The radial matrix elements for transitions from the $5P$ state of ^{87}Rb to the nS and nD Rydberg states can also be calculated numerically and are approximately given by [19]

$$R_{5P}^{nS} = 0.014 \times (50/n)^{3/2} a_0 \quad \text{and} \quad R_{5P}^{nD} = -0.024 \times (50/n)^{3/2} a_0, \tag{2.25}$$

where a_0 is the Bohr radius.

2.2.3. Electric Fields

Compared to ground state atoms, Rydberg atoms are very sensitive to electric fields. A static electric field $\boldsymbol{E}$ causes a mixing of the energy eigenstates of the bare atom resulting in an energy level shift, known as the Stark shift. Using the electric-dipole approximation, an atom exposed to a static electric field is described by the Hamiltonian [126]

$$H = H_{\text{atom}} - \boldsymbol{d} \cdot \boldsymbol{E} \tag{2.26}$$

with the electric dipole moment of the atom given by $\boldsymbol{d}$. Choosing the z direction along the orientation of the electric field, $\boldsymbol{E} = E_z \hat{z}$, we can write the coupling term as $-d_z E_z$. In the fine-structure basis $\{|n, l, j, m_j\rangle\}$, the electric field therefore couples bare states with selection rules $|\Delta l| = 1$ and $\Delta m_j = 0$. The latter reflects the fact that the Stark Hamiltonian (2.26) commutes with the z component of the the total angular momentum operator J_z. The off-diagonal matrix elements $-E_z \langle n', l', j', m_j | d_z | n, l, j, m_j \rangle$ can be evaluated using standard angular momentum algebra [127] and numerically calculated radial matrix elements (cf. Chap. 2.2.2). The diagonal matrix elements are given by the binding energies $E_{n,l,j}$ according to Eq. (2.15). Because of the Δm selection rule, the eigenenergies can be calculated for each m_j separately by numerical diagonalisation.

Fig. 2.3 shows the obtained energy levels as a function of electric field strength E around $n = 97$ for the $m_j = 1/2$ and $m_j = 3/2$ manifolds. Such a graph is usually called a Stark map. It is clearly visible that the quantum defects and the spin-orbit coupling lift the degeneracy of the energy levels with $l \leq 3$. For $l > 3$, however, these effects are neglected and hence these states show a linear

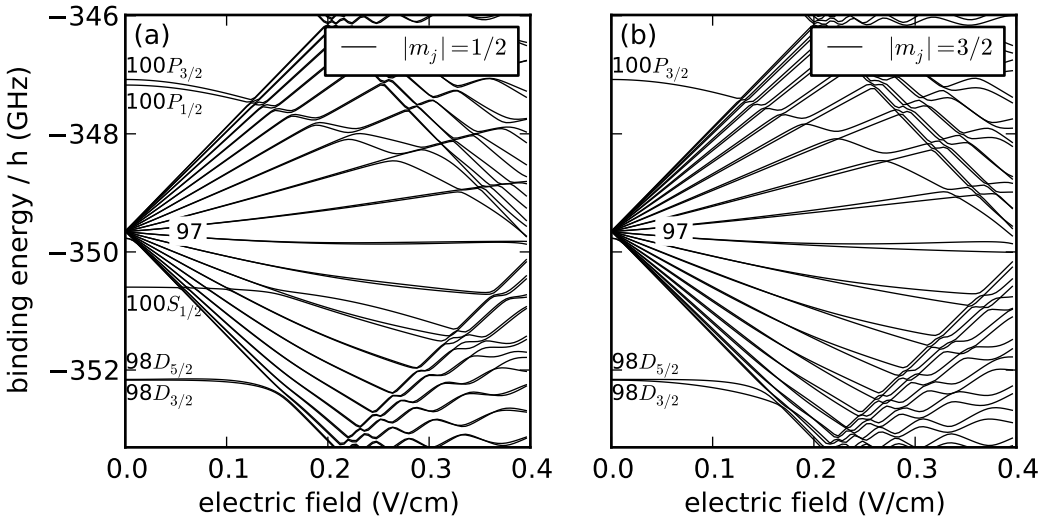

Figure 2.3.: Stark maps near $100S_{1/2}$ in Rb for $|m_j| = 1/2$ (a) and $|m_j| = 3/2$ (b). At fairly low electric fields, on the order of 0.1 V/cm, mixing with adjacent l states becomes relevant. In the calculation, states with $92 \leq n \leq 102$ and $l \leq 20$ were included, which gives sufficiently good convergence for the low-l states.

Stark shift for small energies. The separation of the two extreme states of the $l > 3$ manifold is approximately given by [114]

$$\Delta E_{\text{hyd}} \approx 3n(n-1)E_z. \tag{2.27}$$

The stark maps for $\pm m_j$ are identical as follows from the symmetry properties[7] of the Hamiltonian (2.26) [127]. At low fields, where the interaction energy $-\boldsymbol{d} \cdot \boldsymbol{E}$ is small compared to the detuning of neighbouring energy eigenstates, the Stark Hamiltonian (2.26) can be treated with perturbation theory. For the energetically non-degenerate states in our calculation, this gives, in leading order, a shift that depends quadratically on the electric field

$$\Delta E_{\text{Stark}} = -\frac{1}{2}\alpha_0 \boldsymbol{E}^2, \tag{2.28}$$

where α_0 is the static electric polarisability of the Rydberg atom. For a state $|n, l, j, m_j\rangle$ the polarisability α_0 is given by

$$\alpha_0 = -2 \sum_{(n',l',j') \neq (n,l,j)} \frac{|\langle n', l', j', m_j | d_z | n, l, j, m_j \rangle|^2}{E_{n,l,j} - E_{n',l',j'}} \tag{2.29}$$

[7] This is a consequence of the fact that the electric field does not break the time-reversal symmetry of the Hamiltonian H. If Θ is the antiunitary time-reversal operator [128] which has the properties $\Theta \boldsymbol{x} \Theta^{-1} = \boldsymbol{x}$, $\Theta \boldsymbol{p} \Theta^{-1} = -\boldsymbol{p}$ and $\Theta \boldsymbol{J} \Theta^{-1} = -\boldsymbol{J}$ then the relation $\Theta|\gamma, j, m_j\rangle \propto |\gamma, j, -m_j\rangle$ holds. From $[H, \Theta] = 0$ it follows that the states $|\gamma, j, \pm m_j\rangle$ are degenerate.

with binding energies $E_{n,l,j}$. The sign of α_0 depends on the coupling strength and detuning of the neighbouring states. A numerical calculation of the polarisability for the $100S_{1/2}$ state of rubidium using the same parameters as in Fig. (2.3) yields $\alpha_0 = h \cdot 6.2\,\mathrm{GHz/(V/cm)^2}$ which is in good agreement with experiments [121] where the authors found $\alpha_0 = h \cdot [2.202(28) \cdot 10^{-9}\ (n^*)^6 + 5.53(13) \cdot 10^{-11}\ (n^*)^7]\,\mathrm{MHz/(V/cm)^2}$.

2.2.4. Electric Dipole-Dipole Interaction

As outlined in Chap. 1, the interest in Rydberg atoms stems from the fact that they show long-range dipole-dipole interactions which are large compared to that of ground state atoms. Consider a pair of atoms, A and B, at a distance R which is larger than the extension of the atoms. The z-axis is chosen along the internuclear axis. The leading order of the electrostatic interaction between the atoms is then given by the dipole-dipole interaction[8] [129]

$$V_{dd}(R) = \frac{\boldsymbol{d}_A \boldsymbol{d}_B - 3 d_{A,z} d_{B,z}}{R^3}, \tag{2.30}$$

where $\boldsymbol{d}_{A,B}$ are the electric dipole moments of atoms A and B with respect to their core. The whole system is then described by the Hamiltonian

$$H = H_0 + V_{dd}(R), \tag{2.31}$$

where H_0 is the Hamiltonian in the absence of dipole-dipole interaction.

Introducing the spherical components of a vector $\boldsymbol{V}$ [127]

$$V^{(1)}_{\pm 1} = \frac{1}{\sqrt{2}}(\mp V_x - i V_y), \qquad V^{(1)}_0 = V_z, \tag{2.32}$$

which form a spherical tensor of rank one, Eq. (2.30) can be written as [127]

$$V_{dd}(R) = \frac{d^{(1)}_{A,-1} d^{(1)}_{B,+1} + 2 d^{(1)}_{A,0} d^{(1)}_{B,0} + d^{(1)}_{A,+1} d^{(1)}_{B,-1}}{R^3} = -\sqrt{6}\frac{1}{R^3} T^{(2)}_0. \tag{2.33}$$

In the last expression, the dipole-dipole interaction is expressed by the component $T^{(2)}_0$ of a rank two spherical tensor $T^{(2)}_q$ which is constructed as a tensor product of the spherical tensors $d^{(1)}_{A,q_A}$ and $d^{(1)}_{B,q_B}$ by [127, Eq. (5.1.5)]

$$T^{(2)}_q = \sum_{q_A, q_B} d^{(1)}_{A,q_A} d^{(1)}_{B,q_B} \langle 1, q_A, 1, q_B | 1, 1, 2, q \rangle \tag{2.34}$$

using Clebsch-Gordan coefficients. According to Eq. (2.33), the dipole-dipole interaction couples states such that the individual atoms obey the dipole selection

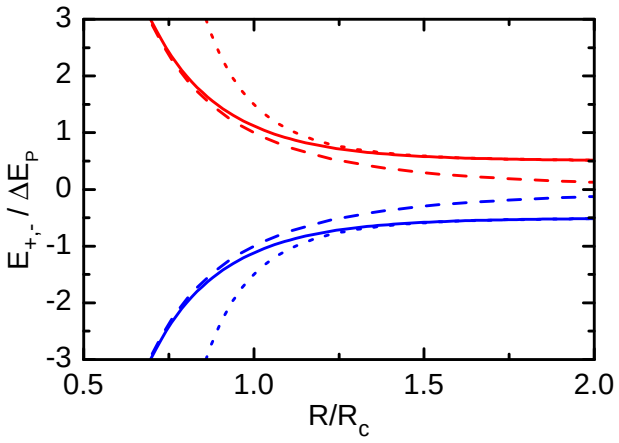

Figure 2.4.: Eigenenergies as a function of atomic separation in the presence of dipole-dipole interaction according to Eq. (2.38). For $R \to \infty$ the eigenenergies are identical to those in the absence of dipole-dipole interaction. At shorter distances the eigenstates repel each other due to the interaction. The asymptotes for $R \to 0$ and $R \to \infty$ are drawn with dashed and dotted lines, respectively.

rules $|\Delta l| = 1$, $\Delta j \in \{0, \pm 1\}$ and $\Delta m_j \in \{0, \pm 1\}$. The sum $M = m_{jA} + m_{jB}$ is a conserved quantity.

Let us now consider the situation where V_{dd} couples two pair states[9] $|\psi_A \psi_B\rangle$ and $|\psi'_A \psi'_B\rangle$. The energy difference between these states in the absence of V_{dd} is given by

$$\Delta E_p = E'_A + E'_B - E_A - E_B. \tag{2.35}$$

Because in Rydberg atoms ΔE_p is determined by the energy defects, it is referred to as the pair state energy defect or Förster energy defect. The Hamiltonian (2.31) can be expressed in the basis $\{|\psi_A \psi_B\rangle, |\psi'_A \psi'_B\rangle\}$ by

$$H = \begin{pmatrix} -\frac{\Delta E_p}{2} & -\frac{C_3}{R^3} \\ -\frac{C_3}{R^3} & \frac{\Delta E_p}{2} \end{pmatrix}. \tag{2.36}$$

Here the real coefficient C_3 is given by $C_3 = \sqrt{6}\langle \psi_A \psi_B | T_0^{(2)} | \psi'_A \psi'_B \rangle$. In the case of product states, C_3 can be written as the product

$$C_3 = D \cdot R^{n'_A l'_A}_{n_A l_A} R^{n'_B l'_B}_{n_B l_B} \tag{2.37}$$

[8] Using the Born-Oppenheimer approximation, the motion of the atoms is neglected. In addition, retardation effects do not play a role as wavelengths corresponding to the transition energies to the neighbouring Rydberg states, which dominate the dipole-dipole interaction, are on the order of centimetres which is small compared to the size of the atom cloud used in this thesis.

[9] This notation is used for pair states that are symmetrised in order to fulfil the commutation relations of bosons. In Chap. 2.2.5 the symmetrisation of specific pair states is demonstrated. Sometimes readability is facilitated by the use of unsymmetrised product states $|\psi_A\rangle_A |\psi_B\rangle_B$. If this is the case, it is explicitly stated.

of an angular part D and a part that only depends on the radial matrix elements $R^{n'_A l'_A}_{n_A l_A}$ and $R^{n'_B l'_B}_{n_B l_B}$ [127]. D can be calculated using angular momentum algebra (cf. App. B, Ref. [129]). The Hamiltonian (2.36) can be easily diagonalised yielding eigenvalues

$$E_\pm(R) = \pm\sqrt{\Delta E_p^2/4 + C_3^2/R^6}. \tag{2.38}$$

The eigenenergies depend on the separation R between the atoms and are depicted in Fig. 2.4(a). The characteristic radius

$$R_c = |C_3/\Delta E_p|^{1/3} \tag{2.39}$$

marks the transition between two regimes.

For $R \gg R_c$, the dipole-dipole interaction $V_{dd}(R)$ only results in a small perturbation to the bare atom states. Therefore, the eigenenergies can be approximated by

$$E_\pm(R) = \pm\frac{1}{2}|\Delta E_p| - \frac{C_{6,\pm}}{R^6} \qquad (R \gg R_c) \tag{2.40}$$

with the van der Waals coefficients $C_{6,\pm} = \mp C_3^2/|\Delta E_p|$. This limit is called the van der Waals regime in which the interaction potential is proportional to $1/R^6$.

For $R \ll R_c$, the interaction dominates the Hamiltonian (2.36) and we obtain for the eigenenergies

$$E_\pm(R) = \pm\frac{C_3}{R^3} \qquad (R \ll R_c). \tag{2.41}$$

This is called resonant dipole-dipole regime. Here, the eigenenergies scale as $1/R^3$, similar to the potential of two static dipoles.

The above treatment, where only two pair states were considered, is a good approximation if all other pair states are far detuned or the coupling to them is small. Often more pair states have to be taken into account and the corresponding Hamiltonian has to be diagonalised numerically. For large R, however, where the dipole-dipole interaction is small compared to the spacing of the energy levels, second order perturbation theory is applicable [129]. The energy shift of a pair state $|\Psi_i\rangle$ is given by $\Delta E_{\mathrm{vdW}} = -C_{6,i}/R^6$, with

$$C_{6,i} = -\sum_{j\neq i} \frac{|\langle\Psi_j|\sqrt{6}T_0^{(2)}|\Psi_i\rangle|^2}{E_{p,i} - E_{p,j}}. \tag{2.42}$$

Here the sum runs over all other pair states $|\Psi_j\rangle$ with pair state energies $E_{p,j}$. As the matrix element in Eq. (2.42) scales as $(n^*)^4$ and the energy between adjacent states as $(n^*)^{-3}$, the C_6 coefficients are proportional to $(n^*)^{11}$. Theoretical predictions for the C_6 coefficients of the pair states $|nl, nl\rangle$ in alkali atoms can

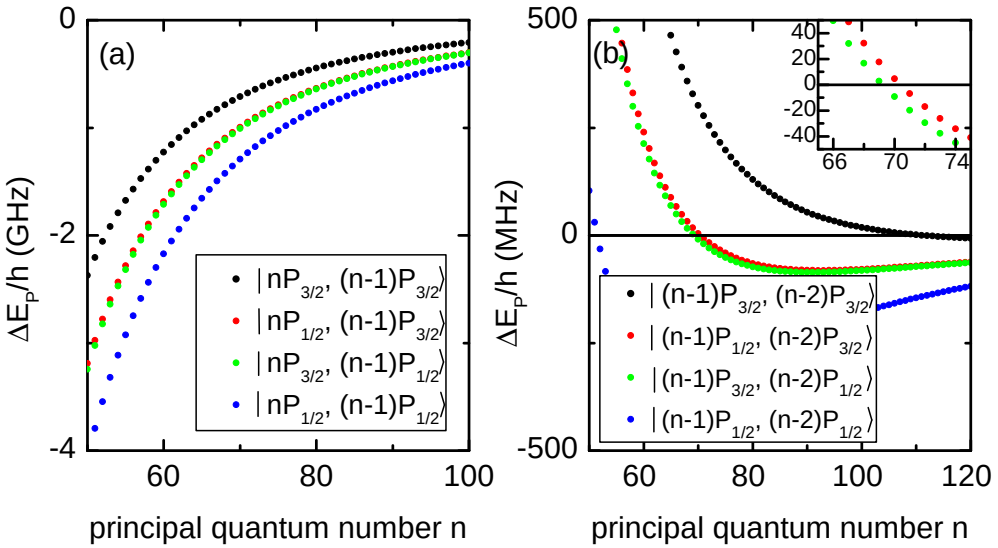

Figure 2.5.: Pair state energy defects in rubidium as a function of principal quantum number. (a) For $|nS_{1/2}, nS_{1/2}\rangle$, four states with the same sign dominantly contribute to the C_6 coefficient resulting in a repulsive van der Waals interaction. (b) For $|nS_{1/2}, (n-2)S_{1/2}\rangle$, the pair state energy defects for two states change their sign near $n = 70$ and nearly vanish (s. inset). Thus, they create a Förster resonance with a large C_6 coefficient.

be found in Refs. [122, 129]. For the $|100S_{1/2}, 100S_{1/2}\rangle$ state, C_6 is quoted in Tab. 2.1.

Strong and long-range dipole-dipole interactions require small pair state defects ΔE_p. Fig. 2.5(a) shows the Förster energy defects of pair states that are relevant for the van der Waals coefficient of the state $|\psi_A\psi_B\rangle = |nS_{1/2}, nS_{1/2}\rangle$ in rubidium. According to the selection rules of the dipole-dipole interaction, this state only couples to neighbouring p-states. The pair states with the smallest detuning are the four states $|nP_{j_1}, (n-1)P_{j_2}\rangle$ with $j_1, j_2 \in \{1/2, 3/2\}$. Note that these pair states show Zeeman degeneracy which has to be considered when calculating the energy eigenvalues of the system [129]. The combination of these states results in a repulsive van der Waals interaction.

The Förster energy defects for the state $|nS_{1/2}, (n-2)S_{1/2}\rangle$, which are shown in Fig. 2.5(b), exhibit a more interesting behaviour. Near $n = 70$ the energy defects of $|(n-1)P_{1/2}, (n-2)P_{3/2}\rangle$ and $|(n-1)P_{3/2}, (n-2)P_{1/2}\rangle$ are close to zero and the dipole-dipole interaction is resonantly enhanced. This is called a Förster resonance and will be discussed in detail in Chap. 2.2.5.

2.2.5. Förster Resonances in Rubidium

In many experiments it is desirable to attain the strongest possible interaction between Rydberg atoms. Strong interaction can be achieved if it is resonantly

enhanced by a Förster resonance [130, 131], which occurs when two pair states become degenerate. Close to resonance, the C_6 coefficient of the van der Waals interaction and the characteristic radius R_c of Eq. (2.39) are drastically enhanced. Right at resonance R_c diverges leading to a long-range $1/R^3$ interaction potential for all R.

In rubidium the pair state $|X\rangle = |nS_{1/2}, (n-2)S_{1/2}\rangle$ is almost degenerate with $|Y_1\rangle = |(n-1)P_{1/2}, (n-2)P_{3/2}\rangle$ and $|Y_2\rangle = |(n-1)P_{3/2}, (n-2)P_{1/2}\rangle$ near $n = 70$, as shown in Fig. 2.5(b). In this chapter the dipole-dipole interaction for these states will be discussed in more detail.

First we consider only two pair states $|X\rangle$ and $|Y_1\rangle$. Abbreviating $|a\rangle = |nS_{1/2}\rangle$, $|b\rangle = |(n-2)S_{1/2}\rangle$, $|c\rangle = |(n-1)P_{1/2}\rangle$ and $|d\rangle = |(n-2)P_{3/2}\rangle$, these pair states can be written as the sum of product states $|X\rangle = \frac{1}{\sqrt{2}}(|a\rangle_A|b\rangle_B + |b\rangle_A|a\rangle_B)$ and $|Y_1\rangle = \frac{1}{\sqrt{2}}(|c\rangle_A|d\rangle_B + |d\rangle_A|c\rangle_B)$. Using that the Hamiltonian (2.31) is symmetric under particle exchange, its matrix elements can be written as

$$\langle X|H|Y_1\rangle = \langle a|_A\langle b|_B\, H\, |c\rangle_A|d\rangle_B + \langle b|_A\langle a|_B\, H\, |c\rangle_A|d\rangle_B. \tag{2.43}$$

For the states considered here, the first and second terms on the right side of Eq. (2.43) are proportional to $R_{nS}^{(n-1)P}R_{(n-2)S}^{(n-2)P}$ and $R_{nS}^{(n-2)P}R_{(n-2)S}^{(n-1)P}$, respectively. As the radial matrix elements are dominantly determined by the valence electron's wavefunction at large r, they mostly depend on the difference between the effective principal quantum numbers Δn^*. The radial matrix elements in the first term of Eq. (2.43) have $\Delta n^* \approx \pm 0.5$ compared to $\Delta n^* \approx \pm 1.5$ in the second term. Hence the first term is much larger than the second. For the states considered here, they differ by a factor of 56. It is therefore justified to approximate the matrix element (2.43) by the expression $\langle X|H|Y_1\rangle \approx \langle a|_A\langle b|_B H|c\rangle_A|d\rangle_B$, which only contains product states. The same argument holds for $\langle X|H|Y_2\rangle$.

So far we have neglected the fact that more quantum numbers are needed to characterise the atom pair. In a coupled basis the quantum numbers of the atom pair's total angular momentum J and $M = m_{jA} + m_{jB}$ can be used for this purpose [129]. The states $|X, J, M\rangle$, $|Y_1, J, M\rangle$ and $|Y_2, J, M\rangle$ then span subspaces U_X, U_{Y_1} and U_{Y_2}, respectively.

We we will now analyse the dipole-dipole interaction in the coupled basis. The off-diagonal matrix elements can be evaluated using Eq. (2.37). Due to the dipole selection rules, V_{dd} does not couple states within the subspaces U_X and $U_{Y_1} \cup U_{Y_2}$. All matrix elements of states belonging to the same pair of subspaces have the same radial matrix elements and can only differ in their angular part D. D only depends on the quantum numbers J and M of the states involved. All non-zero angular matrix elements D for the states $|X, J, M\rangle$ and $|Y_1, J', M'\rangle$ are shown in Fig. 2.6. The dipole-dipole interaction only couples states having the same M. Only the states $|X, 1, \pm 1\rangle$ couple to more than one state, namely the states $|Y_1, 1, \pm 1\rangle$ and $|Y_1, 2, \pm 1\rangle$.

The problem can be further simplified by considering that, in the subspace that is spanned by the states $|Y_1, 1, \pm 1\rangle$ and $|Y_1, 2, \pm 1\rangle$, it is possible to choose

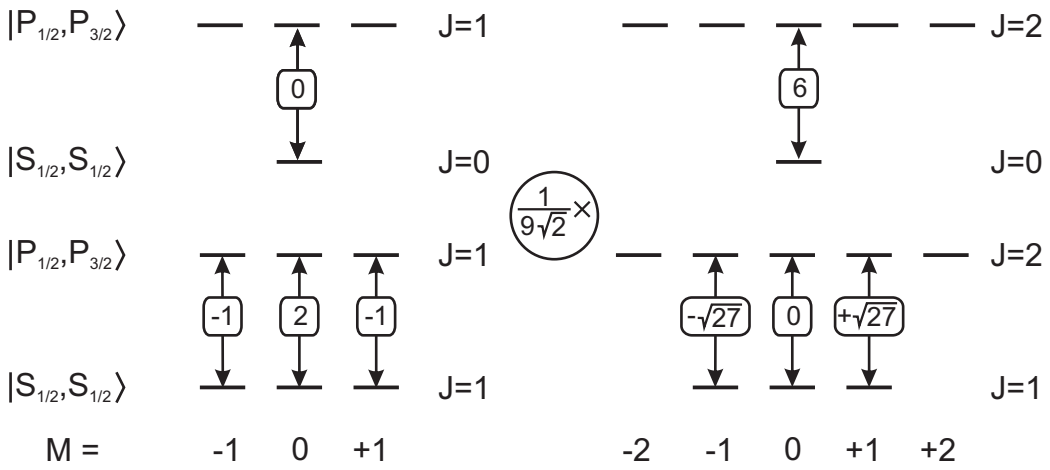

Figure 2.6.: Angular matrix elements $D_{J,M}^{J',M'}$ of the dipole-dipole interaction for the channel $|S_{1/2}, S_{1/2}\rangle \leftrightarrow |P_{1/2}, P_{3/2}\rangle$. The selection rule $\Delta M = 0$ for the dipole-dipole interaction is obvious. The transition $M = 0 \leftrightarrow M = 0$ is only allowed if ΔJ is even. All matrix elements share a common prefactor $1/9\sqrt{2}$.

a basis $\{|Y_1, v_\pm, \pm 1\rangle, |Y_1, w_\pm, \pm 1\rangle\}$ such that only the states $|Y_1, w_\pm, \pm 1\rangle$ couple to $|X, 1, \pm 1\rangle$. The corresponding basis transformation is given by

$$\begin{pmatrix} |Y_1, v_\pm, \pm 1\rangle \\ |Y_1, w_\pm, \pm 1\rangle \end{pmatrix} = \frac{1}{\sqrt{28}} \begin{pmatrix} \mp\sqrt{27} & -1 \\ -1 & \pm\sqrt{27} \end{pmatrix} \begin{pmatrix} |Y_1, 1, \pm 1\rangle \\ |Y_1, 2, \pm 1\rangle \end{pmatrix}. \tag{2.44}$$

In the new basis, the dipole-dipole interaction leads to a pairwise coupling of states. For each decoupled subspace the Hamiltonian can be diagonalise analytically and the eigenvalues are given by Eq. (2.38). For the states considered here, the eigenvalues are shown in Fig. 2.7 (dotted lines). In general the C_3 coefficients can be different in each decoupled subspace and depend on the specific fine structure states involved. Note that some of the eigenenergies belong to eigenspaces with dimension larger than one.

As the states $|Y_2, M, J\rangle$ have only a small detuning from the states $|X, M, J\rangle$, they have to be included in the calculation. It is straightforward to numerically diagonalise the Hamiltonian (2.31) in each decoupled subspace. The numerically obtained eigenvalues are shown in Fig. 2.7 (solid lines). Corrections to the two-level system become relevant at short interatomic distances.

From Fig. 2.7 it also becomes obvious that certain states are not affected by the dipole-dipole interaction at all (blue lines). They are states that do not couple to any other state due to the angular momentum algebra. This phenomenon is called *Förster zero* [129]. In experiments requiring large dipole-dipole interactions, Förster zeros can be a limiting factor. It is advantageous for our experiment that states that are adiabatically connected to the $|S_{1/2}, S_{1/2}\rangle$ threshold do not show any Förster zeros, as can be inferred from Fig. 2.7.

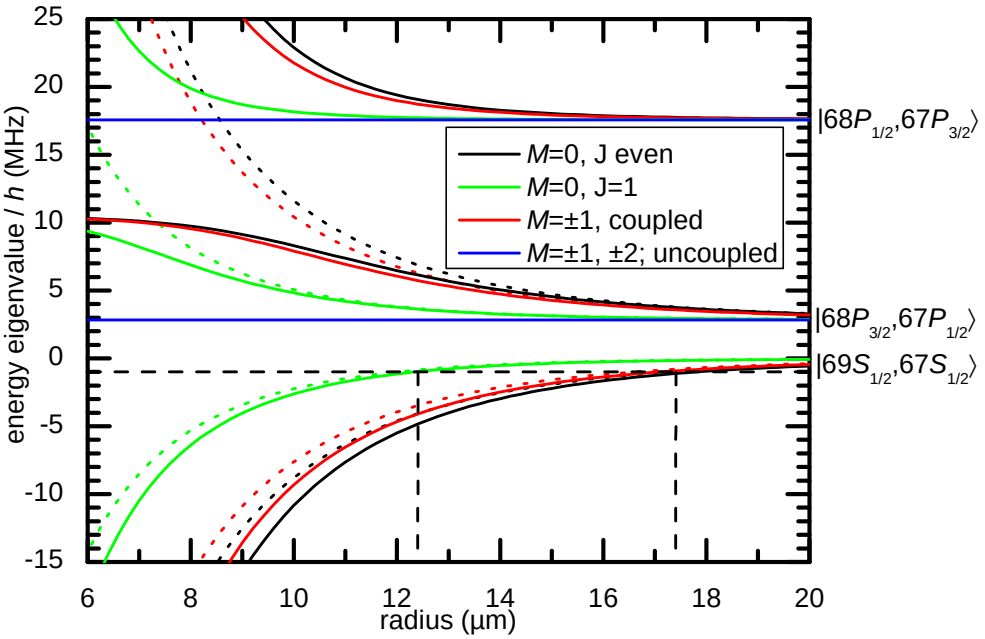

Figure 2.7.: Pair state energies in the vicinity of the state $|69S_{1/2}, 67S_{1/2}\rangle$ in rubidium. Only the states shown here are included in the calculation. If states belong to the same decoupled subspace, then they are drawn in the same colour. The dotted lines show the result when the $|68P_{1/2}, 67P_{3/2}\rangle$ state is also neglected. The dashed lines indicate the radii, where the energies of the states that are adiabatically connected to the $|69S_{1/2}, 67S_{1/2}\rangle$ threshold are shifted by 1 MHz relative the threshold. The relevant radial matrix elements are $R^{68P_{1/2}}_{69S_{1/2}} = 4664\,a_0$ and $R^{67P_{1/2}}_{67S_{1/2}} = 4713\,a_0$. For $R \to \infty$, the state $|68P_{3/2}, 67P_{1/2}\rangle$ is detuned by $\Delta E/h = 2.8\,\mathrm{MHz}$.

It is worth mentioning that often a superposition of pair states is addressed during laser excitation. This is because, typically, the internuclear axis subtends an angle β with the wave vector of the light. The states $|X, J, M\rangle$ with quantisation axis along the internuclear axis are related to the states $|\widetilde{X, J, M}\rangle$ with the quantisation axis along the wave vector by [127]

$$\begin{pmatrix} |X,1,1\rangle \\ |X,1,0\rangle \\ |X,1,-1\rangle \end{pmatrix} = \begin{pmatrix} \cos^2\frac{\beta}{2} & \frac{1}{\sqrt{2}}\sin\beta & \sin^2\frac{\beta}{2} \\ -\frac{1}{\sqrt{2}}\sin\beta & \cos\beta & \frac{1}{\sqrt{2}}\sin\beta \\ \sin^2\frac{\beta}{2} & -\frac{1}{\sqrt{2}}\sin\beta & \cos^2\frac{\beta}{2} \end{pmatrix} \begin{pmatrix} |\widetilde{X,1,1}\rangle \\ |\widetilde{X,1,0}\rangle \\ |\widetilde{X,1,-1}\rangle \end{pmatrix}. \quad (2.45)$$

In many of our experiments, the lasers excite the state

$$|\widetilde{X,1,1}\rangle = \cos^2\frac{\beta}{2}\,|X,1,1\rangle - \frac{1}{\sqrt{2}}\sin\beta\,|X,1,0\rangle + \sin^2\frac{\beta}{2}\,|X,1,-1\rangle. \quad (2.46)$$

The states $|X,1,\pm1\rangle$ have the same C_3 coefficients and therefore the same energies. According to Fig. 2.7, however, the state $|X,1,0\rangle$ has a smaller C_3. This

can be a disadvantage if large C_3 coefficients are desired. The worst case occurs at $\beta = \pi/2$, where the population in $|X, 1, 0\rangle$ is maximal and has a value of $1/2$.

In some experiments, however, we excite the states $|n_1 S_{1/2}, \widetilde{m_j = 1/2}\rangle$ and $|n_2 S_{1/2}, \widetilde{m_j = -1/2}\rangle$ corresponding to $(|X, 0, 0\rangle + |X, 1, 0\rangle)/\sqrt{2}$.

In our experiments, β is typically poorly controlled. If a propagating Rydberg excitation passes a frozen excitation, β typically changes as a function of time. For two copropagating excitations, β is typically time-independent, but has a value that is only well-controlled in the uninteresting case where the temporal distance between the excitations is large.

2.2.6. Rydberg Blockade

The van der Waals interaction between two Rydberg atoms is very large compared to that of two ground state atoms or a ground state and a Rydberg atom. In fact, the van der Waals coefficient of the $|100S_{1/2}, 100S_{1/2}\rangle$ state of rubidium is 20 orders of magnitude larger than that of the $|5S_{1/2}, 5S_{1/2}\rangle$ ground state [122, 132]. This has far-reaching consequences for the laser excitation of an atom pair at a distance of several micrometers, as illustrated in Fig. 2.8(a). A light field that is resonant with the transition from the ground state $|g\rangle$ to a Rydberg state $|r\rangle$ of the atoms, can excite one of the atoms. At large atomic separations, it is also possible to excite both atoms to the pair state $|rr\rangle$. At shorter distances, however, the van der Waals potential causes an energy shift of $|rr\rangle$. Hence the laser field only off-resonantly couples the states $|gr\rangle$ and $|rr\rangle$ and the excitation of both atoms to the state $|rr\rangle$ is suppressed. This is commonly known as *Rydberg blockade* [70, 71]. In this context, the displacement of the Rydberg state $|rr\rangle$ is also referred to as the blockade shift.

The exact size of the blockade shift is not important for observing blockade as long as it is larger than a certain threshold $V_{\text{thr}} > 0$. This threshold might be given by the linewidth of the Rydberg state or the excitation light. Since the lifetime of highly excited Rydberg states is long compared to the typical time scales of many experiments, V_{thr} is usually defined by the properties of excitation light such as power and pulse length. For a given V_{thr} the blockade radius R_b is defined as

$$|V_{dd}(R_b)| = V_{\text{thr}}, \tag{2.47}$$

where V_{dd} is the dipole-dipole interaction potential that is experienced by the state $|rr\rangle$. For the van der Waals interaction, the blockade radius is therefore $R_b = |C_6/V_{\text{thr}}|^{1/6}$. If two atoms are less than R_b apart, then excitation of both atoms is strongly suppressed.

Fig. 2.8(b) shows the numerically calculated blockade radius for $V_{thr}/h = 1\,\text{MHz}$ for the pair states $|nS_{1/2}, nS_{1/2}, M = 1\rangle$ and $|nS_{1/2}, (n-2)S_{1/2}, M = 1\rangle$. The obtained dependence of the blockade radius on the principal quantum number n can be understood by looking at the pair state defects in Fig. 2.5. For the pair states $|nS_{1/2}, nS_{1/2}, M = 1\rangle$, all relevant p-states have negative Förster

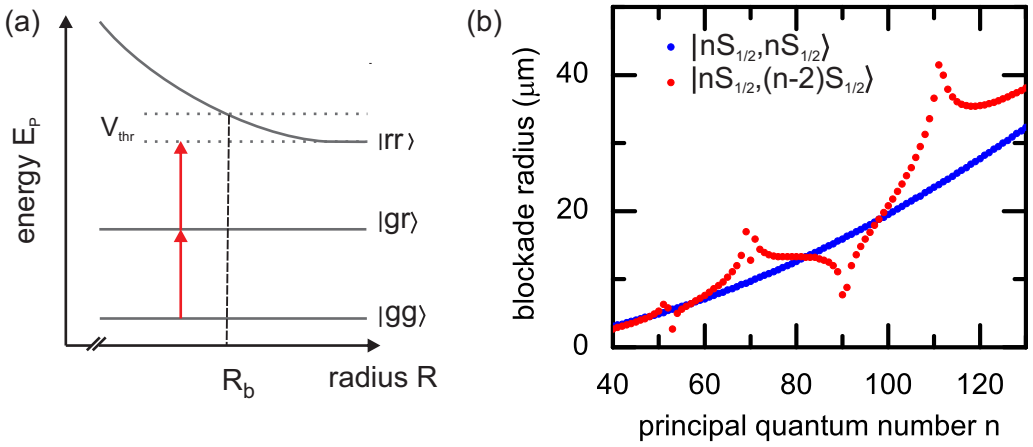

Figure 2.8.: Rydberg blockade during the laser excitation of Rydberg atoms. (a) Schematic energy diagram of atom pair states $|gg\rangle$, $|gr\rangle$ and $|rr\rangle$. The $|rr\rangle$ state is shifted because of the dipole-dipole interaction. For internuclear distances shorter than the blockade radius R_b, the excitation of both atoms to a Rydberg state with resonant light is suppressed. (b) Blockade radius for $V_{\mathrm{thr}}/h = 1\,\mathrm{MHz}$ in rubidium. For the pair state $|nS_{1/2}, nS_{1/2}, M = 1\rangle$, the blockade radius increases proportional to $n^{11/6}$. For the state $|nS_{1/2}, (n-2)S_{1/2}, M = 1\rangle$, the Förster resonances near $n = 51, 70, 111$ lead to local maxima of the blockade radius. Local minima can be attributed to principal quantum numbers where the dipole-dipole couplings to different pair states compensate each other. For the states $|nS_{1/2}, nS_{1/2}\rangle$ and $|nS_{1/2}, (n-2)S_{1/2}\rangle$, the calculation includes four and eight neighbouring pair states, respectively.

defects leading to a blockade radius that approximately increases as n^2. The states $|nS_{1/2}, (n-2)S_{1/2}, M = 1\rangle$ show Förster resonances near $n = 51, 70, 111$. They are responsible for a strongly increased blockade radius compared to that of the states $|nS_{1/2}, nS_{1/2}, M = 1\rangle$. Resonant dipole-dipole interaction also leads to strong mixing of the coupled pair states. This can affect the Rydberg blockade. Local minima, for example near $n = 53, 70, 90$, can occur when channels with positive and negative C_6 coefficients compensate each other.

The Rydberg blockade is not restricted to atom pairs but can also be observed in atomic ensembles. If the spatial extension of the atomic ensemble is much less than the blockade radius, then the situation becomes particularly simple because here only a single atom can be excited to the Rydberg state by resonant laser light. Excitation of more than one atom is suppressed due to the Rydberg blockade. Hence a Fock state with $N = 1$ Rydberg atoms is prepared [71, 72]. This state can be described by the Dicke state of Eq. (2.12). Its properties can be mapped onto a light field, thus yielding a single-photon source [98].

Rydberg blockade in EIT As outlined in Chap. 1, large optical nonlinearities on the few-photon level can be achieved in EIT with Rydberg states. In our

experiments, they are used to create an interaction between single photons, which is the physical mechanism that forms the basis of the single-photon switch. Therefore, this chapter discusses how this interaction arises in Rydberg-EIT.

First, we consider signal light propagating in an atomic ensemble on EIT resonance with $\Delta_s = 0$ and $\Delta_c = 0$, as discussed in Chap. 2.1. An incoming signal photon propagates inside the medium as a dark-state polariton with a large atomic component. If the state $|r\rangle$ in Fig. 2.1(a) is a long lived Rydberg state, then the polariton becomes very sensitive to other Rydberg excitations. In fact, if several Rydberg polaritons propagate inside the medium, then the van der Waals interaction leads to absorption and the transmission of more than one photon at a time is suppressed.

Two Rydberg polaritons propagating at a distance R experience a van der Waals potential $V_{\mathrm{vdW}}(R)$ which leads to an energy shift of the state $|r\rangle$. In the EIT level scheme of Fig. 2.1(a), this corresponds to a non-zero control field detuning $\Delta_c = V_{\mathrm{vdW}}(R)/\hbar$. As can be seen in Fig. 2.1(c), this gives rise to a non-vanishing $\mathrm{Im}(\chi)$ and therefore to absorption. This provides the basis for a possible definition of a blockade radius for Rydberg polaritons. As a threshold, half the single-atom EIT linewidth of Eq. (2.8) can be used, i.e. $V_{\mathrm{thr}} = \gamma_{\mathrm{EIT}}/2$ [99]. For the van der Waals potential this gives the blockade radius

$$R_b = \left| \frac{2C_6\Gamma_e}{\hbar\Omega_c^2} \right|^{1/6}. \tag{2.48}$$

Note, that this definition neglects the effects of dephasing on EIT. Furthermore, it is not the only possible definition and others exist in the literature. An alternative approach, for example, is to use the experimentally obtained FWHM linewidth of the EIT transmission window $\Delta\omega_T$ as V_{thr} [97], which yields a blockade radius

$$R_b = \left| \frac{C_6}{\hbar\Delta\omega_T} \right|^{1/6}. \tag{2.49}$$

In the following we study the absorption that a propagating Rydberg polariton experiences when it encounters a stationary Rydberg excitation. We consider a simple, one-dimensional model which is a good approximation if the blockade radius is large compared to the transverse extend of the polaritons. The extinction ϵ, which is defined as the transmission through the medium in presence of the stationary excitation divided by the transmission in absence of the stationary excitation is then approximately given by

$$\epsilon \approx \exp\left(\frac{2R_b}{l_{a,\mathrm{EIT}}} - \frac{2R_b}{l_a} \right). \tag{2.50}$$

Here l_a is the absorption length for the signal light in absence of the control field. $l_{a,\mathrm{EIT}}$ is the absorption length experienced by the propagating polariton due to imperfect EIT.

3. Experimental Setup

The experiments presented in this thesis were performed using ultracold clouds of ^{87}Rb atoms. The apparatus for the preparation of the atomic clouds was covered extensively by previous dissertations [106,107,133–137]. Chap. 3.1 therefore only gives a rough overview of the experimental procedure and summarises the most important details. The excitation of Rydberg atoms required the implementation and characterisation of a new laser system. This is the subject of Chap. 3.2. Finally, in Chap. 3.3 the optical setup that was used for the realisation of the single-photon switch and transistor is discussed in more detail. This also includes a description of the necessary stray light filtering and the light detection at the single-photon level.

3.1. Preparation of Ultracold Atomic Samples of Rubidum

The experiments presented in this thesis strongly benefit from the properties of an atomic ensemble with densities and temperatures close to the phase transition to a Bose-Einstein condensate (BEC). One reason is that the coherence time in storage and retrieval experiments increases with lower temperature (cf. Eq. (2.14)). This is particularly important if the differential recoil is large. In addition, at lower temperatures the atomic gas can be held in weaker optical dipole traps. This reduces undesired dynamical Stark shifts and photoionisation processes. Many other experiments in the field operate at somewhat higher temperature and turn off all trapping light before exciting Rydberg states.

Preparation of an ultracold ensemble in an optical dipole trap For the preparation of a cloud of ^{87}Rb atoms at densities of $10^{12} - 10^{14}\,\mathrm{cm}^{-3}$ and temperatures of $300 - 400\,\mathrm{nK}$, a cooling scheme comprising several stages is pursued. The first step is to trap and cool ^{87}Rb atoms in a magneto-optical trap (MOT) [138], which is loaded from the background gas of a vapour cell [133]. Subsequently, a short resonant laser pulse transfers the atoms to a second MOT, which is located in a glass cell with lower background pressure ($< 10^{-11}\,\mathrm{mbar}$). These two steps are repeated several times to increase the particle number in the second MOT. After polarisation gradient cooling, the atoms are optically pumped into the hyperfine state $|F, m_F\rangle = |1, -1\rangle$ and stored in a magnetic trap in Ioffe-Prichard configuration [139]. Here the cloud is adiabatically compressed

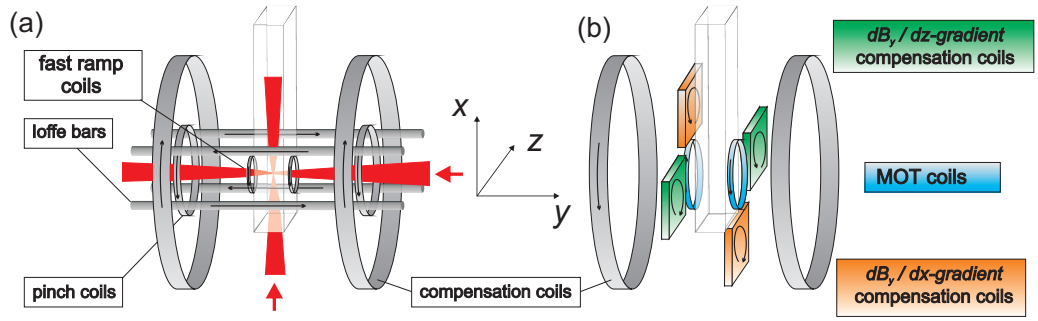

Figure 3.1.: Coil configuration and position of the crossed-beam optical dipole trap. The MOT coils create the magnetic field gradient for the second MOT. The Pinch-coils, Ioffe-bars and compensation coils form the magnetic trap. The fast ramp coils and the gradient compensation coils are used as electrodes in this thesis. The beams of the optical dipole trap are illustrated in red.

and further cooled by radio-frequency induced evaporative cooling [140].

For the final step, the atoms are transferred into a crossed-beam optical dipole trap at a wavelength of 1064 nm (cf. Fig. 3.1(a)) [141]. The vertical beam has a round beam profile with a waist ($1/e^2$ radius of intensity) of 90 μm and a typical power of 0.1 W. The horizontal beam is elliptically shaped with waists $w_x = 60\,\mu$m and $w_z = 1$ mm at a typical power of 4 W. The trapping light is red detuned from all ground state transitions approximately resulting in a harmonic potential with measured trap frequencies $(\omega_x, \omega_y, \omega_z)/2\pi = (136, 37, 37)$ Hz. During the subsequent hold time of 1 s the cloud thermalises and further evaporative cooling takes place. The size of the cloud depends on its temperature, which was different during various experiments performed. Typically, thermal clouds with $N = 1.5 \times 10^5$ atoms at temperatures of $T = 330$ nK were used, corresponding to rms radii of $(\sigma_x, \sigma_y, \sigma_z) = (7, 24, 24)\,\mu$m. The particle number can be controlled by varying the number of loading cycles of the MOT.

The potential created by the dipole trap is attractive for atoms in the ground state, but it is repulsive for atoms in highly excited Rydberg states. As the Rydberg electron is only weakly bound, the potential that is experienced by the atom can be approximated by that of an electron in an oscillating electric field of the form $\boldsymbol{E}(\boldsymbol{x}) = \boldsymbol{E}_0(\boldsymbol{x}) \cos \omega_{\mathrm{dpt}} t$, where $\omega_{\mathrm{dpt}} = 2\pi c/1064\,\mathrm{nm}$ is the angular frequency of the dipole trap light. The resulting time-averaged ponderomotive potential is given by [142]

$$V_p(\boldsymbol{x}) = \frac{e^2 |\boldsymbol{E}_0(\boldsymbol{x})|^2}{4 m_e \omega_{\mathrm{dpt}}^2}. \tag{3.1}$$

The associated polarisabilty has the opposite sign compared to that of the ground state of ^{87}Rb. For the vertical dipole trap beam the maximal ponderomotive potential is ca. $V_p = k_B \times 5\,\mu$K, where k_B is the Boltzmann constant.

The light of the dipole trap can also cause photoionisation of the Rydberg atoms. For given intensities of the dipole trap, a photoionisation rate on the order of 0.8 Hz is expected for the $50S_{1/2}$ state of rubidium [143]. The photoionisation cross section decreases for higher principal quantum numbers.

Magnetic field alignment After the transfer of atoms into the dipole trap the atoms are in the hyperfine state $|F, m_F\rangle = |1, -1\rangle$, with the quantisation axis chosen along the y-axis. A magnetic field of $|\boldsymbol{B}| = 1.5\,\mathrm{G}$ along the same axis preserves the spin polarisation of the atoms during and after the switch-off of the magnetic trap.

For the implementation of the single-photon switch, however, the magnetic field must be aligned parallel to the z-axis and the atoms must be prepared in the state $|F, m_F\rangle = |1, -1\rangle$, with the quantisation axis chosen as the same axis. This can be achieved by adiabatically rotating the magnetic field using three coils that are usually used for the compensation of the earth's magnetic field (not shown in Fig. 3.1). The rotation of the magnetic field is performed during the hold time in the dipole trap mentioned above, following the procedure described in Ref. [107]. After the rotation, a magnetic field $B_z > 0.2\,\mathrm{G}$ is applied to preserve the spin state of the atoms.

Absorption imaging The properties of the atomic sample, such as the particle number and the temperature, can be measured using absorption imaging. To this end, the dipole trap is switched off abruptly and the atom cloud starts expanding in free fall. The cloud is illuminated by a beam that is near-resonant with the cycling transition of ^{87}Rb on the D_2 line. The shadow cast by the atoms is detected by a CCD camera. For the detection of atoms in the $5S_{1/2}$ $F = 1$ ground state of ^{87}Rb, an additional repump laser on the transition $F = 1 \leftrightarrow F' = 2$ of the D_2 line is necessary. Details can be found in Ref. [134].

Coarse timing After preparing the atoms in the optical dipole trap, experiments are typically performed for 1 s. The particle number in the trap decays exponentially with a $1/e$ time of approximately 1.7 s, leading to a considerable change in particle density within the 1 s measurement interval. During the subsequent 200 ms the signal laser is swept across the EIT resonance in order to obtain an EIT spectrum for every prepared sample. Afterwards the dipole trap is switched off and an absorption image is taken. Hereafter a new atomic cloud has to be prepared. A new atomic sample is loaded every 15 s.

Optical dipole potential created by the control field In EIT with the Rydberg states of ^{87}Rb, a strong control light field at a wavelength of $\lambda = 475\,\mathrm{nm}$ is used which creates an optical dipole potential for the ground state atoms in the ensemble. The $5S_{1/2}$ ground state of rubidium has a dynamical polarisability

of $\alpha_{5s} = -163\,\text{a.u.}$ [19] at the control wavelength. The resulting potential is repulsive so that it pushes the atoms away. After time averaging over one optical period, the potential is estimated to be $V_c = -\alpha_{5s} E_c^2(\boldsymbol{r})/4$, where $E_c(\boldsymbol{r})$ is the electric field amplitude of the control beam at position $\boldsymbol{r}$. At a typical control power of $P_c = 32\,\text{mW}$ and a beam waist of $12\,\mu\text{m}$ (cf. Chap. 3.3) this yields a maximal potential height of $V_{c,0} = k_B \times 5.1\,\mu\text{K}$, which is large compared to the temperature of the cloud.

To mitigate the effects of the repulsive potential, all experiments are operated in a pulsed mode with a cycle repetition time t_{cyc}. The control laser is only switched on for a short time $t_{c,on} \ll t_{\text{cyc}}$, typically on the order of a few microseconds. As the distance travelled by the atoms in such a short time is small and as t_{cyc} is much shorter than all trap oscillation periods, it is justified to consider the the potential after a time averaging over one cycle. In a typical experiment, $t_{c,on}$ is shorter than t_{cyc} by a factor of 50, yielding $\langle V_{c,0} \rangle = V_{c,0}/50 = k_B \times 0.1\,\mu\text{K}$. For a thermal gas, this reduces the density in the centre of the trap by $\sim 10\%$, which can often be neglected.

In some experiments, however, a higher ratio $t_{\text{cyc}}/t_{c,on}$ is used. For these experiments, we model the combined trap potential as

$$V_{\text{trap}} = \frac{m}{2}\left(\omega_x^2 x^2 + \omega_y^2 y^2 + \omega_z^2 z^2\right) + \langle V_{c,0} \rangle \exp\left(-2\frac{x^2+y^2}{w_c^2}\right). \tag{3.2}$$

Here, m is the rest mass of ^{87}Rb and w_c the waist of the beam creating the repulsive potential, which propagates along the z direction (cf. Chap. 3.3).

3.2. Laser System for Two-Photon Rydberg Excitation

For the EIT experiments with Rydberg states, presented in this theses, light sources at the wavelength of the signal and the control transitions are required. In the experiments, the signal field drives transitions of the D_1 line of ^{87}Rb at a wavelength of $\lambda = 795.0\,\text{nm}$. The control field couples the $5P_{1/2}$ state to Rydberg states with $n \geq 30$. For these transitions, light at wavelengths ranging from 477.1 to 473.7 nm is necessary.[1]

For the realisation of a single-photon switch based on Rydberg blockade in EIT, it is desirable to achieve small EIT linewidths $\Delta\omega_{\text{trans}}$ for two reasons. Firstly, the Rydberg blockade radius increases for narrower EIT lines (cf. Chap. 2.2.6) leading to better switching contrast of the single-photon switch. Secondly, narrow EIT lines are associated with low group velocities (cf. Fig. 2.1(b) and Eqs. (2.8), (2.9)), which allow for better signal pulse compression and hence higher storage efficiencies.

[1] Corresponding wavelengths for the two-photon excitation over the D_2 line of ^{87}Rb are 482.6 and 479.1 nm and are also covered by the laser system.

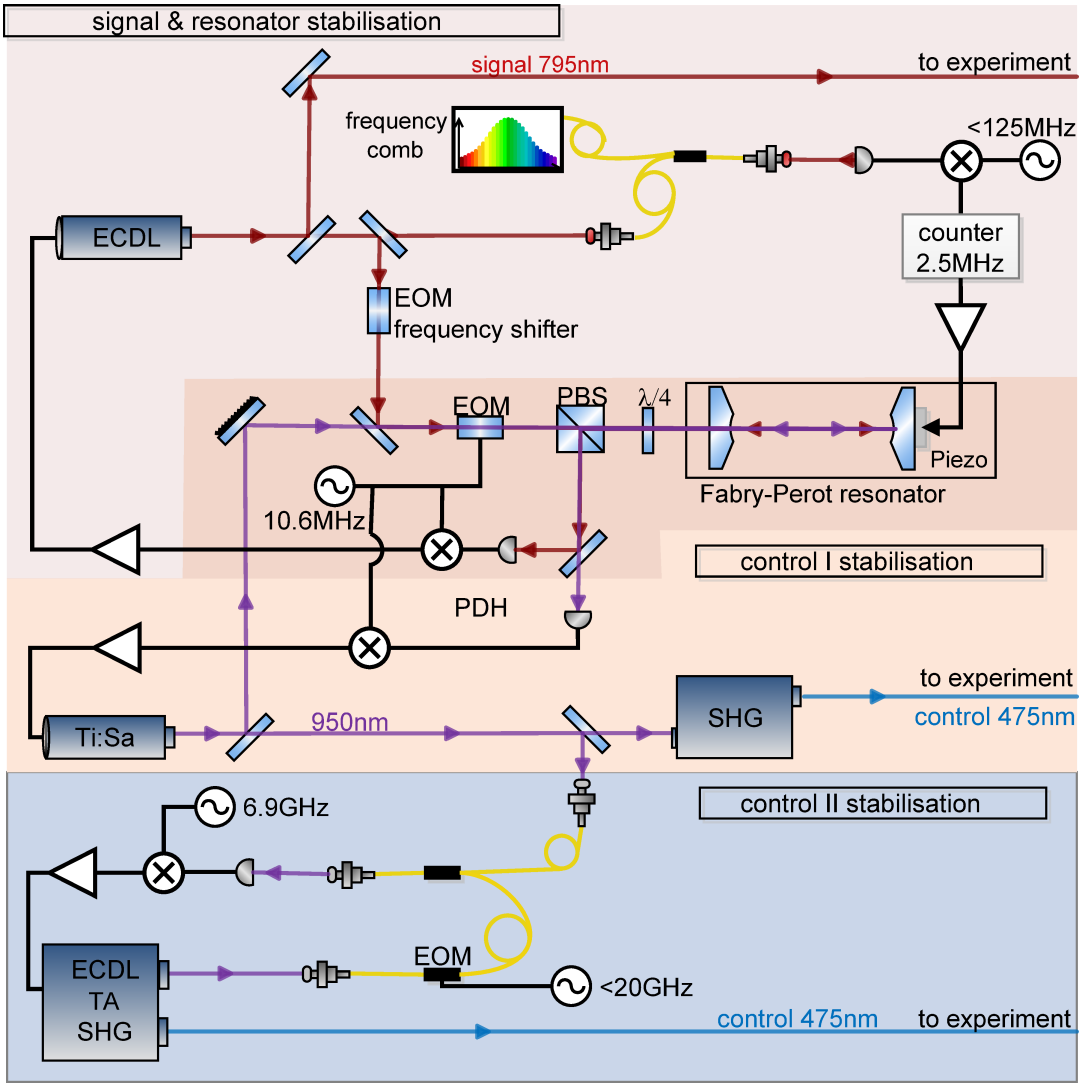

Figure 3.2.: Laser system for the two-photon excitations of Rydberg atoms. A Fabry-Perot resonator serves as a frequency reference. An external cavity diode laser (ECDL) at $\lambda = 795\,\mathrm{nm}$ is stabilised to the resonator. A frequency shifter allows for tuning of the laser frequency relative to the cavity resonance. The resonator is stabilised against long-term drift by comparing the ECDL light with a frequency comb. A Ti:Sa laser, operating at $\lambda = 950\,\mathrm{nm}$, is stabilised to the resonator and provides light at $\lambda = 475\,\mathrm{nm}$ after second harmonic generation (SHG) in a nonlinear crystal. A second laser system, consisting of an ECDL, a tapered amplifier (TA) and an SHG stage, also generates light at $\lambda = 475$ and is stabilised relative to the Ti:Sa laser.

EIT relies on the coherent coupling of the excited state $|e\rangle$ to the Rydberg state $|r\rangle$ by the control field. The finite control laser linewidth leads to a reduction of transparency on EIT resonance and a broadening of the transmission window [108]. Likewise, the linewidth of the signal laser should be much smaller

than the EIT linewidth to minimise undesired absorption. For the reasons mentioned above, a laser stabilisation scheme was implemented which offers a narrow linewidth of both the control and the signal lasers[2] as part of this thesis.

The heart of the laser system is a Fabry-Perot resonator (FPR) which serves as a frequency standard for both the signal and the control laser. The resonator has a length of $L = 100\,\mathrm{mm}$ corresponding to a free spectral range of 1.5 GHz. The spacer is manufactured from Invar, an alloy with a low thermal expansion coefficient. The length of the resonator may be varied by up to 1 μm using a piezo ceramic tube. The spacer, the piezo tube and the mirrors are arranged such that the longitudinal thermal expansion coefficients of all elements approximately cancel each other. Both mirrors have a curvature radius of $R_m = -150\,\mathrm{mm}$, which results in a stable resonator with the degeneracy of the low TEM modes lifted. The resonator has a finesse of $\mathcal{F}_{795nm} \approx 1800$ and $\mathcal{F}_{950nm} \approx 1000$ at 795 nm and 950 nm, respectively. It is mounted to the optical table using a combination of two silicone pads of different elasticity for vibration isolation. A composite housing lined with foam plastic protects the cavity from acoustic disturbances. The length of the cavity drifts around 5 nm per hour under typical lab conditions and 10 mW of light coupled into the cavity.

The signal light is created by an external cavity diode laser (ECDL, *Toptica DL-100*) with 100 mW output power and a free-running linewidth $> 1\,\mathrm{MHz}$.[3] The frequency stabilisation and linewidth reduction scheme is illustrated in Fig. 3.2. The laser frequency is stabilised to a mode of the resonator using the Pound-Drever-Hall (PDH) technique [145, 146]. To this end, some light from the laser is phase-modulated at a frequency of 10.6 MHz and coupled into the resonator. The reflected light is detected with a photodiode and a PDH error signal is created. This is fed into the frequency control unit of the laser (*Toptica FALC 110*) which closes the feedback loop. The loop bandwidth is approximately 600 kHz. The frequency of the laser relative to the resonator resonance can be tuned to arbitrary values by placing an optical frequency shifter in the feedback loop. This is implemented using a fibre-base phase modulator (*Jenoptik, PM785HF*) and only utilising the first sidebands of the modulated light.

The Fabry-Perot resonator is subject to long-term drifts and has to be actively stabilised. An optical frequency comb (*Menlo Systems, FC 1500-250*) is used as a long-term stable frequency reference. Therefore light from the signal laser is superimposed on a photodiode with light from the frequency comb. The resulting beat note signal in the frequency range from 5 to 125 MHz is mixed with a local oscillator of frequency f_{LO}. A frequency to voltage converter[4] is used

[2] Strictly speaking, the two-photon linewidth is relevant for EIT. Using Rydberg EIT, the combined linewidth can be stabilised [144]. For high-n Rydberg states, however, this scheme is prone to systematic errors, e.g. due to electric fields.

[3] For the measurements presented in Chap. 6, a different ECDL (*Toptica DL pro*) with improved performance was used.

[4] A frequency to voltage converter in this frequency range can be realised in various ways. For

to generate an error signal with the zero-voltage offset corresponding to 2.5 MHz. The error signal is fed into an integral-controller which applies feedback to the piezo actuator of the resonator. The loop bandwidth is chosen not to exceed 100 Hz. This is crucial as the frequency comb is not stable at short time scales and special care has to be taken so as not to transfer noise to the cavity. The absolute frequency of the signal laser can be adjusted by choosing the frequency of the local oscillator f_{LO}.

The linewidth of the stabilised signal laser was measured with an independent Fabry-Perot resonator using a side-of-fringe technique. The obtained rms linewidth is less than 100 kHz for integration times shorter than 100 ms. This is a factor of 2 lower than if the same diode laser is directly stabilised to the frequency comb.

The control field is created by frequency-doubling the light originating from a Ti:Sa laser (*Coherent MBR-110*) which is pumped with 12 W from a 532 nm laser (*Coherent Verdi V18*). The Ti:Sa laser is operated at a wavelength of around $\lambda = 950$ nm and has an output power of up to 1.2 W. The light is guided through a lithium-triborat crystal which is placed in a ring resonator (*Toptica SHG pro*). After frequency doubling, up to 360 mW of light at a wavelength of $\lambda = 475$ nm is available. The frequency of the Ti:Sa laser is stabilised to the same Fabry-Perot resonator as the signal laser using a PDH scheme. To this end the light is superimposed with the signal light on a dichroic mirror. The same EOM is used for the phase modulation. The light reflected from the cavity is again spatially separated by a dichroic mirror and detected. Feedback to the Ti:Sa laser is provided through an improved and adapted version of the commercial controller of the laser. The loop bandwidth is 30 kHz.

The linewidth of the light was characterised before and after frequency doubling. The rms linewidth of the Ti:Sa laser obtained from an out-of-loop measurement is approximately 100 kHz at an integration time of 100 ms which translates to an rms linewidth of 200 kHz in the blue spectral region.[5] Improvements to the power and the stability of the laser system can be achieved by creating a slow permanent flow of nitrogen gas through the laser resonator, thereby presumably minimising the disturbing effects of water absorption lines that can be found in the spectral region around $\lambda = 950$ nm.

The second laser system providing light at a wavelength of $\lambda = 475$ nm is a commercially available system (*Toptica TA-SHG-pro*) consisting of an ECDL, a tapered amplifier (TA) and a frequency-doubling stage that is identical to the one used in the Ti:Sa system. It delivers an output power of up to 960 mW at $\lambda = 475$ nm. Frequency stabilisation is achieved by referencing the ECDL to the

example, a frequency counter with analogue output (*Stanford Research Systems, SR620*) can be used. Alternatively, the frequency offset locking scheme demonstrated in Ref. [147] can be applied.

[5] The noise spectrum shows that the largest contribution to rms linewidth stems from the etalon modulation of the Ti:Sa laser. If the etalon modulation is temporarily switched off, then linewidths of below 30 kHz were observed.

Ti:Sa laser. For the Rydberg states used in the experiment the optical frequencies of both lasers typically differ by 20 to 40 GHz before the SHG stages. To stabilise this frequency difference, light from the Ti:Sa laser is phase-modulated with a fibre-based modulator (*Photline NIR-MPQX800*) with frequencies up to 20 GHz and superimposed with light from the ECDL on a fibre-coupled photodiode (*New Focus 1554-A*). The modulation frequency is chosen such that the first or second sideband creates a beat signal at 6.9 GHz. After amplification (*Microwave Solutions MSH55566609*) the signal is mixed (*Minicircuits ZMX-10G+)* with a local oscillator at a frequency of 6.8 GHz. The resulting frequency difference is phase stabilised to a second local oscillator at 100 MHz using a laser controller (*Toptica mFALC*) that provides feedback to the ECDL.

3.3. Beam Geometry

Before the signal and control light reaches the atoms, it passes several optical elements that allow precise control of the spatial, temporal and polarisation mode as well as the exact frequency.

The power of the signal light can be adjusted using an acousto-optic modulator (AOM). Typical rise and fall times are 30 ns. The AOM is set up in a double-pass configuration, which allows rapid frequency sweeping of the signal light over a range of 20 MHz, while only minimally changing the spatial mode of the transmitted light. Subsequently, the light is coupled to a single-mode optical fibre for spatial mode filtering. An electro-optic modulator (EOM, *Qioptiq LM0202 P 5W KD*P*) is used for quickly switching between horizontal and vertical polarisations. The EOM consists of two pairs of KD*P crystals, where one crystal in each pair is rotated by 90° to minimise thermal drifts. The linear polarisation of the incoming light is at an angle of 45° to the optical axis of the crystals. The switching contrast is typically better than 1:100 with rise- and fall-times of 20 ns. A polarisation maintaining fibre guides the light to the experiment. The fibre is aligned such that both linear polarisations a are maintained. Fig. 3.3 illustrates how the light is applied to the atoms. A combination of $\lambda/2$ and $\lambda/4$ waveplates rotates the polarisation such that the signal light is either left-handed (L) or right-handed (R) circularly polarised in front of the glass cell, thereby compensating polarisation changes caused by the optical elements in the beam path. An achromatic corrected lens which is placed at a distance of 130 mm from the atoms focuses the signal beam to a waist of $w_s = 8\,\mu$m at the position of the atoms. A small beam waist is important as it determines how many Rydberg polaritons can propagate next to each other. Ideally, it should be much smaller than the blockade radius R_b such that all transversal degrees of freedom are frozen out and a one dimensional system is realised.

The signal light that is transmitted through or retrieved from the atomic cloud is collected by a lens system with high numerical aperture of NA = 0.19 and coupled to a single-mode optical fibre which guides the light to the detection

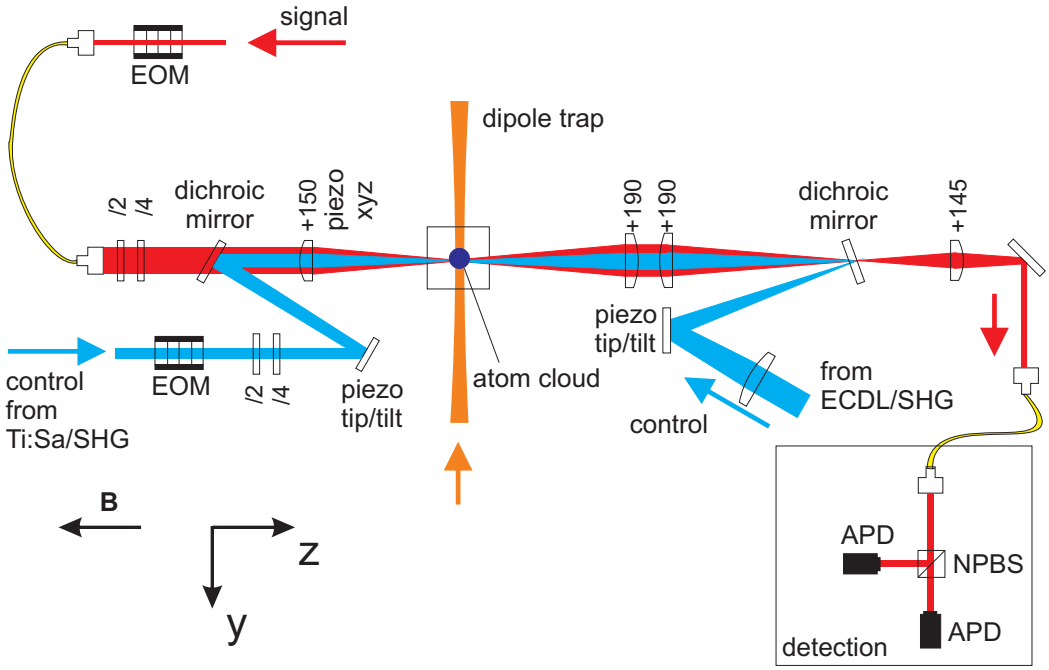

Figure 3.3.: Optical setup for performing Rydberg-EIT experiments. The signal light from an optical fibre is focused onto the atom cloud in parallel to the magnetic field. The control light is superimposed with the signal light on a dichroic mirror focused onto the cloud by the same lens. A second control field can be applied, counter-propagating the signal light. The retrieved light is collected by a lens system coupled to a single-mode optical fibre that guides the light to the detection setup. This consists of two APDs and a non-polarising beam splitter (NPBS) for correlation measurements.

setup.

The power of the control light originating from the frequency-doubled Ti:Sa can be controlled by an AOM in single-pass configuration. Rise- and fall-times are measured to be 30 ns. Similar to the signal beam setup, the polarisation can be rapidly switched between R and L by a combination of an EOM (*Qioptiq LM0202 P VIS KD*P*) and waveplates. The control beam is superimposed with the signal beam on a dichroic mirror. The same lens as the one that is used for the signal light focuses the beam onto the atomic cloud, where it has a spot size of $w_c = 12\,\mu$m. This is a trade-off between two goals. On the one hand, it is necessary to achieve sufficiently high Rabi frequencies at the light power, that is available. On the other hand, the Rabi frequency should be homogeneous across the transverse extend of the probe beam as required for best EIT performance. The transmission of one wall of the glass cell for light at a wavelength of $\lambda_c = 475\,$nm is $T_{\text{cell}} = 0.83$. A mirror can be placed between the lens and the glass cell for optimising the overlap of the two beams on a CCD camera.

The power regulation of the second control beam created by the frequency doubled ECDL/TA system is realised in a manner similar to the first beam. The beam's polarisation at the position of the atoms is statically set by a combination of waveplates. The beam is superimposed with the signal beam in a counter-propagating configuration. To this end, a dichroic beam splitter is placed in the focal point of the lens system (cf. Fig. 3.3). Two achromatic lenses of the detection system focus the beam onto the atomic cloud with a waist of $w_c = 21\,\mu$m. The transmission of the pair of lenses at a wavelength of $\lambda = 475\,$nm is $T = 0.61$.

The detection setup is placed in a lightproof box to which light originating from the atom cloud is guided by an optical fibre. For the detection of light on the single-photon level, avalanche photodiodes (APD, *PerkinElmer SPCM AQR-16*) with a quantum efficiency of 50% and a dark count rate of 30 Hz are used. In order to be able to perform correlation measurements, a non-polarising 50:50 beam splitter and two APDs are used. The probability that a transmitted signal photon is detected is 27%.[6]

Special care has to be taken to ensure that background light impinging onto the detectors is kept to a minimum. The single-mode optical fibre used for detection provides spatial filtering. Spectral filtering can be achieved by a combination of interference filters. Control light at a wavelength of $\lambda = 475\,$nm can efficiently be suppressed using a long-pass filter (*Semrock FF01-515/LP*). The strong control light causes stray light that originates from the glass cell or something inside of it, even in the absence of atomic cloud, and has a broad spectrum in the wavelength region around 795 nm. This can be suppressed by placing two narrow bandpass filters (*Semrock FF01-800/12*) at an angle of 0° and 20° in front of the detectors. The remaining dark count rate is typically 170 Hz.[7]

[6] For the experiments presented in Chap. 6 the detection efficiency is 24% due to modification to the setup.

[7] This value strongly depends on the alignment of the control beams, their power and the duration for which they are switched on. After the control light is switched on, the count rate increases on a time scale of 500 μs before it saturates to a constant value. The quoted number corresponds to a typical control light exposure during experiments.

4. EIT and Storage of Light with Rydberg States

In this chapter characterization measurements of EIT and storage of light with Rydberg states, that are important for a quantitative understanding of the results of Chaps. 5 and 6, are presented. Many of the effects shown are the subject of current research and have only recently been observed by various groups. Chap. 4.1 discusses Rydberg EIT spectra as obtained from our apparatus at very low signal light levels. At higher signal photon rates, Rydberg blockade effects can be observed in EIT which is the subject of Chap. 4.2. Light that is stored in Rydberg states using EIT and subsequently retrieved shows photon antibunching. Experimental data demonstrating this effect can be found in Chap. 4.3. In the single-photon switch experiments of Chap. 5, long coherence times are necessary to retrieve the gate photon at the end of each experiment. This allows to perform postselection which helps in analysing the switch performance. Therefore, Chap. 4.4 reports the experimental progress made in understanding and decreasing decoherence in our system. The electric field at the position of the atoms is a very important quantity due to the high static polarisability of Rydberg atoms. Therefore Chap. 4.5 shows how it can be characterised using Stark spectroscopy based on Rydberg EIT. This makes it possible to apply an electric field of known strength at the position of the atoms.

4.1. EIT with Rydberg States

The foundation of all experiments presented in this thesis is the observation of EIT in our apparatus. Fig. 4.1(a) shows the atomic states of ^{87}Rb that are normally used (cmp. Fig. 2.1(a)). For the states $|g\rangle$ and $|e\rangle$, the hyperfine quantum numbers are good quantum numbers. For the Rydberg state $|r\rangle$, however, the hyperfine splitting can usually be neglected (cf. Tab. 2.1) and it is sufficient to describe the problem in a fine structure basis. The spontaneous decay rate of the state $|e\rangle$ is $\Gamma_e = 2\pi \times 5.75\,\mathrm{MHz}$, where the probability for a decay into state $|g\rangle$ is $\Gamma_{eg}/\Gamma_e = 1/2$. The signal light drives transitions on the D_1 line of ^{87}Rb at a wavelength of 795.0 nm. The control field couples the excited state $|e\rangle$ to the Rydberg states $nS_{1/2}$. The electric dipole matrix element of this transition is given by $d_{re} = e\Xi R_{5P}^{nS}$, where e is the elementary charge. The angular part of the matrix element Ξ can be calculated using angular momentum algebra [127]. For this specific transition, it is $\Xi = \sqrt{2}/3$. The radial matrix elements R_{5P}^{nS}

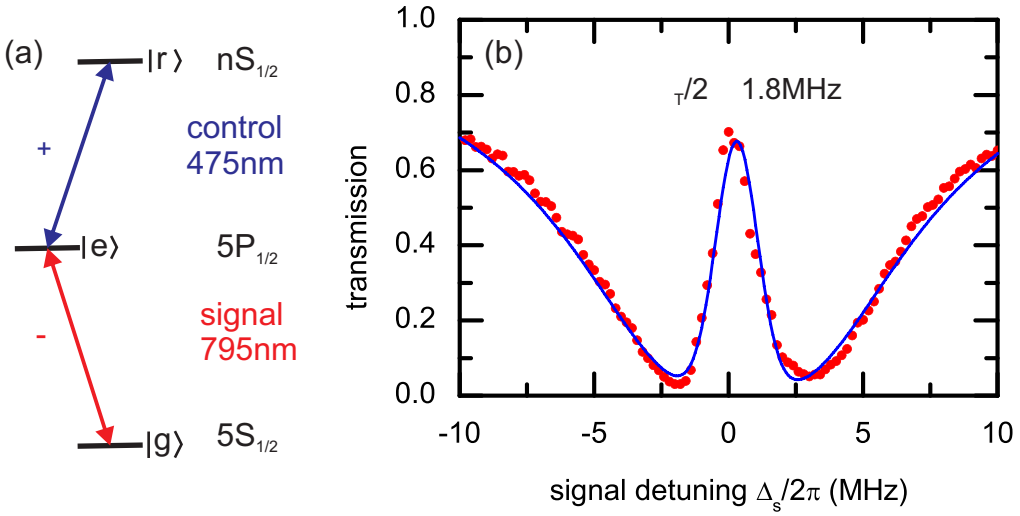

Figure 4.1.: EIT spectrum with the Rydberg state $67S_{1/2}$. (a) EIT level scheme. The hyperfine quantum numbers of the states $|g\rangle$ and $|e\rangle$ are $|F, m_F\rangle = |1, -1\rangle$ and $|F, m_F\rangle = |2, -2\rangle$, respectively. The fine structure quantum numbers of the state $|r\rangle$ are $|J, m_J\rangle = |1/2, +1/2\rangle$. (b) Measured EIT spectrum for Rydberg state $67S_{1/2}$. The control field has a single-photon detuning of $\Delta_c \approx 0$ and a Rabi frequency of $\Omega_c/2\pi = 10\,\mathrm{MHz}$. The solid line shows a fit of Eq. (4.1) to the data.

can be evaluated using Eq. (2.25). The signal pulse is switched on for $200\,\mu$s. The control light is ramped up simultaneously with the signal light and lasts for $220\,\mu$s. The signal pulse can therefore leave the cloud before the control pulse is switched off, even if the signal pulse is delayed due to a reduced group velocity. The experiment is repeated every $t_{\mathrm{cyc}} = 1\,\mathrm{ms}$. A magnetic field of 1.1 G is applied along the z-direction.

A signature of EIT is the appearance of a transparency window in the absorption profile of the atomic cloud due to the presence of the control field. Fig. 4.1(b) shows a transmission spectrum that was recorded using the Rydberg state $67S_{1/2}$ in a co-propagating beam geometry (cf. Fig. 3.3). A transmission peak can clearly be seen in the centre of the spectrum. A low signal photon rate of 1.75 MHz is chosen in order to minimise Rydberg blockade effects that are separately studied in Chap. 4.2.

The EIT spectrum can be analysed using the simple, empirical model

$$T = \exp\left(-\frac{OD}{1 + (2(\Delta_s - \Delta_0)/\Gamma_e)^2}\right) + T_0 \exp\left(-\frac{(\Delta_s - \Delta_1)^2\, 4 \ln 2}{\Delta\omega_T^2}\right). \quad (4.1)$$

The first term is the atomic absorption line with optical depth OD and natural linewidth Γ_e. Δ_s is the detuning of the signal light. Δ_0 is the centre of the line and accounts for shifts of the signal transition, e.g. due to magnetic fields. The second term empirically models EIT by a Gaussian transmission profile with

maximal transmission T_0 and FWHM $\Delta\omega_T$. Δ_1 determines the centre of the EIT window. It is related to the control light detuning Δ_c, but also includes Zeeman shifts.

Fitting Eq. (4.1) to the data in Fig. 4.1(b) yields an optical depth of $OD = 5$. For comparison, the parameters of the cloud can be used to estimate the transmission averaged over the transverse beam profile $\langle T \rangle$. Equating this with $\langle T \rangle = e^{-OD}$ yields $OD = 8$ for an atom number of 1.5×10^5 and a temperature of $T = 0.33\,\mu\mathrm{K}$. The agreement is fair considering that the optical depth obtained from the fit is prone to systematic errors. The reason for this is the diffraction due to the inhomogeneity of the atomic cloud combined with the spatial mode filtering of the detection fibre. The fit yields a maximal EIT transmission of $T_0 = 0.67$ at a linewidth of $\Delta\omega_T/2\pi = 1.8\,\mathrm{MHz}$. The linewidth is much smaller than the natural linewidth of the transition Γ_e. The agreement with the theoretical prediction of Eq. (2.7) which yields $\Delta\omega_T/2\pi = 6.4\,\mathrm{MHz}$ is moderate. One possible reasons for this is an imperfect overlap between signal and control beam leading to a reduced Ω_c.

Ideally, the transmission on EIT resonance should be close to unity. Various effects can lead to a reduced EIT transmission and a broadening of the line. Assuming that the imperfect EIT is due to Markovian dephasing of ρ_{rg} or Lorentzian laser line shapes (cf. Chap. 2.1.1), we can use the model $T = \exp(-OD\,\mathrm{Im}(\chi)/\chi_0)$ with χ from Eq. (2.4) to extract the dephasing rates. A fit to the EIT spectrum in Fig. 4.1(b) with $\gamma_{eg}/2\pi = 5.75\,\mathrm{MHz}$ yields a dephasing rate of the Rydberg state relative to the ground state of $\gamma_{rg}/2\pi = 0.5\,\mathrm{MHz}$. We compare this result to the measured rms laser linewidths of $\sigma_s/2\pi = 0.1\,\mathrm{MHz}$ and $\sigma_c/2\pi = 0.2\,\mathrm{MHz}$ for the signal and control laser, respectively (cf. Chap. 3.2). Assuming that the noise spectra of the lasers are Gaussian and that they can be approximated by a Lorentzian with the same FWHM, we obtain the estimate $\gamma_{eg} \approx \sqrt{8\ln 2}(\sigma_s + \sigma_p) = 2\pi \times 0.7\,\mathrm{MHz}$. This suggests, that the maximal EIT transmission and the width of the EIT window is limited by the laser linewidths.

4.2. Rydberg blockade in EIT with Rydberg states

Rydberg blockade can directly be observed in EIT with Rydberg states. It manifests itself in a saturation of the transmitted signal photon rate for an increasing incident signal light power [97] and in the photon statistics of the transmitted signal light [99]. Understanding the saturation is important because it limits the performance of the single-photon switch as detailed in Chap. 5.

The saturation of transmitted signal photon rate can be understood qualitatively from a simple picture. On EIT resonance, a single signal photon can ideally be transmitted through the cloud without absorption. However, if several photons enter the medium, then due to Rydberg blockade, only one atom can be excited to the Rydberg state and contribute to the dark state polariton.

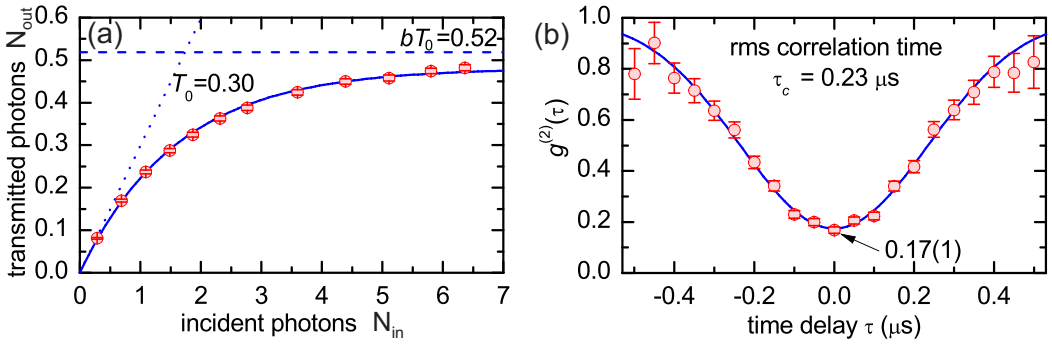

Figure 4.2.: Rydberg blockade for copropagating excitations. (a) Rydberg blockade causes a non-linear absorption for signal photons transmitted on EIT resonance. The signal pulse duration is kept fixed. For small N_{in}, the number of transmitted photons is linear in N_{in} (dotted line). For large N_{in}, however, the number of transmitted photons levels off and approaches a constant value (dashed line) due to Rydberg blockade. The solid lines shows a fit of Eq. (4.2) to the data. (b) The $g^{(2)}$ correlation function of the transmitted light (here for $N_{\text{in}} = 1.7$) exhibits strong photon antibunching as a consequence of the Rydberg blockade. The solid line shows a Gaussian fit.

All other atoms act as resonant two-level atoms and absorb the excess photons. This is true as long as the cloud is much smaller than the blockade radius. But even if this restriction is dropped, a saturation can still be observed because in a finite size medium a limited number of Rydberg atoms can be excited at typical distances on the order of the blockade radius.

In order to be able to observe blockade effects, we now use the Rydberg state $100S_{1/2}$, which has a larger C_6 coefficient compared to the state $67S_{1/2}$ used in the previous chapter and therefore shows more pronounced Rydberg blockade. The experiment is performed with a thermal cloud consisting of 2.2×10^5 atoms at a temperature of $0.43\,\mu$K. An optical depth of $OD = 15$ is inferred from a measured of an EIT spectrum and shows fair agreement with $OD = 10$ calculated from the parameters of the cloud. The control power is $P_c = 32\,$mW resulting in a measured EIT transmission window of $\Delta\omega_T/2\pi = 4.0\,$MHz. For the parameters given, Eq. (2.48) yields a blockade radius $R_b = 14\,\mu$m.

During the experimental sequence, the control light is switched on for $1\,\mu$s. The signal light is ramped up simultaneously, but only lasts for $t_s = 0.4\,\mu$s. The signal pulse can therefore leave the cloud before the control pulse is switched off (cf. Chap. 4.1). This pulse sequence is repeated every $t_{\text{cyc}} = 100\,\mu$s. A magnetic field of $\sim 0.2\,$G along the z axis preserves the spin orientation.

In the experiment, the number of incoming signal photons N_{in} is varied and the number of transmitted photons N_{out} recorded on EIT resonance. The results are shown in Fig. 4.2(a). At low signal intensities, N_{out} is proportional to N_{in} with a proportionality factor of $T_0 = 0.30$. T_0 is the maximal EIT transmission in the limit of low signal photon numbers. N_{out} levels off for higher N_{in} as

a consequence of Rydberg blockade. The solid line shows a fit of a simple model [103]

$$N_{out} = bT_0 \left(1 - e^{-N_{\text{in}}/b}\right) \tag{4.2}$$

to the data. The model is one-dimensional which is justified as the blockade radius $R_b = 14\,\mu$m is larger than the transversal extension of the signal beam $w_s = 8\,\mu$m (cf. Chap. 3.3). The light pulse is divided into b bins of equal duration. In each bin, only one photon experiences an overall transmission of T_0, whereas all extra photons are subject to absorption due to the Rydberg blockade. Since the absorption length $l_a = 1/\sigma\varrho \approx 5\,\mu$m, where σ is the resonant absorption cross-section of the signal transition and ϱ the atom density[1], is short compared to $2R_b$, it can be assumed that all extra photons are completely absorbed. The best-fit values obtained are $b = 1.7$ for the number of bins[2] and $T_0 = 0.30$ for the maximal EIT transmission. The number of transmitted photons therefore saturates at $bT_0 = 0.51$.

Antibunching in the transmitted light. The Rydberg blockade can also be observed when studying the normalised second-order correlation function $g^{(2)}(\tau)$ of the transmitted photons. In order to detect correlations, a non-polarising beam splitter and two single-photon detectors are used (cf. Fig. 3.3). In the experiment, detection events at the two detectors with a time delay of τ are counted and normalised to the average photon rate.

Fig. 4.2(b) shows $g^{(2)}(\tau)$ evaluated for the same data as shown in Fig. 4.2(a) at $N_{\text{in}} = 1.7$. The correlation function exhibits antibunching with $g^{(2)}(0) = 0.17(1)$. This gives evidence that the transmitted light is non-classical unlike the incoming light that is derived from a laser where $g^{(2)}(\tau) = 1$ for all τ. The solid line shows a Gaussian fit to extract the rms correlation time $\tau_c = 0.23\,\mu$s. We compare this to the prediction in Ref. [99] $\tau_c = 1.05\sqrt{8OD}/\gamma_{\text{EIT}} = 0.12\,\mu$s. The agreement is fair. The deviation might be due to the inhomogeneity of the medium. Note that τ_c is quite different from the simple estimate $R_b/v_g \sim 0.05\,\mu$s obtained from the group velocity $v_g = \sqrt{2\pi}\sigma_z/t_{\text{delay}} = 0.3\,$km/s, where σ_z is the rms radius of the cloud in the direction of propagation and $t_{\text{delay}} = 0.25\,\mu$s is the measured group delay. This is likely due to the fact that propagation effects cannot be neglected as discussed in Ref. [99].

[1] Here, we approximate the medium as homogeneous with density $\varrho = \varrho_p/2$, where ϱ_p is the peak atomic density.

[2] The number of bins $b = 1.7$ agrees well with the simple estimate $b \approx t_s/\tau_c = 1.7$, obtained from the signal pulse duration t_s divided by the measured rms width $\tau_c = 0.23\,\mu$s of the antibunching feature in Fig. 4.2(b).

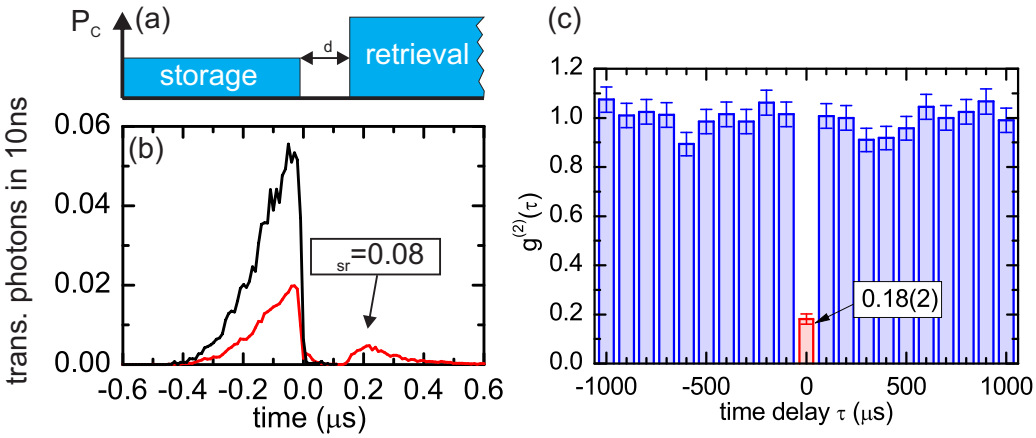

Figure 4.3.: Rydberg blockade in the storage and retrieval using the Rydberg state $100S_{1/2}$. (a) Timing diagram for the control field. The control power P_c is a factor of 2 larger for the retrieval than for the storage. (b) Transmitted signal photons with (red line) and without atoms (black line). The incoming light pulse contains on average $N_{in} = 1.0$ photons. The stored light pulse can be retrieved with an efficiency of $\eta_{sr} = 0.08$ after a dark time of $\tau_d = 0.15\,\mu$s. (c) $g^{(2)}$ correlation function for the retrieved light. The data is binned over the whole retrieved light pulse. For an incoming photon number of $N_{\mathrm{in}} = 1.0$, a pronounced antibunching is observed.

4.3. Rydberg blockade in Storage and Retrieval of Light

Rydberg blockade can also be observed in the storage and retrieval of light with Rydberg states. Here, it leads to antibunching in the retrieved light. This mechanism can therefore be utilised to build single-photon sources [98, 100].

To demonstrate this effect, a storage and retrieval experiment is performed using the Rydberg state $100S_{1/2}$. The parameters of the atomic cloud are the same as in the correlation measurements in Chap. 4.2. In contrast to the level scheme of Fig. 4.1(a), however, the states $|F, m_F\rangle = |2, 0\rangle$ and $|J, m_J\rangle = |1/2, -1/2\rangle$ are used for $|e\rangle$ and $|r\rangle$, respectively.[3] The angular parts of electric dipole matrix elements are $\Xi_s = 1/3$ and $\Xi_c = 1/\sqrt{12}$ for the signal and the control transition [127].

The storage and retrieval sequence is shown in Figs. 4.3(a) and (b) for $N_{in} = 1.0$ incoming photons on average. First, the control field is switched on with a power of $P_c = 16\,\mathrm{mW}$ to make the medium transparent for the signal light due to EIT. Next, the signal light pulse is applied. It is shaped as a Gaussian that is cut off in the centre (Fig. 4.3(b), black curve).[4] Without cutting, its rms width would be $t_s = 0.2\,\mu$s. This is short compared to τ_c in Fig. 4.2(b). Therefore,

[3] These states are also used in the switch experiment in Chap. 5 for the gate photon.
[4] This shape was found to optimise storage and retrieval efficiencies [107].

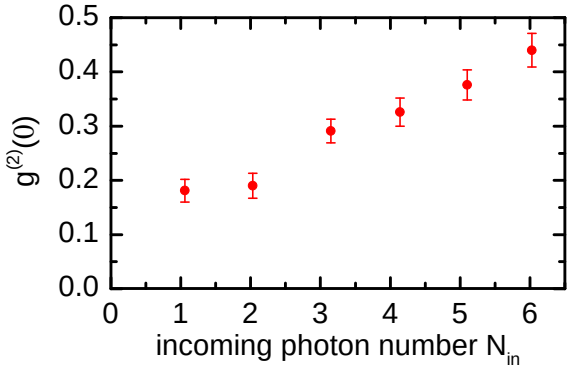

Figure 4.4.: Antibunching in retrieved light. $g^{(2)}(0)$ increases as a function of incoming photon number N_{in}. For higher N_{in}, the probability of creating more than one Rydberg excitation increases due to imperfect longitudinal blockade.

$g^{(2)}(\tau)$ is close to its minimal value for the whole pulse. We thus expect a small $g^{(2)}$, even if we bin over the complete light pulse.

The wavelength of the signal field is set such that the two-photon resonance condition $\delta_2 = 0$ for EIT is fulfilled. As a consequence, the light pulse is slowed down and compressed in the medium. The control laser is switched off simultaneously with the signal pulse with a ramp time of 30 ns, in order to store the light pulse. After a dark time of $\tau_d = 0.15\,\mu$s, the control light is switch on again for the retrieval of the light pulse[5].

Experimental results are shown in Fig. 4.3(b) (red line). The first peak shows an undesired non-zero transmission during the gate pulse due to imperfect storage. The second peak is light that is retrieved from the cloud with a storage and retrieval efficiency of $\eta_{sr} = 0.08$. The Rabi frequency of the control light was optimised for high η_{sr} (see also Ref. [107]). Several imperfections limit η_{sr}: The transmission on EIT resonance is measured to be $T_0 = 0.46$ and thus considerably affects η_{sr}. The measured optical depth of $OD = 3.2$, combined with an EIT linewidth of $\Delta\omega_T/2\pi = 3.3\,$MHz, leads to an insufficient compression of the light pulse and thus the storage efficiency is further reduced.[6]

We now analyse the photon statistics of the retrieved light by evaluating the normalised second order correlation function $g^{(2)}(\tau)$. τ is now an integer multiple of the cycle period $t_{\text{cyc}} = 100\,\mu$s and the data is binned over the whole retrieved pulse from $t = 0.14\,\mu$s until $0.34\,\mu$s (cf. Fig. 4.3(b)). Results are shown in Fig. 4.3(c). Photon antibunching is clearly visible. The imperfect suppression of $g^{(2)}(0)$ is consistent with a cloud that is longer than the blockade radius. For the given parameters of the ensemble, the rms radius of the cloud along the

[5]The power and length of the control pulse is chosen such that the cloud experiences the same repulsive potential (cf. Chap. 3.1) as in the experiments in Chap. 5

[6]η_{sr} strongly depends on the Rydberg state used. Lower principal quantum numbers usually reduce dephasing. As a consequence, higher storage and retrieval efficiencies are achieved.

direction of propagation is $\sigma_z = 28\,\mu$m, which is larger than the blockade radius of $R_b = 18\,\mu$m. Transversally, however, the transmission is well blocked because the waist of the signal beam of $8\,\mu$m is much smaller than the blockade radius.

Further experimental evidence for this conclusion is provided by Fig. 4.4, where $g^{(2)}(0)$ is shown as a function of the number of incoming photons. The suppression of $g^{(2)}(0)$ becomes weaker for higher photon numbers. This again agrees with the fact that the medium is longer than the blockade radius. In this situation the probability of storing more than one photon increases for higher incoming photon numbers and $g^{(2)}(0)$ increases along with it.

4.4. Decoherence in Storage and Retrieval of Light

In storage and retrieval experiments, like the one shown in Fig. 4.3(b), the storage and retrieval efficiency η_{sr} decays as a function of dark time τ_d due to dephasing. For many applications, such as the experiments in Chap. 5, long coherence times are important. Therefore, decoherence mechanisms that affect η_{sr} are discussed in this chapter.

In order to experimentally determine the dephasing rate, $N_{\text{in}} \approx 1$ photons are stored in the atomic cloud and retrieved after a dark time τ_d. The number of retrieved photons N_{out} is measured as a function of τ_d and an exponential decay with time constant τ_{dec} is fitted to the data (cf. inset in Fig. 4.5). The dephasing rate is then defined as $1/\tau_{\text{dec}}$.

The experimental data in Fig. 4.5 show that the dephasing rate depends linearly on the density ϱ of the surrounding ground-state atoms.[7] This can be attributed to a shift of the Rydberg state due to elastic collisions of the Rydberg electron with the ground-state atoms.

Such shifts were first observed in the absorption spectra of highly excited sodium atoms [148] and can qualitatively explained by a simple picture. For the Rydberg state $100S_{1/2}$, the valence electron is delocalised over a distance of $\sim 1\,\mu$m, as can be seen in Fig. 2.2. The electron spends most of the time close to the classical turning radius, where it becomes quasi-free. At high ground-state atom densities the spatial extend of the electron wavefunction is larger than the mean interatomic distance, so that interactions between the electron and the ground state atoms start to play a role. As the electron is very slow close to the classical turning point, only s-wave scattering takes place between the electron and a ground state atom. The interaction potential can thus be described by the Fermi pseudo potential [149]

$$V_{\text{Fermi}}(\boldsymbol{r}) = \frac{2\pi\hbar^2 a}{m_e}\,\delta(\boldsymbol{r}), \tag{4.3}$$

[7] The transitions shown in Fig. 4.1(a) were used. The power of the control light was $P_c = 17\,\text{mW}$ for storage and retrieval.

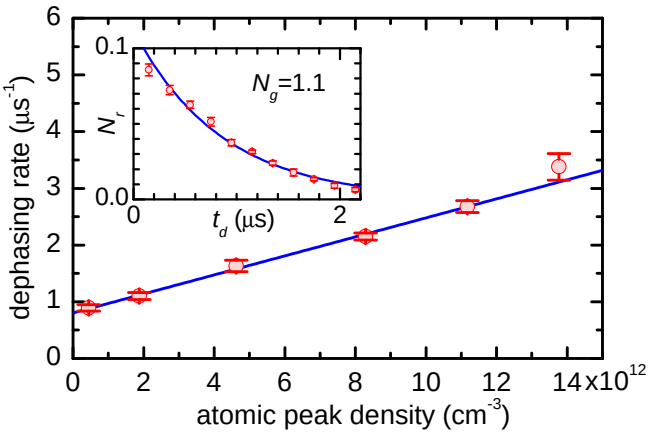

Figure 4.5.: Density dependent dephasing of the coherence between the Rydberg state $100S_{1/2}$ and the atomic ground state. The measured dephasing rate increases linearly with atomic density. Inset: measurement of the dephasing rate at a peak density of $\sim 2 \times 10^{12}\,\mathrm{cm}^{-3}$, where the experiment is normally operated. The retrieved photon number N_r decays as a function of dark time τ_d. An exponential fit yields the $1/e$ dephasing rate.

where m_e is the electron mass and r is the distance between the electron and the ground-state atom. a is the s-wave scattering length for the collision of an electron with a neutral ground state atom. For the $5S_{1/2}$ ground state of ^{87}Rb it is $0.627a_0$ and $-16.1a_0$ for the singlet and triplet channel, respectively [150].

If the number of atoms within the electron wavefunction is high, a mean field approach can be pursued which predicts an energy shift of the Rydberg state [149, 151]

$$\hbar\Delta_m = \frac{2\pi\hbar^2 a}{m_e}\,\varrho \tag{4.4}$$

that is proportional to the particle density ϱ. For densities of $\varrho = 1 \times 10^{13}\,\mathrm{cm}^{-3}$, Eq. (4.4) yields $\Delta_m/2\pi \approx 0.04\,\mathrm{MHz}$ and $\Delta_m/2\pi \approx -1\,\mathrm{MHz}$ for the singlet and triplet scattering length, respectively. The experimental observation of such an energy shift in an ultracold gas of ^{87}Rb atoms has recently been reported in Ref. [151].

Note that the mean field result (4.4) is independent of the principal quantum number. For low principal quantum numbers or low atomic densities, however, the mean-field approximation breaks down.[8]

In our experiment, the atom density is not homogeneous. As a consequence, the phase evolution of the Dicke state $|D_1^{N-1}\rangle$ in Eq. (2.12) is inhomogeneous across the sample which results in a spatial dephasing of $|D_1^{N-1}\rangle$. A detailed explanation and a theoretical model can be found in App. A. The model predicts a linear dependence of the dephasing rate on the peak atom density in agreement

[8] The situation, where the number of ground state atoms within the electronic wavefunction is ~ 1, is studied separately in App. C.

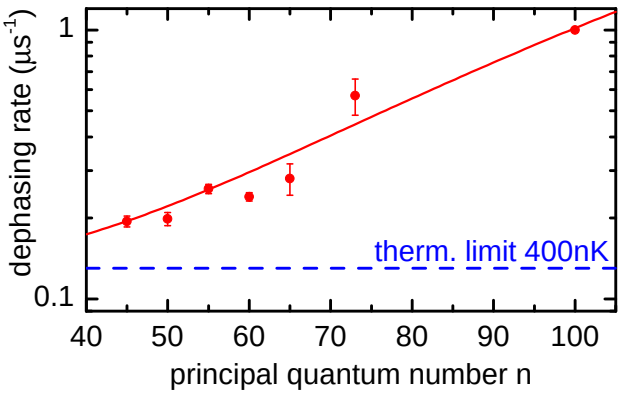

Figure 4.6.: Dependence of dephasing rate on the principal quantum number. For lower principal quantum numbers the dephasing rate approaches the dephasing rate estimated from the temperature of the cloud (blue dashed line). The solid red line shows a fit of a power law $1/\tau = 1/\tau_{\mathrm{therm}} + A \cdot (n^*)^a$ to the data.

to the experimental observation. Fitting a linear function to the data in Fig. 4.5 yields a slope of $0.17\,\mu\mathrm{m}^3/\mu\mathrm{s}$. This matches quite well the theoretical estimate of $0.18\,\mu\mathrm{m}^3/\mu\mathrm{s}$ (cf. App. A). The dephasing rate at zero density obtained from the fit is $1/\tau_{\mathrm{dec}} = 0.8\,\mu\mathrm{s}^{-1}$. According to Eq. (2.14), the dephasing rate due to thermal motion is expected to be $0.14\,\mu\mathrm{s}^{-1}$ for a copropagating beam geometry and a temperature of $\sim 450\,\mathrm{nK}$. Indeed, if we change the beam geometry from copropagating to counter propagating, we do not observe longer coherence times in spite of the fact the recoil is reduced by a factor of 4. This suggests that further decoherence mechanisms play a role.

Fig. 4.6 shows how the dephasing rate depends on the principal quantum number n.[9] At $n = 45$ a dephasing rate of $0.19(1)\,\mu\mathrm{s}^{-1}$ is observed, which is close to the theoretical estimate $1/\tau_{\mathrm{therm}} \sim 0.13\,\mu\mathrm{s}^{-1}$ for dephasing due to the thermal motion of the atoms. Subtracting $1/\tau_{\mathrm{therm}}$ from the data and fitting a power law yields an exponent of $a = 3.3(4)$. If the dephasing were due to electric field gradients, we would expect an exponent between 6 and 7 (cf. Chap. 2.2.3) in the limit of the quadratic Stark effect. We numerically find that an exponent of 6.5 is obtained at an electric offset field of $\sim 25\,\mathrm{mV/cm}$ (cf. Chap. 4.5). The origin of the measured scaling behaviour is thus unclear.

Similar experiments reported in Ref. [98] used a magnetic field of 4.3 G and observed a dephasing rate of $0.4(1)\,\mu\mathrm{s}^{-1}$ for the $90S_{1/2}$, which is consistent with the decoherence expected from atomic motion because Ref. [98] operated at higher temperature. If a magnetic field of 1.3 G is applied in our experiment

[9] The data were taken at peak atomic densities of around $\varrho_p \sim 2{\times}10^{12}\,\mathrm{cm}^{-3}$ and temperatures of approximately $T \sim 0.4\,\mu\mathrm{K}$. The control power was optimised for best retrieval efficiency for each data point. A magnetic field of $\sim 0.2\,\mathrm{G}$ was applied. We experimentally verify that the dephasing rate does not depend on the number of incoming photons. Typically we use $N_{in} \sim 6$.

and the electric field is reduced by a factor of two to 12 mV/cm, a dephasing rate of better than $1/\tau_{\mathrm{dec}} = 0.5\,\mu\mathrm{s}^{-1}$ is observed for the $100S_{1/2}$ state. This suggests that a spatially inhomogeneous electric field might partly be responsible for the observed decoherence.

4.5. Stark Spectroscopy using EIT

Rydberg atoms are very sensitive to electric fields. As can be seen in Fig. 2.3, at electric fields as small as $\sim 50\,\mathrm{mV/cm}$ the state, adiabatically connected to the $100S_{1/2}$ state at zero field, crosses the hydrogenic manifold which leads to a strong state mixing. Therefore knowledge of the electric fields present in the experiment is very important and their compensation desirable.[10] The amplitude of the electric field at the position of the atoms can be determined by measuring the Stark splitting of the $nD_{3/2}$ Rydberg state using EIT. By properly choosing the principal quantum number n, the sensitivity of this measurement can be adjusted. In the example shown here, we use the Rydberg state $90D_{3/2}$. The signal light drives the transition from $|F, m_F\rangle = |1, -1\rangle$ to $|F, m_F\rangle = |2, 0\rangle$ of the D_1 line of ^{87}Rb. The control field is σ^- polarised and therefore couples to the $m_J = -1/2$ and $m_J = -3/2$ Zeeman sublevels of the $90D_{3/2}$ state. A magnetic field of $B \sim 1.1\,\mathrm{G}$ is applied along the z direction and causes a Zeeman splitting of these states of $\Delta_B/2\pi = g_J\mu_B B/h = 1.2\,\mathrm{MHz}$, where $g_J = 4/5$ is the Landé factor and μ_B the Bohr magneton.

Even if we do not deliberately apply an electric field, stray electric fields are present in our experimental setup. Together with the magnetic field, they cause a measured level splitting of the states with $m_J = -1/2$ and $m_J = -3/2$ of $\Delta_{\mathrm{split}}/2\pi = 3.8\,\mathrm{MHz}$ (see inset in Fig. 4.7). Although the fields are not parallel, we simply subtract the estimated Zeeman splitting $\Delta_B/2\pi = 1.2\,\mathrm{MHz}$ and compare the result to a numerically calculated Stark spectrum. This yields an electric field of $\sim 25\,\mathrm{mV/cm}$.

This stray electric field can be partially compensated by an externally applied electric field. To this end, we use the optical table and the dB_y/dx-gradient compensation coils of our apparatus (cf. Fig. 3.1) as the electrodes. This should predominantly create an electric field along the x direction. But the surrounding coils of the magnetic trap drastically shield the electric field such that no additional Stark effect at the position of the atoms is observed. If the voltage, however, is only switched on for the short $2.5\,\mu\mathrm{s}$ of the EIT experiment, the shielding is incomplete and the Stark splitting is altered.[11]

[10] If all electric offset fields are compensated, then the Stark effect is quadratic and, for example, dephasing of the Dicke state (2.12) due to electric field gradients is only a second order effect.

[11] Like in a Faraday cage, shielding arises from a rearrangement of charges in the copper of the coils. During the rearrangement, electric currents have to flow. The time scale for reaching a new steady state depends on the paths these currents take. If they have to flow through the coils, then this time scale is given by the pulse response time τ_{resp} of the

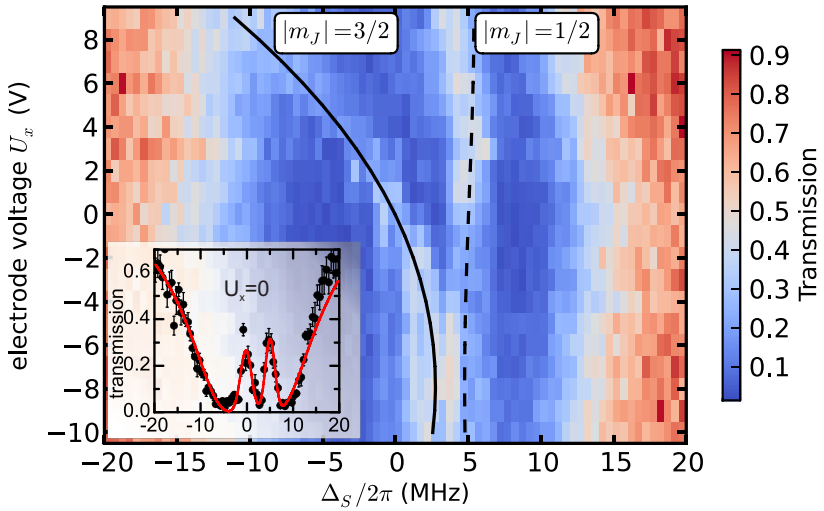

Figure 4.7.: Stark spectrum of the state $90D_{3/2}$. The graph shows EIT transmission spectra for different applied electrode voltages U_x. The lines are numerically calculated Stark spectra. The dashed (solid) line shows the expected resonance position for the $|m_J| = 1/2$ ($|m_J| = 3/2$) state. The relation between electric field E_x and applied voltage is given by $E_x = (U_x - U_{x,0})/\xi$. The parameters $\xi = 2.8 \times 10^{-3}\,\mathrm{cm}^{-1}$ and $U_{x,0} = -7.9$ are obtained from a fit (see text). A theoretical estimate for ξ can be found in Ref. [152].

Fig. 4.7 shows how the measured EIT transmission spectra change if a voltage U_x is applied at the electrodes. Two EIT transmission windows are visible corresponding to the $m_J = -1/2$ and $m_J = -3/2$ Zeeman sublevels of the $90D_{3/2}$ state. By fitting the model of Eq. (4.1), extended by a second EIT window, to the data, the EIT line positions can be extracted. If the numerically calculated Stark spectrum is fitted to the obtained resonance positions,[12] the electric field components along and perpendicular to the x direction, E_x and E_{yz}, can be determined. The fit yields $E_x = 0$ at an applied voltage of $U_{x,0} = -7.9\mathrm{V}$. The remaining electric field is $E_{yz} = 12\,\mathrm{mV/cm}$.

The Stark spectrum in Fig. 4.7 also shows that the transmission on EIT resonance decreases and the linewidth increases at electrode voltages U_x cor-

circuit formed by the inductance of the coils $L \sim 10\,\mu\mathrm{H}$ and their resistance $R \sim 10\,\mathrm{m}\Omega$. This yields approximately $\tau_{\mathrm{resp}} = L/R \sim 1\,\mathrm{ms}$. If after a fast ramp-up of the electrode voltage the steady state has not yet been reached, the shielding is imperfect. Further details can be found in Ref. [152].

[12] For the numerically obtained eigenenergies of the states with $|m_J| = 1/2$ and $|m_J| = 3/2$, a set of functions $\omega_{i,\mathrm{num}}(E)$ with $i \in \{1/2, 3/2\}$ can be created by interpolation. Here, E is the electric field. The fit function is then given by $\omega_{\mathrm{fit},i} = \omega_{\mathrm{num},i}\left(\sqrt{E_x^2 + E_{yz}^2}\right) + \Delta_0$ with $E_x = \xi(U_x - U_{x,0})$. The free fit parameters are the electric field in the yz plane E_{yz}, the electric field along the x axis per applied voltage ξ, the electrode voltage $U_{x,0}$ corresponding to $E_x = 0$ and a detuning Δ_0 that determines the centre of the EIT line at zero electric field.

responding to higher electric fields. This indicates that decoherence becomes larger at higher electric fields. The reason for this is unclear.

One can only speculate about the origin of the stray electric field at $U_x = 0$. Stray charges on the surface of the glass cell, which is only 1.5 cm away from the atoms, are a potential sources of electric fields.

5. Single-Photon Switch based on Rydberg Blockade

This chapter presents the experimental realisation of a single-photon switch based on Rydberg blockade. Most of these results have been published in Ref. [103]. The chapter starts with a brief introduction in Chap. 5.1, explaining the basic concept of the switch. This is followed, in Chap. 5.2, by a description of the experimental sequence and how a switch can be implemented in an ultracold cloud of ^{87}Rb. In Chap. 5.3, the experimental results demonstrating the single-photon switch are shown and discussed. Chap. 5.4 shows how the switch can be used to measure the lifetime of the Rydberg blockade. The single-photon switch relies on the suppression of undesired retrieval of light that is stored in the atomic ensemble. The performance of the polarisation switching scheme that is used for this purpose is discussed in Chap. 5.5.

5.1. Basic Concept

The strategy that is used to realise a single-photon switch is visualised by the cartoon illustration in Fig. 5.1. An atomic medium is made transparent for signal light by Rydberg EIT. Therefore, a target light pulse sent through the medium experiences high transmission. If, however, a gate pulse that contains one incoming photon on average is sent into the atomic cloud and stored as a Rydberg excitation using the storage of light techniques explained in Chaps. 2.1.2 and 4.3, then the medium becomes opaque due to Rydberg blockade. If now a target light pulse is sent through the medium, it gets absorbed. After the application of the target pulse, the stored gate excitation can be retrieved from the medium.

To achieve a good switching contrast, two conditions have to be fulfilled. Firstly, the target photons must not be able to pass the blockaded volume in the transverse direction. We ensure this by focusing the signal light to a waist which is smaller than the blockade radius $w_s \lesssim R_b$. Secondly, the target light has to experience substantial absorption if a Rydberg excitation was created in the medium. Hence, the absorption length for the signal target light $l_{a,t} = 1/\sigma\varrho$ has to be short compared to twice the blockade radius, i.e. $l_{a,t} \ll 2R_b$. Here, $\sigma = 3\xi_t\lambda_s^2/2\pi$ is the absorption cross section for the signal target light with wavelength λ_s, the branching ratio ξ_t and ϱ the atom density.

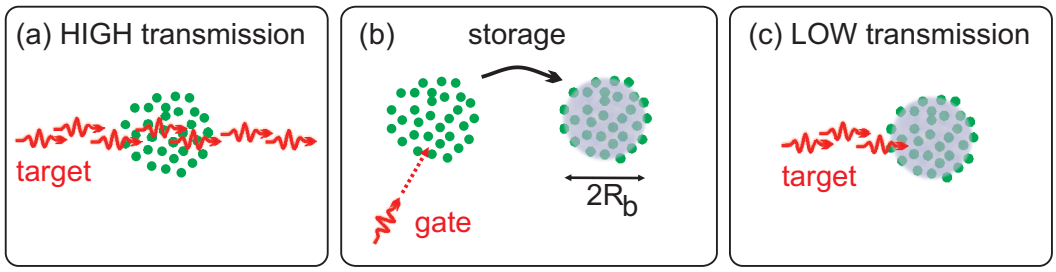

Figure 5.1.: Cartoon illustration of a single-photon switch. (a) The medium is normally transparent for the target light. (b) The gate photon is stored in the atomic cloud as a Rydberg excitation. Within the blockade sphere (blue) with radius R_b the medium becomes opaque. (c) The target photons are absorbed.

5.2. Experimental Sequence

This chapter describes how the single-photon switch is implemented in our experiment, using the Rydberg state $100S_{1/2}$. In particular, the exact timing sequence is presented, the choice of the atomic levels is discussed and finally important parameters are listed. Note that the characterisation measurements, shown in Chaps. 4.2 and Chaps. 4.3, were performed in the same parameter regime as the experiments presented here.

Fig. 5.2(a) shows the timing sequence of the incoming light pulses. The signal gate pulse has the shape of a Gaussian that is cut off in the centre. Without cutting, its rms width would be 0.2 μs. After a dark time $\tau_d = 0.15\mu$s, the signal target pulse is applied. A light pulse at the control wavelength, with power of $P_{c,s} = 16\,\mathrm{mW}$, is used to store the gate pulse in the form of a Rydberg excitation (cf. Chap. 4.3). A second control light pulse with a power of $P_{c,t} = 32\,\mathrm{mW}$ creates EIT for the target light. A third control light pulse with the same power is used to retrieve the gate Rydberg excitation from the cloud. This gate-target sequence is repeated with a cycle repetition time of $t_{\mathrm{cyc}} = 100\,\mu$s. The control beam originates from the Ti:Sa-SHG laser system and copropagates with the signal beam (cf. Fig. 3.3).

The target control light must be prevented from reading out the stored Rydberg excitations. Fig. 5.2(b) shows how this is achieved by using orthogonal polarisations for the gate and target pulse. The gate photon is stored in the Rydberg state $|r_g\rangle$ with quantum numbers $|J, m_J\rangle = |1/2, -1/2\rangle$ using σ^- polarised control light. During the dark time, the polarisation of the control field is switched to σ^+. Hence the target control light cannot couple the stored Rydberg excitations to any state in the $5P_{1/2}$ manifold, because such a state would require $m_J = -3/2$ contradicting $J = 1/2$. For the retrieval, the polarisation is switched back to σ^-. Note that this scheme cannot be implemented with $|e_t\rangle = |5P_{3/2}\rangle$ and thus the D_1 line of ^{87}Rb is used for the signal light.

To improve the performance of the single-photon switch, the signal light is

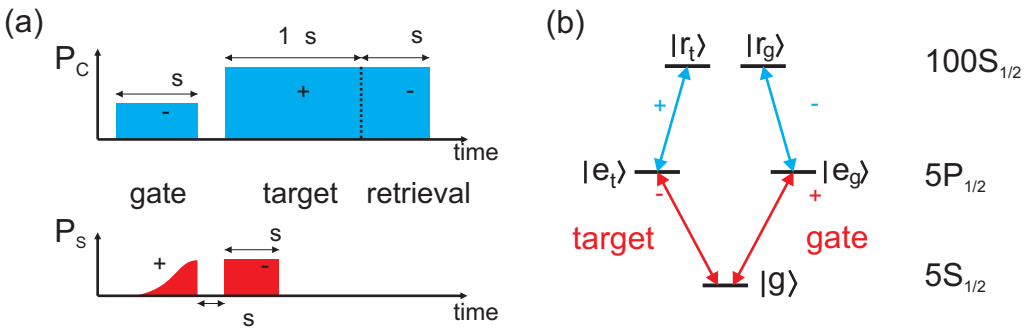

Figure 5.2.: (a) Timing of incoming light (see text). (b) Atomic level scheme for the single-photon switch. The signal light with polarisations σ^+ and σ^- couples the ground state $|g\rangle = |5S_{1/2}, F = 1, m_F = -1\rangle$ with the excited states $|e_g\rangle = |5P_{1/2}, F = 2, m_F = 0\rangle$ and $|e_t\rangle = |5P_{1/2}, F = 2, m_F = -2\rangle$ for the gate and the target pulse, respectively. The control light with polarisations σ^- and σ^+ couples the states $|e_g\rangle$ and $|e_t\rangle$ with the Rydberg states $|r_g\rangle = |100S_{1/2}, m_J = m_I = -1/2\rangle$ and $|r_t\rangle = |100S_{1/2}, m_J = +1/2, m_I = -3/2\rangle$.

switched from σ^+ for the gate to σ^- for the target pulse. The reasons for this are based on the following considerations. On the one hand, good switching contrast requires the absorption length for the target light $l_{a,t} = 1/\varrho\sigma$ to be short compared to the blockade radius $R_{b,t}$. This suggests that a large atomic density should be used. On the other hand, a large retrieval efficiency for the gate excitation can only be achieved at low atomic densities due to the dephasing effects discussed in Chap. 4.4. In fact, we choose the peak atomic density to be $\sim 2.4 \times 10^{12}\,\mathrm{cm}^{-3}$ to keep the dephasing to a minimum, as can be seen in Fig. 4.5. At these densities, we must choose a target signal transition with large absorption cross section σ to obtain a sufficiently short absorption length. We therefore choose σ^- polarised target light such that the strongest available transition on the D_1 line with a branching ratio of $1/2$ is driven.

This transition, however, is not compatible with the polarisation switching scheme for the control light mentioned above, because the signal target light couples to the state $|e_t\rangle$ with the hyperfine quantum numbers $|F, m_F\rangle = |2, -2\rangle$. This stretched state has no component of $m_J = 1/2$, where J, m_J are the fine structure quantum numbers, and σ^- polarised control light cannot couple this state to the $100S_{1/2}$ state. Hence, we choose σ^+ polarised control light during the target pulse. In a copropagating beam geometry, the only choice for $|e_g\rangle$ is thus the state $|F, m_F\rangle = |2, 0\rangle$ which requires the gate signal light to be σ^+ polarised. Consequently, the absorption cross section on the signal transition is a factor of 6 smaller for the gate than for the target pulse. This leads to reduced storage efficiencies for the gate excitation. This, however, can partially be compensated by appropriately adjusting the Rabi frequency of the control field. Also, it is worth mentioning that the storage efficiencies can theoretically

	gate		target	
	measured spectra	theory	measured spectra	theory
EIT peak transmission T_0	0.40		0.18	
EIT linewidth $\Delta\omega_T/2\pi$ (MHz)	3.3	1.7	4.0	4.0
Optical depth OD	3.2	3.5	15	10
Angular matrix el. control [127]	$1/3$		$\sqrt{2}/3$	
Control Rabi frequency $\Omega_c/2\pi$	4.7 MHz		9.4 MHz	
Absorption length l_a	$30\,\mu$m		$5\,\mu$m	
Blockade radius R_b, cf. Eq. (2.48)	$18\,\mu$m		$14\,\mu$m	

Table 5.1.: EIT properties. If possible, they are obtained from measured spectra. For comparison, theoretical estimates are calculated from the parameters of the atomic cloud as in Chap. 4.1. A cloud of $N = 2.2\times10^5$ atoms at a temperature of $T = 0.43\,\mu$K is used for all experiments in this chapter.

be increased by elongating the atomic cloud along the propagation direction of the signal light while keeping the atomic density constant. If the on-resonance EIT transmission is high, this should not affect the switching contrast.

Tab. 5.1 summarises important properties that are associated with the transitions shown in Fig. 5.2(b). The two central requirements for the realisation of a switch are met: Firstly, on the target transition, the absorption length $l_{a,t}$ is small compared to $2R_b$. Secondly, the blockade radius is larger than the waist of the signal beam of $w_s = 8\,\mu$m. During the experiment, a magnetic field of $B \sim 0.2\,$G is applied along the z axis to preserve the spin orientation. The resulting Zeeman splitting between the Rydberg states $|r_g\rangle$ and $|r_t\rangle$ is $\Delta_B/2\pi = g_s\mu_B B/h \approx 0.6\,$MHz, where $g_s \approx 2$ is the Landé factor of the electron and μ_B the Bohr magneton. This is much smaller than the measured EIT linewidths listed in Tab. 5.1.

An important feature of the switch is that we are able to retrieve the gate excitation at the end of the experimental sequence. Therefore long coherence times are necessary. At a peak atomic density of $\sim 2.4\times10^{12}\,\mathrm{cm}^{-3}$, in a storage and retrieval experiment, the number of retrieved gate photons decays with $1/e$ time scale of $\sim 0.9\,\mu$s (cf. Fig. 4.5). As the dephasing is not dominated by the thermal motion, the recoil transfer during storage can be neglected and it is sufficient to apply the signal and control fields in copropagating fashion (cf. Fig. 3.3).

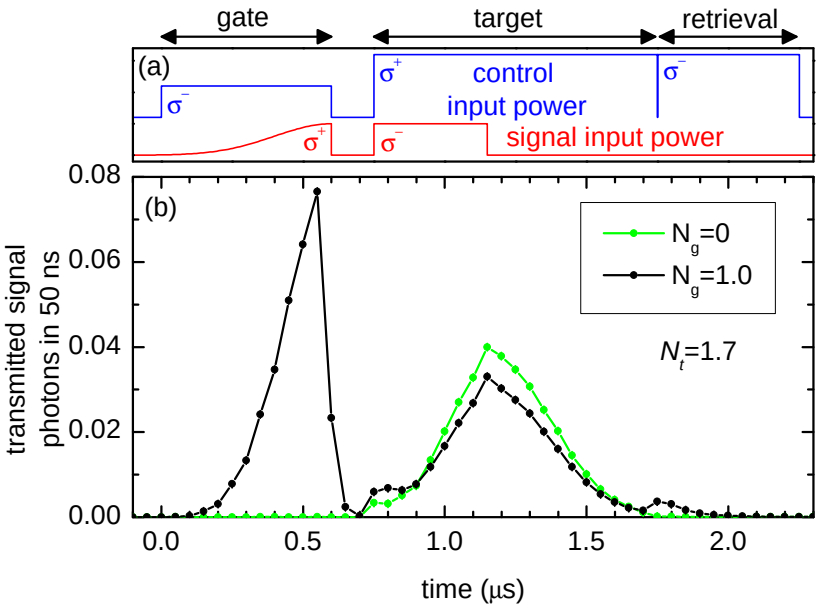

Figure 5.3.: Single-photon switch. (a) Input-power timing sequence reproduced from Fig. 5.2(a) for reference. (b) Experimental results. The black data show the average number of transmitted signal photons for an average number of incoming signal photons during the gate pulse of $N_g = 1.0$. The green data show a reference measurement with $N_g = 0$. The extinction between black and green target-pulse data is $\epsilon = 0.812 \pm 0.001$. The deviation from $\epsilon = 1$ is clearly observed, thus demonstrating a single-photon switch. The average number of incoming target signal photons is $N_t = 1.7$. The subensemble postselected on the detection of a retrieved photon yields $\epsilon = 0.051 \pm 0.004$.

5.3. Experimental Demonstration of a Single-Photon Switch

The experimental results demonstrating the single-photon switch are shown in Fig. 5.3. The gate pulse is derived from a laser and contains $N_g = 1.0$ photons on average. The black data show two large peaks. The first peak is an undesired nonzero transmission during the gate pulse due to imperfect storage. The second large peak shows the number of transmitted target photons which is reduced compared to the green reference data. There are also two smaller peaks in the black data: one at the beginning of the target interval, which can be attributed to undesired partial retrieval of the stored gate excitation, the other at the beginning of the retrieval interval, corresponding to the desired retrieval of the gate excitation.

To quantify how well the gate pulse reduces the transmission of the target

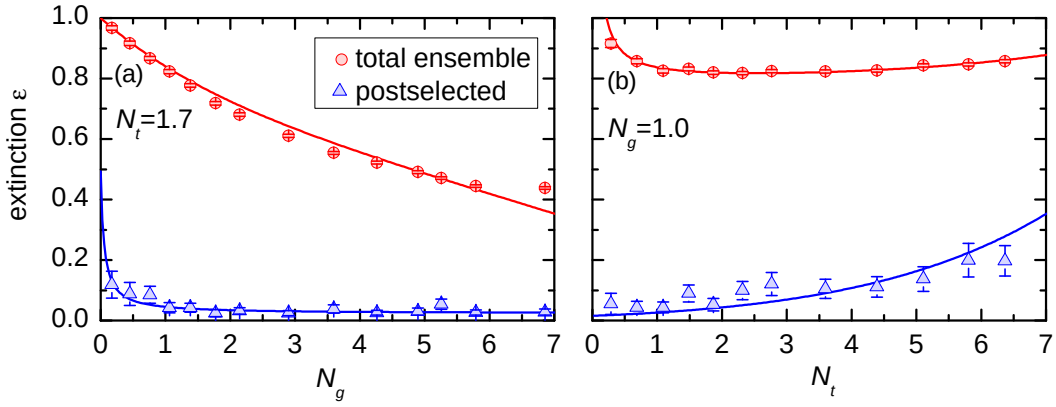

Figure 5.4.: (a) Dependence of the extinction ϵ on the incoming average photon number in the gate pulse N_g. Large N_g reduces the probability of storing zero Rydberg excitations, resulting in improved average extinction in the total ensemble. The subensemble that is postselected conditioned on detecting a retrieved gate excitation shows a drastically improved extinction. This proves that the non-ideal extinction in the total ensemble is dominantly limited by the storage efficiency. (b) Dependence of the extinction ϵ on the incoming average photon number in the target pulse N_t. ϵ is fairly robust against changing N_t. All lines show fits to models from Ref. [103].

signal photons, we use the extinction

$$\epsilon = \frac{N_{t,\text{trans}} \text{ with gate signal pulse}}{N_{t,\text{trans}} \text{ without gate signal pulse}}, \tag{5.1}$$

where $N_{t,\text{trans}}$ denotes the mean number of transmitted target signal photons in one gate-target cycle. A reduction of ϵ below 1 is clearly observed in Fig. 5.3, thus realising an all-optical switch. As the average number of signal photons in the incoming gate pulse N_g is only 1.0, this measurement demonstrates a single photon switch.[1]

As the signal light is derived from an attenuated laser beam, the incoming gate photons have a Poissonian number distribution so that there is a noticeable probability that more than one photon enters the medium. However, the probability of storing more than one photon is negligible due to Rydberg blockade among the gate photons before storage, as discussed in Chap. 4.3.

If the storage of different gate photons is uncorrelated, then the number of excitations stored will be Poissonian too. This is expected for small N_g where blockade among gate photons has little relevance. Hence, the probability of

[1] After the start of the gate-target cycle, a new equilibrium of the atomic density establishes on a time scale that is given by the slowest trap oscillation period. Hence, typically data from the first 50 ms after the start of the gate-target cycle are not processed. After 950 ms, the density has dropped due to particle loss such that a new atomic sample has to be loaded. Every second gate-target cycle is a reference measurement with $N_g = 0$ to minimise systematic errors.

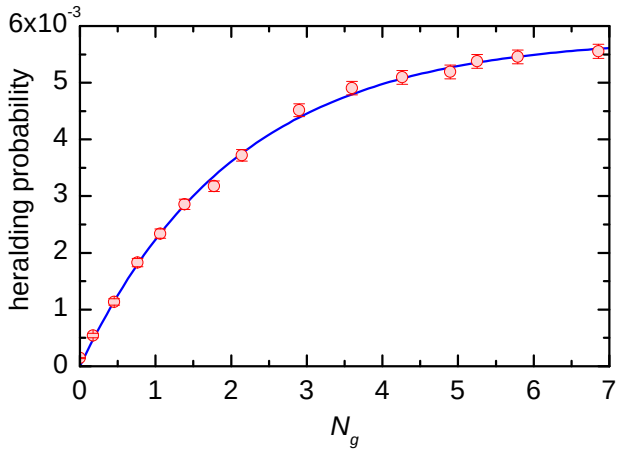

Figure 5.5.: Heralding probability p_h for the data in Fig. 5.4(a). p_h increases linearly for small N_g. The offset at $N_g = 0$ corresponds to the probability of detecting a dark count $p_d = 1.4 \times 10^{-4}$. p_h levels off for large N_g due to Rydberg blockade, similar to the data shown in Fig. 4.2(a). The solid line shows a fit to the model in Ref. [103].

storing zero excitations is $p_{s,0} = \exp(-\beta N_g)$ for small N_g. Here β is the storage efficiency in the absence of Rydberg blockade. Even if suppression of the target transmission by a Rydberg excitation is perfect, $p_{s,0}$ sets a lower boundary on the extinction $p_{s,0} \leq \epsilon$.

A quantitative understanding of how well a single Rydberg excitation suppresses the target transmission can be obtained by postselecting the data on successful retrieval events. The corresponding extinction ϵ does not depend on the storage efficiency β. For the data shown in Fig. 5.3, the postselected subensemble shows a drastically improved extinction of $\epsilon = 0.051 \pm 0.004$. This means that it is mostly limited by the finite probability for creating a gate excitation in the medium.

Fig. 5.4(a) shows how the extinction depends on the number of incoming gate photons N_g. Even for $N_g = 0.17$, we observe a deviation of ϵ from 1 by 4.5 standard errors in the total ensemble. As the gate photons create blockade for each other, the simple estimate above is only applicable for small N_g. Hence, β can be obtained from the absolute value of the slope $\beta = |d\epsilon/dN_g|$ at $N_g \to 0$. A fit to the data yields $\beta = 0.19$.

The postselected subensemble shows a drastically improved extinction. For very small N_g, the postselected extinction deteriorates slightly. This is because, for small N_g, the heralding probability, shown in Fig. 5.5, decreases so that background counts during the retrieval interval contribute an increasing fraction to the heralded events.

One can model the effects of the dark counts during the retrieval interval [103]. A fit of this model to the postselected data in Fig. 5.4(a) shows that the extinction in the absence of these dark counts would be $\epsilon = 0.022 \pm 0.003$. We compare

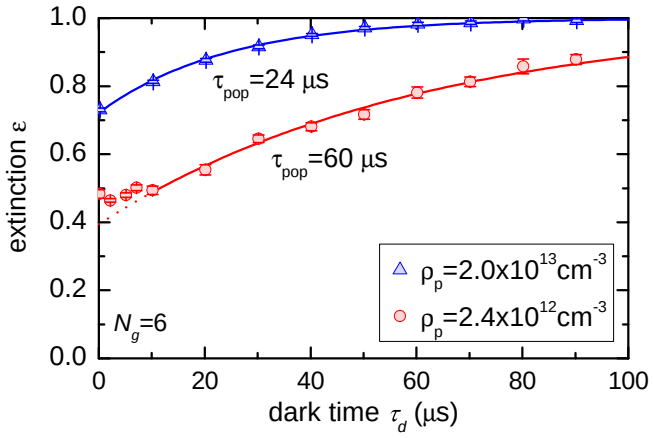

Figure 5.6.: Decay of Rydberg blockade. The extinction ϵ in the total ensemble decays as a function of the dark time τ_d between gate and target pulse. The decay is most likely caused by population decay of the Rydberg atoms. Higher density of surrounding ground-state atoms, characterised by the peak density ϱ_p, causes a faster decay. Exponential fits to the data yield $1/e$ times of $\tau_{\mathrm{pop}} = 24$ and $60\,\mu$s. The blue data serve only to illustrate the density dependence. Normally, we do not operate at such high density.

this value to the rough theoretical estimate of Eq. (2.50). Assuming that the medium is homogeneous with length $2\sigma_z$, we obtain $l_{a,\mathrm{EIT}} \approx -2\sigma_z/\ln T_0 = 28\,\mu$m. Inserting this and the parameters from Tab. 5.1 into Eq. (2.50) yields $\epsilon = 0.013$, which is in fair agreement with the value obtained from the fit.

Fig. 5.4(b) shows the dependence of ϵ on N_t at fixed target pulse duration. The dependence is rather weak, showing that the single-photon switch is fairly robust. The lines show fits to models from Ref. [103]. The slight deterioration of ϵ for larger N_t is due to the fact that scattering target signal photons reduces the atomic density, thus reducing the absorption. But this occurs only when averaging over a large number of cycles for each atomic gas. The deterioration of ϵ for small N_t is due to background photodetection events due to an undesired readout of stored gate photons during the target pulse.

5.4. Lifetime of the Rydberg Blockade

The Rydberg blockade is quite robust. On one hand, Fig. 5.4(b) shows that the extinction ϵ depends only weakly on N_t. On the other hand, Fig. 5.6 shows that it only decays slowly as a function of the dark time τ_d between gate and target pulse. This decay is much slower than the dephasing rate observed in Fig. 4.5. While the decay of retrieval in Fig. 4.5 is sensitive to phase coherence and displays a time scale of $\sim 1\,\mu$s, the decay of blockade in Fig. 5.6 is only sensitive to Rydberg population. An exponential fit (solid line) to the low-density data (red) with $\tau_d \geq 10\,\mu$s yields a 1/e time of $60\,\mu$s. Data for shorter times seem

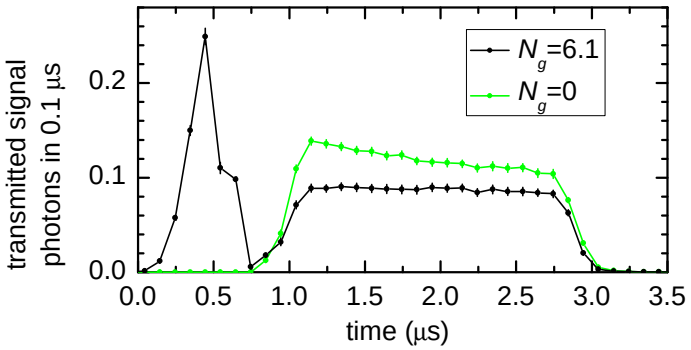

Figure 5.7.: Decay of extinction during the target light pulse. The black data show the average number of transmitted signal photons for an average number of incoming signal photons during the gate pulse of $N_g = 6.1$. The green data show a reference measurement with $N_g = 0$. Note that the target light pulse is longer than in Fig. 5.3. The ratio of the two data sets decays with a $1/e$ time of $2.6 \pm 0.2\,\mu$s.

to deviate slightly from the extrapolated fit curve (dotted line). A model based on spontaneous emission and blackbody radiation predicts a $336\,\mu$s lifetime for the $100S_{1/2}$ state (cf. Tab. 2.1). We obtain a hint at a possible origin of the deviation from the measured decay time of the blockade by comparing this decay time with a measurement at 8 times higher atomic density (blue data), where the population lifetime is only $24\,\mu$s. This suggests that the collisions of a Rydberg atom with ground-state atoms are responsible for the decay.[2] Possible processes include associative ionisation [153] or ion pair formation [154]. Related observations were reported in Ref. [151].

5.5. Decay of Extinction

We not only observe a decay of extinction during the dark time between gate and target pulse but also during the target pulse itself. This decay takes place on a much faster time scale than the one observed in Fig. 5.6. The decay becomes apparent if we increase the duration of the target signal light pulse to $2\,\mu$s. Accordingly, the target control pulse is extended to $2.5\,\mu$s. Fig. 5.7 shows an exemplary data set that exhibits the decay of extinction during the target pulse.[3] The green data show a reference measurement with $N_g = 0$ and $N_t = 6.1$. It is evident that the transmitted target photon rate decays. Note that the incoming signal light pulse is rectangular. The origin of this decay is currently unclear. A possible reason could be undesired storage of target signal

[2] This hypothesis is supported by the data in Chap. 6, where a lifetime of the Rydberg state $69S_{1/2}$ is measured that is close to the theoretical predictions.

[3] These data were recorded at a peak atomic density of $\varrho_p = 2.0 \times 10^{-13}\,\mathrm{cm}^{-3}$ and a temperature of $\sim 0.26\mu$K.

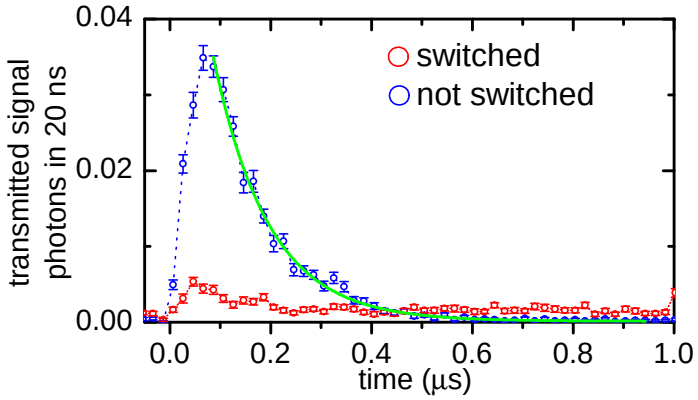

Figure 5.8.: Suppression of undesired retrieval during the target pulse. Only the target interval is shown (cf. Fig. 5.3) and no target signal light is applied. The number of incoming gate photons is $N_g = 0.9$ on average. If the polarisation of the control light is not switched (blue), then the signal gate light is retrieved with a $1/e$ time of $0.110(3)\mu$s. Switching the control polarisation from σ^- to σ^+ suppresses the amplitude of the retrieval signal.

light due to dephasing.

The black data show the transmitted signal photons for $N_g = 6.1$. The first pulse is light leaking through the cloud due to imperfect storage. The second pulse is the transmitted signal target light. We divide these data by the reference data and obtain a $1/e$ time of $2.6 \pm 0.2\,\mu$s from an exponential fit that is assumed to decay to 1.[4] Because of the decay of the extinction, the duration of the target light pulse that is useful for switching is limited to a few microseconds.

One contribution to the decay of the extinction comes from the undesired retrieval of the gate excitation by the target control light. This undesired retrieval is largely suppressed by the switching of control light polarisation from σ^- for the gate pulse to σ^+ for the target pulse (cf. Chap. 5.2). To quantify this suppression, we repeat the experiment of Chap. 5.3, without signal target light applied. Fig. 5.8 shows the signal light that is retrieved while the target control light is applied.

For reference, we first study the case where the polarisation of the control light remains at σ^- (blue data). Here, we observe a quick rise of the retrieved signal light followed by a decay with a $1/e$ time of $\tau_{\mathrm{retr}} = 0.110(3)\,\mu$s. If, instead, the polarisation is switched to σ^+ (red data), then the retrieved signal displays much less amplitude and a much slower decay. The amplitude is so small and the decay so slow that the signal-to-noise ratio of the data does not suffice for extracting the $1/e$ time.

To obtain a coarse estimate for this $1/e$ time, nonetheless, we note that the ratio of the amplitudes of the red and blue data is $\sim$1:7.[5] A simple model suggest

[4] Varying N_t between 1.5 and 32, we observe $1/e$ times between $\sim 4.7\,\mu$s and $\sim 1.3\,\mu$s.

[5] It is unclear why this ratio is not better. A measurement of the purity of the linear

that the rate at which signal photons are retrieved is $(\eta_c/\tau_{\mathrm{retr}})\exp(-t/\tau_{\mathrm{retr}})$, where η_c is a constant that incorporates the photon collection efficiency and the initial population of the Rydberg state. Hence, we can estimate the $1/e$ time for the blue data to be ~ 7 times that of the red data, yielding the coarse estimate $\tau_{retr} =\sim 0.8\,\mu$s.

This estimate is somewhat shorter than the $1/e$ time observed in Fig. 5.8. On one hand, this suggests that the estimate is not very accurate because one would expect the $1/e$ time in Fig. 5.7 to be shorter than this estimate; on the other hand, it suggests that undesired retrieval actually contributes significantly to the decay of extinction observed in Fig. 5.7. At this point, it might be tempting to take additional data to rigorously pin down the origin of the problem. Instead, we decided to eliminate undesired retrieval as described in Chap. 6.1 instead of studying the origin of the problem in detail.

polarisations immediately after the EOM yields an intensity ratio of 1:100. Assuming that the wave vector of the signal light is parallel to the magnetic field and that the wave plates are rotated correctly, one would expect that the ratio of the retrieved amplitudes should match the intensity ratio after the EOM.

6. A Single-Photon Transistor using a Förster resonance

This chapter reports the realisation of a single-photon transistor that exhibits a gain of 20. The majority of the experimental results has been published in Ref. [104]. The single-photon transistor builds on the experiments presented in Chap. 5 and is a much improved version thereof. Chap. 6.1 discusses the conceptual advances that lead to the observation of gain. In Chap. 6.2 the new atomic level scheme and the experimental sequence are described. In the subsequent Chap. 6.3, the experimental data showing a single-photon transistor with gain are presented. A major advancement compared to previous experiments is that a Förster resonance is utilised in order to achieve strong Rydberg blockade at fairly low principal quantum numbers. Experimental evidence for the benefits of the Förster resonance are given in Chap. 6.4. In Chap. 6.5, the non-destructive optical detection of a Rydberg excitation in a single experimental shot is demonstrated as a first application of the transistor.

6.1. Conceptual Advances

One of the main limitations of the single-photon switch of Chap. 5 is that is does not show a gain above unity. The gain is defined as

$$G = \frac{\Delta N_{\mathrm{trans}}}{N_g} = \frac{|N_{\mathrm{trans,\ ref}} - N_{\mathrm{trans}}|}{N_g}, \tag{6.1}$$

where N_{trans} is the number of transmitted target photons and $N_{\mathrm{trans,ref}}$ is the reference value for $N_g = 0$. The single-photon switch of Chap. 5 exhibits a gain of ~ 0.24.

There are various strategies that could solve this problem in principle. Some obvious candidates are increasing the duration of the target pulse, increasing the input intensity of the target pulse, increasing the EIT transmission by reducing dephasing, and improving the storage efficiency.

Increasing the duration of the target pulse does not yield much higher gain in Chap. 5, because the extinction decays on a time scale of a few microseconds, a problem which, as suggested by Chap. 5.5, has a significant contribution from undesired retrieval. To overcome this problem, we decided to base the suppression of undesired retrieval on using different principal quantum numbers n_g and

n_t for the gate and target pulse, respectively. Hence, the frequencies of the control light pulses differ by many gigahertz so that the target control light cannot induce a noticeable amount of undesired retrieval.

As high-efficiency frequency shifters for these frequencies are not available, this means that the control light fields must be produced in two different lasers, namely the two 475 nm lasers described in Chap. 3.2. This strategy has the drawback that setting up the second laser, its beam path, and its frequency stabilisation represent a considerable amount of additional effort compared to the measurements in Chap. 5 which use only one control laser. Once, this effort is expended, however, this scheme offers significant additional advantages at very little additional experimental effort.

Having two lasers available, we can utilise the Förster resonance for $n_t = n_g - 2 \sim 70$ discussed in Chap. 2.2.5. This leaves the blockade radius between a stored gate excitation and a propagating target excitation essentially the same as in Chap. 5. At the same time, it reduces self-blockade[1] within the target pulse because the blockade radius between two propagating target excitations is much reduced. This increases the gain.

Another benefit of using the Förster resonance is the use of lower principal quantum numbers which reduces dephasing, as discussed in Chap. 4.4. This increases the transmission on the EIT resonance which, in turn, increases the gain. In addition, the decay of the green data in Fig. 5.7 might be explained as undesired storage caused by dephasing. Hence, a reduction in dephasing might be expected to reduce this decay. Indeed, this expectation agrees with our observations in Chap. 6.3. This also increases the gain.

We find that the combination of all these improvements leads to a $1/e$ time for the decay of the extinction of $\sim 100\,\mu$s compared to only a few microseconds in Chap 5.5. Hence, increasing the target pulse duration now does increase the gain far above unity.

The improved scheme offers even more benefits. The reduced dephasing also increases the storage efficiency which improves the extinction and the gain. Using different principal quantum numbers makes it possible to choose the same polarisation for both, the gate and the target signal light pulse. This increases the electric-dipole matrix element for the gate signal transition, which increases the storage efficiency and thus the gain. The reduced principal quantum numbers also increase the radial part of the electric-dipole matrix elements for both control transitions by a factor of ~ 1.7 according to Eq. (2.25), correspondingly reducing the laser powers required to achieve the same Rabi frequencies.

[1] Increasing the input power of the target signal pulse is still not very useful because of the self-blockade, but the transmitted intensity at similar input power is increased.

6.2. Experimental Sequence

Fig. 6.1(a) shows the atomic level scheme that is used for the single-photon transistor. The signal light is σ^- polarised for both the gate and the target pulse and therefore drives the strongest available transition on the D_1 line with branching ratio 1/2. The σ^+ polarised control light couples to Rydberg states with principal quantum number n_g and $n_t = n_g - 2$ for the gate and the target control light, respectively. The angular matrix element for these transitions is $\sqrt{2}/3$ [127].

The two control light beams originate from two different lasers. The gate control beam counterpropagates the signal beam (cf. Fig. 3.3) and is derived from the ECDL-TA-SHG laser system. The target control beam copropagates with the signal beam and originates from the Ti:Sa-SHG laser system. The gate and target control light have powers of $P_{c,g} = 17\,\mathrm{mW}$ and $P_{c,t} = 10\,\mathrm{mW}$, respectively.

The timing sequence is similar to the one in Chap. 5.2 and is depicted in Fig. 6.1(b). The main difference is that the target signal light pulse has a duration of $200\,\mu\mathrm{s}$. The gate-target pulse sequence is repeated with a cycle repetition time of $t_{\mathrm{cyc}} = 1\,\mathrm{ms}$. After ~ 500 gate-target cycles, a new atomic sample is prepared.[2]

For the experimental realisation of the single-photon transistor, an ultracold cloud of 1.5×10^5 atoms at a temperature of $T = 0.33\,\mu\mathrm{K}$ is used. A magnetic field of 1.1 G is applied along the z direction. An EIT spectrum, measured for characterisation purposes on the target transition, is shown in Fig. 4.1 and discussed in Chap. 4.1 in detail. The key features are a peak transmission of $T_0 = 0.67$, a linewidth of $\Delta\omega_T/2\pi = 1.8\,\mathrm{MHz}$, and an optical depth of $OD = 5$. For the gate transition, the maximal transmission $T_0 = 0.56$ is slightly smaller at a similar linewidth. Based on these data we can estimate the blockade radii. For the $|69S_{1/2}, 67S_{1/2}, M = 1\rangle$ state, a van der Waals coefficient of $C_6 = 2.3 \times 10^{23}\,\mathrm{a.u.}$ can be calculated using Eq. (2.42).[3] This yields a blockade radius of $R_b = 16\,\mu\mathrm{m}$ according to Eq. (2.49). This value is similar to the blockade radius for the target light in Chap. 5. For comparison, the state $|67S_{1/2}, 67S_{1/2}\rangle$ has a much smaller C_6 of $-3.6 \times 10^{21}\,\mathrm{a.u.}$, which yields $R_b = 8\,\mu\mathrm{m}$. Based on the properties of the atomic cloud, the absorption length for the target light is estimated to be $l_{a,t} = 10\,\mu\mathrm{m}$.[4]

[2] Like in Chap. 5, we discard the first 50 ms after starting the gate-target cycles. However, we typically only process the subsequent 100 ms because the atom number drops faster than in Chap. 5.

[3] Only the coupling to the pair state $|68P_{1/2}, 67P_{3/2}\rangle$ is considered. R_b is so large, that the van der Waals approximation is correct within 10%. Details can be found in Chap. 2.2.5, in particular in Fig. 2.7.

[4] The time-averaged repulsive potential created by the control light is $\langle V_{c,0}\rangle = k_B \times 0.16\,\mu\mathrm{K}$ and therefore cannot be neglected (cf. Chap. 3.1). Taking the potential into account, we obtain an atomic density at the centre of the trap of $\varrho_0 = 1.3 \times 10^{12}\,\mathrm{cm}^{-3}$. Approximating the medium as homogeneous with density $\varrho_0/2$ yields the absorption length quoted in the

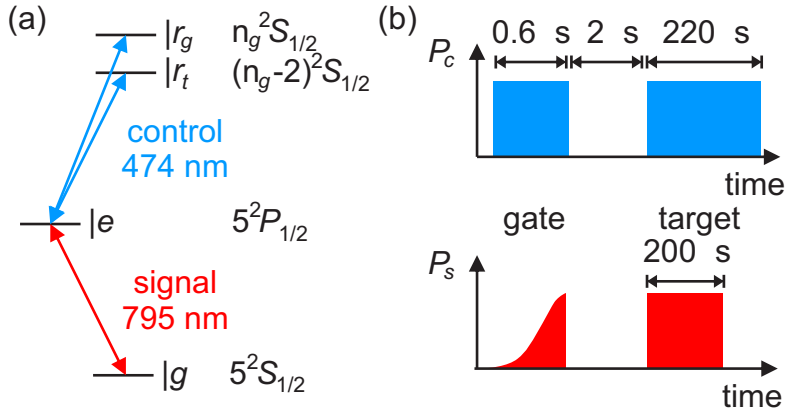

Figure 6.1.: (a) Level scheme for the single-photon transistor. Gate and target pulse each consist of signal light and control light for EIT. Both pulses use the same signal transition, but the control light operates at different frequencies, thus reaching different Rydberg states $|r_g\rangle$ and $|r_t\rangle$. The hyperfine quantum numbers are $F = 1, m_F = -1$ and $F = 2, m_F = -2$ for states $|g\rangle$ and $|e\rangle$, respectively, whereas both Rydberg states have $m_J = 1/2$ and $m_I = -3/2$. The fact that the principal quantum numbers n_g and $n_t = n_g - 2$ differ suppresses undesired retrieval of stored gate excitations by target control light much more efficiently than the polarisation scheme of Chap. 5.2. In addition, both signal light pulses profit from a large electric-dipole matrix element. We typically operate at $n_g = 69$. (b) Input power timing scheme not to scale (see text).

6.3. A Single-Photon Transistor with Gain

Fig. 6.2 shows experimental results demonstrating a single-photon transistor with gain. The number of transmitted target signal photons is shown for $N_g = 1.0$ incoming gate signal photons (red circles). The area under the curve reveals the number of transmitted target signal photons N_{trans}. A measurement with $N_g = 0$ (green triangles) yields a corresponding reference value of $N_{\text{trans, ref}} = 171(2)$. The gain as defined in Eq. (6.1) is observed to be $G = 20(1)$ at $N_g = 1.0$. This is far above unity, thus clearly demonstrating the realisation of a single-photon transistor.[5]

For long target pulse duration, the transmitted target photon number approaches the reference, as seen in Fig. 6.2. We divide the data by the reference, and obtain a $1/e$ time of $\tau = 0.10(1)$ ms from an exponential fit. This is not far from the excited-state lifetime, due to radiative decay at room temperature, of

text.

[5] The gain sets an upper bound on the number of identically constructed transistors that can, in principle, be driven. For cascading the transistor, however, achieving better extinction would be desirable.

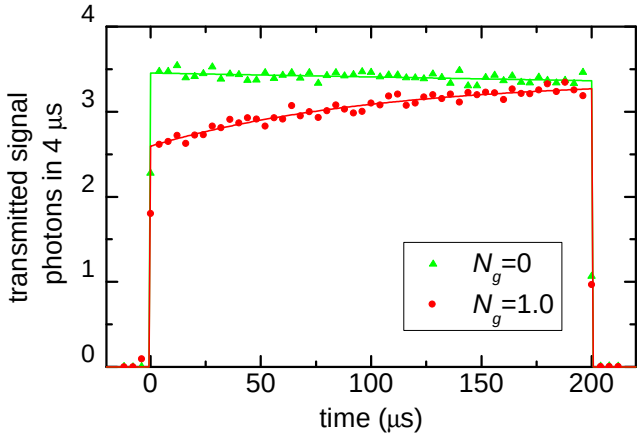

Figure 6.2.: Single-photon transistor. The number of transmitted signal photons is shown for $N_g = 1.0$ incoming signal gate photons (red circles). For reference, the same number is shown in the absence of target signal light $N_g = 0$ (green triangles). The lines show exponential fits multiplied by a step function. The ratio of the areas under the two data sets yields an extinction of $\epsilon = 0.89(1)$. For short target pulse duration the extinction is $\epsilon = 0.75(1)$. The gain is $G = 20(1)$. This is far above unity, thus demonstrating a single-photon transistor.

0.14 ms [143], showing that undesired retrieval of gate excitations and inelastic collisions only have a small effect. As a consequence of the decay, increasing the duration of the target pulse does not lead to a considerably higher gain.

The transmission of the reference target pulse is $T_0 = 0.49(1)$ on EIT resonance for an incoming target photon number of $N_{t,\mathrm{in}} = 350$. This improvement in T_0 by a factor of $\sim$2.5 with respect to Chap. 5 is mostly due to the lower principal quantum number, which reduces self blockade[6] and dephasing. Experimentally varying n_g in the range between 60 and 75, we find that T_0 depends approximately linearly on n_g with a slope of $\Delta T_0/\Delta n_g \sim -0.01$. Increasing the number of incoming target photons does not result in a higher gain, as self-blockade leads to a saturation of the transmitted target photon number.[7]

6.4. Observation of a Förster Resonance

The performance of the single-photon transistor benefits from the Förster resonance near $n_g = 70$, which is discussed in Chap. 2.2.5. The extinction and gain

[6] Evaluation of a $g^{(2)}$ correlation function yields $g^{(2)}(0) = 0.62(2)$ compared to $g^{(2)}(0) = 0.17(1)$ for the $|100S_{1/2}\rangle$ state in Fig. 4.2(b).

[7] In the present experiment, the C_6 coefficient that is relevant for the van der Waals interaction of two target polaritons is a factor of ~ 60 smaller than for the interaction between the a target polariton and a gate excitation. By using a different atomic level scheme, it might be possible to increase this factor thus further reducing self blockade.

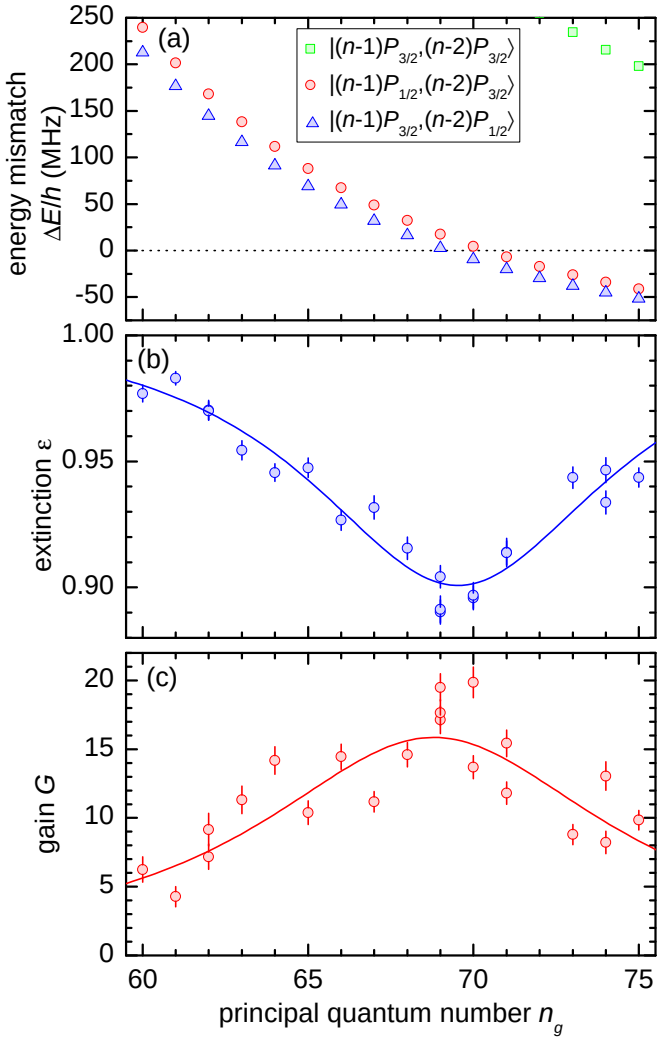

Figure 6.3.: Effect of the Förster resonance on the single-photon transistor. (a) Theoretical estimates of the energy mismatch ΔE in Rb at infinite interatomic distance (cf. Fig. 2.5(b)). The measured values of the extinction (b) and the gain (c) clearly profit from the Förster resonance. The target pulse is operated at $n_t = n_g - 2$. The lines show Lorentzian fits to guide the eye.

in parts (b) and (c) of Fig. 6.3 both show a clear resonance. The positions of the resonances coincide with the zero-crossings of the calculated pair state energy defects which are shown in part (a) for comparison.

The results in Fig. 6.3 constitute a rather unconventional method of detecting a Förster resonance. Compared to the standard approach in cold atom experiments found in the literature, it does not rely on field ionisation [82, 155–157]. The observed dependence of the extinction on the principal quantum number is mainly due to a change in blockade radius. Since the blockade radius is proportional to $C_6^{1/6}$, the resonance is fairly broad. The enhancement of the blockade

radius in the vicinity of the Förster resonance is therefore very robust. It should be noted that the extinction relates to the blockade radius in a non-trivial way. According to the simple one-dimensional model (2.50), the measurement loses its sensitivity to R_b for large $2R_b/l_{a,t}$ because the slope $d\epsilon/dR_b$ decreases. This leads to a further broadening of the resonance. On the other hand, the blockade radius in Fig. 6.3 varies roughly by a factor of two. This means that the condition $R_b \ll w_c$ for perfect transverse blockade is not fulfilled for all n_g. This reduces the extinction far away from the resonance. In addition, it should be noted that close to the Förster resonance state mixing is not negligible and can also affect the blockade.

6.5. Nondestructive Detection of a Rydberg Excitation

Because of the gain, storing a gate excitation has a drastic effect on the transmitted light. This holds not only for the mean value N_{trans} of the transmitted photon number but also for its probability distribution. We measure the histogram for the number of detector clicks N_c registered during a 30 μs long target signal pulse.[8]

Figure 6.4 shows this histogram. The data for $N_g = 1.0$ show a bimodal structure with a clearly visible minimum between the peaks. Clearly, the peak near $N_c = 8$ detector clicks is expected to be identical to the reference distribution with $N_g = 0$, but with the total number of events reduced by an overall factor p_0, which is the probability that zero Rydberg excitations are stored during the gate pulse. A fit (red dotted line) yields $p_0 = 0.60$. Subtracting this fit from the data for $N_g = 1.0$ yields the black solid line.

The red dotted line and the black solid line have well-separated peaks. Hence, the value of N_c obtained in a single experimental shot reveals whether the number of Rydberg excitations N_{Ryd} stored during the gate pulse was zero or nonzero. We set a threshold N_{thr} and assign $N_{\mathrm{Ryd}} = 0$ if $N_c > N_{\mathrm{thr}}$ and $N_{\mathrm{Ryd}} \neq 0$ otherwise. Let c_0 and c_1 denote the probability that this assignment is correct if the initial state were ideally prepared with $N_{\mathrm{Ryd}} = 0$ and $N_{\mathrm{Ryd}} \neq 0$, respectively. To define the fidelity for estimating whether a Rydberg excitation was stored, we follow the conservative definition of Ref. [158] that the fidelity F is the minimum of c_0 and c_1. From Fig. 6.4 we find that the choice $N_{\mathrm{thr}} = 5.5$ maximises the fidelity, yielding $F = 0.86$. Note that the results for p_0 and F depend on the choice of the cutoff value N_{cut} of N_c for fitting p_0. In particular,

[8] These data are recorded with $N \sim 2.4 \times 10^5$, $T = 0.27$ μK, $(P_{c,g}, P_{c,t}) = (35, 22)$ mW, a dark time of 0.15 μs between gate and target pulse, a target control pulse duration of 100 μs, and $t_{\mathrm{cyc}} = 0.7$ ms. The maximal EIT transmission is $T_0 = 0.62$. The repulsive potential created by the control light is $\langle V_{c,0} \rangle = k_B \times 0.51\,\mu$K resulting in an atomic density in the centre of the trap of $\varrho_0 = 8.5 \times 10^{11}\,\mathrm{cm}^{-3}$. This yields a target absorption length of $l_{a,t} = 15.5\,\mu$m.

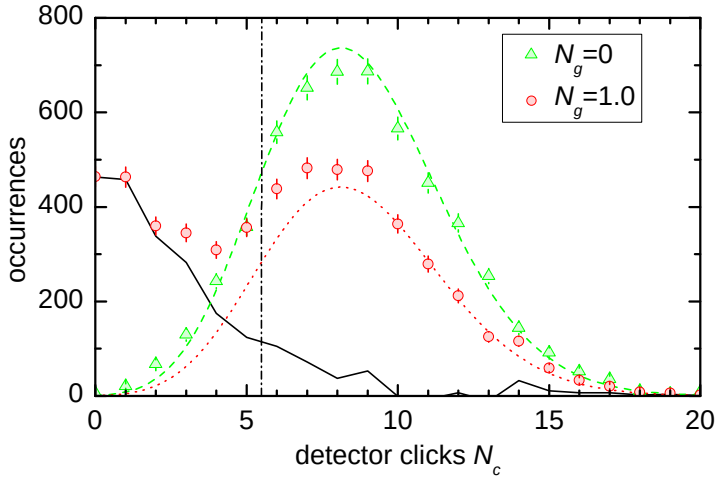

Figure 6.4.: Bimodal distribution. The histogram for the number of detector clicks N_c during the target pulse is shown. The reference pulse with $N_g = 0$ (green triangles) has mean value $\langle N_c \rangle_{\mathrm{ref}} = 8.62(4)$ and variance 9.87. It is well approximated by the Poisson distribution with this mean value (green dashed line). The distribution for $N_g = 1.0$ (red circles) is bimodal. Its peak near $N_c = 8$ is caused by events in which zero gate excitations were stored. This peak is identical to the green line except for an overall factor p_0, expressing the probability for storing zero excitations. A fit (red dotted line) to the data with $N_c > 9.5$ yields the best-fit value $p_0 = 0.60$. The black solid line shows the difference between the red data and the red fit curve. It represents the histogram if a Rydberg excitation was stored. From the value of N_c measured in a single shot, one can infer whether a Rydberg excitation was stored. Setting the discrimination threshold to $N_{\mathrm{thr}} = 5.5$ (dash-dotted vertical line) yields a fidelity for this inference of $F = 0.86$ (see text).

for $N_{\mathrm{cut}} \ll 9.5$ the black solid curve contributes noticeably to the red data, causing the fit to overestimate p_0 and F, whereas for $N_{\mathrm{cut}} \gg 9.5$ the fit must infer the peak height only from data far out on the wings of the distribution which is prone to produce incorrect results. A detailed analysis shows that fits with $7.5 \leq N_{\mathrm{cut}} \leq 12.5$ produce reliable values, with p_0 varying between 0.60 and 0.64 and with F between 0.86 and 0.88. $F = 0.86$ can therefore be regarded as a conservative estimate with respect to the choice of N_{cut}.

The value of p_0 determined here can be used to estimate the storage efficiency $\eta_s = N_s/N_g$, where N_s is the number of stored excitations. On the one hand, the solid bound $\eta_s \geq 1 - p_0$ is reached if the probability of storing more than one excitation is neglected. Using $p_0 = 0.64$, we obtain $0.36 \leq \eta_s$. On the other hand, as self blockade of the gate pulse is not very pronounced, one could approximate the number of stored excitations as Poissonian, so that $p_0 = \exp(-N_s)$ and $p_0 = 0.60$ would yield the less conservative estimate $\eta_s \sim 0.51$. It is obvious that improved storage efficiencies would lead to a higher gain and an improved

extinction.

The histograms, shown in Fig. 6.4, can also be used to estimate the extinction if a gate excitation is present. To this end, the average transmitted photon numbers for the black and green curve in Fig. 6.4 are calculated. Subsequent division yields an extinction of $\epsilon = 0.25$. We compare this to the rough estimate from Eq. (2.50). With a absorption length of $l_{a,t} = 15.5\,\mu$m calculated from the cloud parameters and the EIT absorption length $l_{a,\mathrm{EIT}} = -2\sigma_z/\ln T_0 = 90\,\mu$m, we obtain $\epsilon \sim 0.17$ for a blockade radius of $R_b = 16\,\mu$m. The agreement is fair considering the approximations made. This suggests that higher gain and better fidelities can be attained by reducing $l_{a,t}$. This could be achieved by reducing the duty cycle of the experiment which leads to higher atomic densities in the centre of the trap. Alternatively, an atomic transition with larger electric dipole moment could be used for the signal light such as the cycling transition of the D_2 line in ^{87}Rb. This should reduce the absorption length by a factor of two compared to the transition currently used.

Repeated detection of a Rydberg excitation As the measurement is nondestructive, it is repeatable within the same experimental shot. It is therefore natural to study how much the assignments of two consecutive measurements correlate with each other. To this end, we analysed the first $66\,\mu$s of the transmitted target signal light of the data set that is shown in Fig. 6.2. We mathematically split the $66\,\mu$s time interval in the data analysis into two parts of equal duration. We assign $R_i = 0$ ($R_i = 1$) Rydberg excitations if the number N_d of detector clicks in time interval $i \in \{1, 2\}$ is above (below) the threshold N_{cut}. We use the Pearson correlation coefficient

$$\rho_{R_1,R_2} = \frac{\mathrm{cov}(R_1, R_2)}{\sqrt{\mathrm{cov}(R_1, R_1)\,\mathrm{cov}(R_2, R_2)}} \tag{6.2}$$

to quantify the correlations between the two measurements [159]. Here, $\mathrm{cov}(X, Y) = \langle XY\rangle - \langle X\rangle\langle Y\rangle$ denotes the covariance. $\rho_{R_1,R_2} = 1$ indicates perfect correlation, whereas $\rho_{R_1,R_2} = 0$ indicates uncorrelated variables.

Our experiment with $N_g = 1.0$ yields $\rho_{R_1,R_2} = 0.45(1)$. Ideally, this should be 1. For reference, we also study the $N_g = 0$ case and obtain $\rho^{\mathrm{ref}}_{R_1,R_2} = 0.07(2)$. This nonzero value indicates that there is a background of correlations, but obviously it is small. For comparison, we find fidelities $F_1 = 0.87$ ($F_2 = 0.80$) along with $p_0 = 0.72$ ($p_0 = 0.77$) for the first (second) $33\,\mu$s, both at $N_{\mathrm{cut}} = 3.5$

To develop a theoretical expectation for ρ_{R_1,R_2}, we write X (or $\bar{X}$) if there is actually a Rydberg excitation present (or absent). As $F_1 \approx F_2$, we approximate $P(R_i = 1|X) = c_1$ and $P(R_i = 0|\bar{X}) = c_0$ to be independent of $i \in \{1, 2\}$. Furthermore, we assume that the following conditional probability factorises $P((R_1 = 1 \cap R_2 = 1)|X) \approx P(R_1 = 1|X)P(R_2 = 1|X) = c_1^2$. We use the same approximation for similar expressions. Hence, the model neglects the decay of the Rydberg excitation. Moreover, as N_{cut} is chosen to maximise

$F = \min(c_0, c_1)$, we find $c_0 \approx c_1 \approx F$ and obtain the prediction

$$\rho_{R_1,R_2} = (2F-1)^2 \ \frac{p_0(1-p_0)}{Y(1-Y)}, \qquad Y = p_0(1-F) + F(1-p_0). \tag{6.3}$$

Using the values of F and p_0 from the first (second) interval yields the prediction $\rho_{R_1,R_2} = 0.48$ ($\rho_{R_1,R_2} = 0.28$). Hence, the above result agrees pretty well with the expectation of this simple model.

The measured value of ρ_{R_1,R_2} is further away from unity than the value of F. The reason for this is firstly that F and ρ_{R_1,R_2} incorporate the errors from one and two measurements, respectively, and secondly that $F = 1/2$ and $\rho_{R_1,R_2} = 0$ define the limits where nothing is learnt from a measurement.

7. Outlook

The realisation of a single-photon transistor brings various applications into reach. The first application has already been demonstrated in this thesis. It is the nondestructive detection of a Rydberg excitation.

This method could be used to monitor the spatial and temporal dynamics of a single Rydberg excitation [160–162]. A recent experiment demonstrated nondestructive imaging capabilities for Rydberg atoms, but was unable to reach sufficient sensitivity to detect a single excitation in a single experimental shot [163]. Single-shot data acquisition capabilities of single excitations offer the possibility to record full probability distributions and correlation functions. Moreover real-time trajectories from single excitations could be recorded.

The detection method is also of practical relevance for quantum memories [164], where it could be used to herald the successful storage of a photon in the memory. After a storage event is heralded, the Rydberg excitation could be transferred into a long-lived ground state.

Furthermore, the single-photon transistor could be used for the detection of an optical photon with high sensitivity. Therefore, higher storage efficiencies would be necessary. The best storage and retrieval efficiencies that have been reported for EIT with atomic ground states are $\eta_{sr} = 0.78$ [165].[1] If the stored photon were retrieved with high efficiency, then this would constitute a nondestructive detection of a single photon [166].

The single-photon transistor could also be used to create coherent superpositions of quantum states with macroscopically different photon number, which are also called *cat states* [167]. To this end, the single-photon transistor could be placed inside an optical resonator that is resonant with the signal light. If the atomic ensemble is transparent, then the signal light will be transmitted, whereas the absorption inside the atomic gas will lead to reflection from the first mirror. This would convert the transmission-absorption switch into a transmission-reflection switch which could operate at low dissipation and decoherence. First steps into this direction are reported in Ref. [168].

In addition to these applications, the single-photon transistor is a first step on the way to realising deterministic quantum logic gates for photons based on Rydberg blockade [90–92, 169]. In most proposals, the prerequisite for the implementation of quantum gates is that a single gate photon would have to switch the phase of a target photon . Such a phase switch could then be extended to a full quantum gate.

[1] The storage efficiency might actually be higher as the finite retrieval efficiency is included.

A. Dephasing in Storage and Retrieval Experiments

In this appendix, we study the influence of dephasing on the retrieval efficiency in storage and retrieval experiments. Two mechanisms are separately analysed. First, we consider the effects of thermal motion. Thereafter, we investigate the consequences of a density-dependent energy shift of the Rydberg state due to collisions with ground state atoms as observed in Chap. 4.4.

We consider a gas of N atoms all of which are initially in the internal state $|g\rangle$. In addition, the j-th atom is in the spatial wave function $u_j(\boldsymbol{x}_j)$. We write the initial state as[1]

$$|g_1, ..., g_N\rangle = \prod_j u_j(\boldsymbol{x}_j)|g_j\rangle. \tag{A.1}$$

Assuming one incoming signal photon and perfect storage efficiency, the EIT storage process creates the Dicke state $|D(0)\rangle = |D^1_{N-1}\rangle$ of Eq. (2.12).

During the dark time τ_d in storage and retrieval experiments the Dicke state $|D(\tau_d)\rangle$ evolves in time. We simplify the description of the retrieval process by assuming that the control laser only couples to the state $|D(0)\rangle$ and that all population in $|D(0)\rangle$ is converted into light during the retrieval. This population is $|\langle D(0)|D(\tau_d)\rangle|^2$ so that the storage and retrieval efficiency is

$$\eta_{sr} = |\langle D(0)|D(\tau_d)\rangle|^2 . \tag{A.2}$$

Thermal atomic motion. We now study the time evolution of the Dicke state $|D(\tau_d)\rangle$ due to the recoil transferred during storage. During the dark time τ_d, each term in the sum in $|D\rangle$ picks up a phase factor $\exp(-iE\tau_d/\hbar)$ with the energy E. We choose the energy such that the internal state with exactly one excitation has zero energy. Only the kinetic energy remains. Furthermore, we assume that the j-th atom is in a plane wave state with $u_j(\boldsymbol{x}_j) = \exp(i\boldsymbol{k}_j\boldsymbol{x}_j)/\sqrt{V}$, where V is the quantisation volume and $\boldsymbol{k}_j$ the initial momentum of the j-th atom. After the dark time τ_d the state has evolved to

$$|D(\tau_d)\rangle = \exp\left(-i\tau_d\frac{\hbar}{2m}(\Delta k^2 + \textstyle\sum_l k_l^2)\right)\frac{1}{\sqrt{N}}\displaystyle\sum_{i=1}^{N} e^{i\Delta\boldsymbol{k}(\boldsymbol{x}_j - \boldsymbol{v}_j\tau_d)}|g_1, ..., r_j, ..., g_N\rangle, \tag{A.3}$$

[1] The right hand side is a mixed representation, where the spatial part is taken in a position representation, whereas the internal part is representation free. The left hand side is only a symbolic abbreviation.

where $\boldsymbol{v}_j = \hbar \boldsymbol{k}_j / m$. $|g_1, ..., r_j, ..., g_N\rangle$ is the same state as in Eq. (A.1) except that the internal state of the j-th atom is $|r\rangle$. Inserting this into Eq. (A.2) yields for the retrieval efficiency

$$\eta_{sr} = \left| \frac{1}{N} \sum_j \exp(-i \boldsymbol{v}_{\mathrm{rec}} \boldsymbol{k}_j \tau_d) \right|^2 = \frac{1}{N^2} \left(N + \sum_{j,l,j \neq l} \exp(i \boldsymbol{v}_{\mathrm{rec}} (\boldsymbol{k}_j - \boldsymbol{k}_l) \tau_d) \right), \tag{A.4}$$

where $\boldsymbol{v}_{\mathrm{rec}} = \hbar \Delta \boldsymbol{k} / m$.

We now consider a thermal Boltzmann distribution for the wave vectors of the initial state. Hence, the wave vectors of different atoms are uncorrelated and the single-particle distribution is given by Gaussian with rms width $\sigma_k = \sqrt{m k_B T}/\hbar$. From Eq. (A.4) we obtain

$$\eta_{sr} = \frac{1}{N} + \frac{N-1}{N} \exp\left(-(\sigma_k v_{\mathrm{rec}} \tau_d)^2\right) \approx \exp\left(-(\sigma_k v_{\mathrm{rec}} \tau_d)^2\right), \tag{A.5}$$

where we assume $N \gg 1$. Using the definition of the thermal de-Broglie wavelength $\lambda_{dB} = \hbar \sqrt{2\pi / m k_B T}$, we attain the result in Eq. (2.14).

Inhomogeneous atomic density. We now study how an inhomogeneous atom density can lead to a decay of the retrieval efficiency as a function of dark time. We assume that the atomic density is only inhomogeneous along the propagation direction z of the signal light. Further, we assume that the incoming signal light pulse is rectangular and so long that it is never completely inside the medium. If we neglect absorption, the polariton flux $\Phi_{\mathrm{pol}} = \rho_{\mathrm{pol}}(z) v_{\mathrm{gr}}(z)$ is constant, even inside the medium. Here ρ_{pol} is the local polariton density and $v_{\mathrm{gr}}(z) = c/(1 + n_{\mathrm{gr}}(z))$ the local group velocity. The polariton density before storage is then given by

$$\rho_{\mathrm{pol}}(z) = \frac{\Phi_{\mathrm{pol}}}{c} (1 + n_{\mathrm{gr}}(z)). \tag{A.6}$$

Efficient storage is only possible if the polaritons have only a small electromagnetic component before storage. According to Eqs. (2.10) and (2.11), this is the case if $n_{\mathrm{gr}} \gg 1$. For simplicity we assume unity storage efficiency if $n_{\mathrm{gr}}(z) \geq 1$ and zero storage efficiency else. The polariton density after storage is then given by

$$\rho_{\mathrm{store}}(z) = \rho_{\mathrm{pol}}(z) \theta(n_{\mathrm{gr}}(z) - 1) \approx \frac{\Phi_{\mathrm{pol}}}{c} n_{\mathrm{gr}}(z) \theta(n_{\mathrm{gr}}(z) - 1), \tag{A.7}$$

where θ is the Heaviside function. In the last step, we assumed $n_{\mathrm{gr}}(z) \gg 1$. Since the group index before storage $n_{\mathrm{gr}}(z)$ is proportional to the atomic density $\varrho(z)$ (cf. Eq. (2.9)), the probability of creating a Rydberg excitation is proportional to $\varrho(z)$, as long as θ has value 1.

We now consider the situation where the Rydberg atoms experience a potential $\hbar \Delta_m(z) = \hbar \Delta_p \varrho(z)/\varrho_p$ due to collisions with ground state atoms. Here

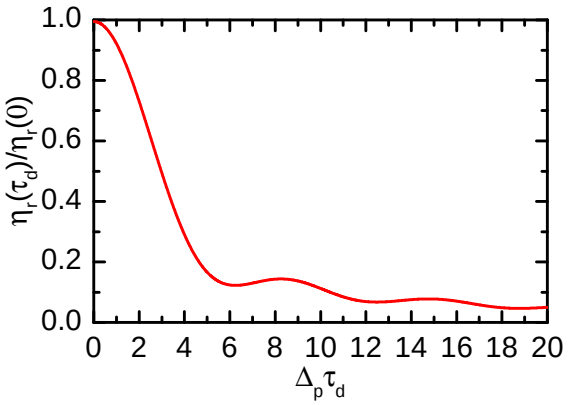

Figure A.1.: Dephasing due to a density-dependent energy shift of the Rydberg state according to Eq. (A.10). The retrieval efficiency decays to $1/e$ at $\Delta_p\tau_d = 3.57$.

$\Delta_p = 2\pi\hbar a\varrho_p/m_e$ is the potential depth (cf. Eq. (4.4)) which is proportional to the peak atomic density ϱ_p. Each term in the Dicke state $|D\rangle$ then picks up a phase factor $\exp(-i\Delta_m(z_j)\tau_d)$. Neglecting the recoil during storage, the time evolution of the Dicke state is given by

$$|D(\tau_d)\rangle = \frac{1}{\sqrt{N}}\sum_{i=1}^{N} e^{-i\Delta_m(z_j)\tau_d}|g_1, ..., r_j, ..., g_N\rangle. \tag{A.8}$$

According to Eq. (A.2), the retrieval efficiency after the dark time τ_d is given by

$$\eta_r = \left|\frac{1}{N}\sum_j e^{-i\Delta_m(z_j)\tau_d}\right|^2 \approx \left|\int d^3\boldsymbol{x}\ \frac{\varrho(z)}{N}\theta(n_{\rm gr}(z)-1)\ e^{-i\Delta_m(z)\tau_d}\right|^2. \tag{A.9}$$

Here we used a continuum approximation ($N \gg 1$) to replace the sum over all atoms by an integral weighted with the atomic density. In our model, the atomic density distribution along the z direction is given by a Gaussian with peak density ϱ_p and rms width σ_z. In x and y direction it is constant. If we assume that only one photon is stored in the cloud then the probability[2] to find a Rydberg excitation at position z is $\exp(-z^2/2\sigma_z^2)/\sqrt{2\pi}\sigma_z$.

Substituting $\tilde{z} = z/\sigma_z$ and abbreviating $g(\tilde{z}) = \exp(-\tilde{z}^2/2)/\sqrt{2\pi}$ yields

$$\eta_r = \left|\int d\tilde{z}\ g(\tilde{z})\ e^{-i\Delta_p\tau_d\sqrt{2\pi}g(\tilde{z})}\right|^2. \tag{A.10}$$

Note that integral in Eq. (A.10) does not depend on the rms width σ_z of the atomic cloud. The retrieval efficiency η_r is a function of only one parameter

[2]Since in typical experiments the peak group index is on the order of 10^6, the Heaviside function in Eq. (A.7) can be replaced by unity, because the integral (A.10) is dominated by the region where θ has value 1.

$\Delta_p \tau_d$. A numerical result for this function is shown in Fig. A.1. It reaches $1/e$ at $\Delta_p \tau_d = 3.57$. Hence the $1/e$ time τ_{dec} obeys

$$\frac{1}{\tau_{\mathrm{dec}}} = \frac{\Delta_p}{3.57} = \frac{2\pi\hbar a}{3.57 m_e}\, \varrho_p. \tag{A.11}$$

So this model predicts a linear dependence of the dephasing rate on the peak atomic density ϱ_p. As a matter of fact, this linear trend is fairly insensitive to many details of the model such as the assumption that the shape of the cloud is Gaussian.

The model predicts a slope of $1/\tau_{\mathrm{dec}}\varrho_p = 0.18\,\mu\mathrm{m}^3/\mu\mathrm{s}$, which, given the simplicity of the model, is in surprisingly good agreement with the experimental results in Chap. 4.4.

B. Angular Matrix Elements of the Dipole-Dipole Interaction

In this appendix the matrix elements of the dipole-dipole interaction as introduced in Sec. 2.2.4 are explicitly calculated. The procedure is similar to the one used in Ref. [129], where the dipole-dipole interaction is analysed in the fine-structure basis. Here the matrix elements are calculated for the product states $|n_A, l_A, j_A\rangle \otimes |n_B, l_B, j_B\rangle$. These matrix elements can be used to obtain matrix elements of bosonic symmetrised pair state (cf. Chap. 2.2.5). For a textbook on angular momentum algebra see e.g. Ref. [127].

In the coupled basis the two-atom state can be described by the total angular momentum of the atom pair J, its projection onto the z-axis M and the remaining quantum numbers $\gamma = n_A, l_A, j_A, s_A, n_B, l_B, j_B, s_B$, which are related to degrees of freedom of the individual atoms. Here $s = 1/2$ is the spin of the valence electron. In this basis the matrix elements of $T_q^{(2)}$ can be evaluated using the Wigner-Eckart theorem [127]

$$\langle \gamma', J', M' | T_q^{(k)} | \gamma, J, M \rangle = (-1)^{J'-M'} \begin{pmatrix} J' & k & J \\ -M' & q & M \end{pmatrix} (\gamma', J' || T^{(k)} || \gamma, J). \quad \text{(B.1)}$$

Here the matrix denotes a Wigner 3-J symbol and $(\gamma', J' || T^{(k)} || \gamma, J)$ a reduced matrix element. Since the tensors $d_A^{(1)}$ and $d_B^{(1)}$, which form the tensor product $T_q^{(2)}$, act on two different subsystems, the reduced matrix element is given by [127, Eq. (7.1.5)]

$$\begin{aligned}(\gamma', j_A', j_B', J', || T^{(k)} || \gamma, j_A, j_B, J) = (\gamma_A', j_A' || d_A^{(k_A)} || \gamma_A, j_A)\ (\gamma_B', j_B' || d_B^{(k_B)} || \gamma_B, j_B) \\ \times \sqrt{(2J+1)(2J'+1)(2k+1)} \begin{Bmatrix} j_A' & j_A & k_A \\ j_B' & j_B & k_B \\ J' & J & k \end{Bmatrix}. \quad \text{(B.2)}\end{aligned}$$

The curly brackets denote a 9-J symbol. For each subsystem the reduced matrix elements can be further factorised considering that the total angular momentum j is composed of an orbital angular momentum l and a spin s. The reduced matrix element can then be evaluated separately by [127, Eq. (7.1.7)]

$$\begin{aligned}(n', l', s, j' || d^{(k)} || n, l, s, j) = (-1)^{l'+s+j+k} \sqrt{(2j+1)(2j'+1)} \\ \times \begin{Bmatrix} l' & j' & s \\ j & l & k \end{Bmatrix} (n', l' || d^{(k)} || n, l), \quad \text{(B.3)}\end{aligned}$$

where the curly brackets denote a 6-J symbol. Finally, the reduced matrix element $(nl'||d^{(k)}||nl)$ can be expressed by [127, Eq. (5.4.5)]

$$(n', l'||d^{(k)}||n, l) = (-1)^{l'} \sqrt{(2l'+1)(2l+1)} \begin{pmatrix} l' & 1 & l \\ 0 & 0 & 0 \end{pmatrix} R_{n,l}^{n',l'} \tag{B.4}$$

with radial matrix element

$$R_{n,l}^{n',l'} = \int_0^\infty R_{n',l'}(r) r R_{n,l}(r) r^2 dr. \tag{B.5}$$

The radial matrix elements can be obtained by numerical integration of the wavefunction (cf. Chap. 2.2.2).

C. Rydberg Molecules

As discussed in Chap. 4.4, the presence of a ground state atom within the electronic wavefunction of the Rydberg state leads to s-wave scattering of the electron from the neutral atom. The interaction can be described by the pseudo-potential (4.3). In the limit of many ground state atoms, the perturbation of the electronic wave function can be treated in a mean field approach which results in an energy shift of the Rydberg state. In this appendix we study the opposite limit, where on average only one ground state atom resides within the classical radius of the Rydberg electron and the mean-field approximation fails.

Since the triplet scattering length $a_T = -16.1a_0$ is negative, the interaction is attractive and bound states between the Rydberg atom and a ground state atom are possible. The potential experienced by a ground state atom can be approximated by [170]

$$V(\boldsymbol{R}) = \frac{2\pi\hbar^2 a_T}{m_e}|\psi(\boldsymbol{R})|^2, \tag{C.1}$$

where m_e is the rest mass of the electron and $|\psi(\boldsymbol{R})|^2$ the probability to find the electron at position $\boldsymbol{R}$. These long range molecules were first observed for low principal quantum numbers using a spectroscopy technique based on laser excitation and field ionization [171]. Very recently, molecular resonances could also be observed for higher principal quantum numbers [172]. The measured binding energies are below $\sim h \times 2\,\mathrm{MHz}$ for $n \geq 50$ such that ultracold atomic gases are necessary to resolve them.

Indeed, these weakly bound Rydberg molecules can also be observed in storage and retrieval experiments similar to the one explained in Chap. 4.3. In the following experiments, the signal light drives the transition from $5S_{1/2}$, $F = 1$, $m_F = -1$ to $5P_{1/2}$, $F' = 2$, $m_{F'} = -2$. The control light is resonant with the transition from $5P_{1/2}$, $F = 2$ to the Rydberg state $nS_{1/2}$ and is σ^+ polarised. The density of the atoms is typically chosen such that approximately one ground state atom resides within the electronic wave function of the Rydberg state. For the $|60S_{1/2}\rangle$ state, for instance, a peak atomic density of $\varrho_p = 9.7 \times 10^{12}\,\mathrm{cm}^{-3}$ ($T = 0.35\,\mu\mathrm{K}$) is used. This yields ~ 0.8 atoms within the orbital radius of $0.27\,\mu\mathrm{m}$ (cf. Tab. 2.1). The incoming signal pulse typically contains $N_g \sim 4$ photons.

Fig. C.1(a) shows the retrieval efficiency as a function of dark time τ_d for $n = 60$. A high contrast oscillation with frequency $\omega_B/2\pi = 457 \pm 3\,\mathrm{kHz}$ is visible (red points). We attribute this oscillation to the excitation of Rydberg molecules where the oscillation frequency corresponds to the binding energy

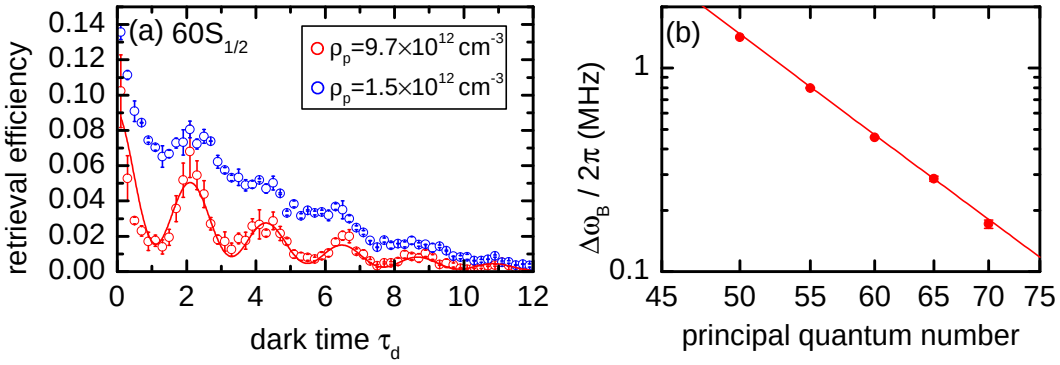

Figure C.1.: Excitation of Rydberg molecules. (a) The retrieval efficiency for storage in the $60S_{1/2}$ state (red data) shows an oscillatory behaviour which can be attributed to storage in a superposition of an atomic and a molecular state. At lower density (blue data) the Franck-Condon overlap for the excitation of two ground state atoms to a Rydberg molecule is reduced and the amplitude of the oscillation is much weaker. An empiric model is fitted to the data to extract the oscillation frequency (solid line). (b) The dependence of the oscillation frequency on the principal quantum number is shown as a double logarithmic plot. The solid line shows the fit of a power law $(n^*)^{-a}$ to the data.

$\hbar\omega_B$.[1]

The appearance of oscillations can be explained in the following way. The molecular state is red detuned from the atomic Rydberg state by its binding energy. If the EIT linewidth is larger than the binding energy then one part of the incoming signal photons is stored in the Rydberg state $|r\rangle$, another part is stored in the molecular state $|m\rangle$. Hence, in the Dicke state of Eq. (2.12) one has to replace $|r_j, g_k\rangle$ by $|c_{jk}\rangle = \cos\alpha|r_j, g_k\rangle + \sin\alpha|m_{jk}\rangle$ in each summand $|g_1, ..., r_j, ..., g_N\rangle$ and additionally sum over all $k \neq j$. Due to the binding energy, the time evolution of the state $|c_{jk}\rangle$ during the dark time τ_d is $|c_{jk}(\tau_d)\rangle = \cos\alpha|r_j, g_k\rangle + \sin\alpha\exp(-i\omega_B\tau_d)|m_{jk}\rangle$. Here, we choose the energy such that the internal state with exactly one Rydberg excitation has zero energy. Insertion into Eq. (A.2) yields the temporal evolution of the retrieval efficiency

$$\eta_r = |\langle c_{jk}(0)|c_{jk}(\tau_d)\rangle|^2 = \cos^4\alpha + \sin^4\alpha + 2\sin^2\alpha\cos^2\alpha\cos\omega_B\tau_d. \qquad \text{(C.2)}$$

Hence we expect that the retrieval efficiency oscillates with a frequency corresponding to the binding energy of the molecules.

According to Eq. (C.2), the visibility of the oscillation is reduced for smaller mixing angles α. In the experiment we can reduce the mixing angle by lowering

[1] Oscillations in the retrieval efficiency can also be caused by a misalignment between the magnetic field and the wave vector of the signal or control light [173]. In this case, the oscillation frequency would be proportional to the strength of the magnetic field B. We therefore check experimentally that the oscillation frequency does not depend on B by varying it between 0.2 and 1.2 G.

the atomic density because this reduces the Franck-Condon overlap for exciting two ground state atoms to a molecular state. The blue data points in Fig. C.1(a) are recorded at $\varrho_p = 1.5 \times 10^{12}\,\mathrm{cm}^{-3}$ and $T = 0.27\,\mu\mathrm{K}$, which yields ~ 0.1 atoms within the electronic wavefunction of the Rydberg atom. Indeed, the amplitude of the oscillation is strongly reduced.

Fig. C.1(b) shows how the oscillation frequency depends on the principal quantum number. For higher principal quantum numbers, the oscillation frequency decreases. Fitting a power law $(n^*)^a$ to the data we can extract the scaling behaviour with the effective principal quantum number n^*, which yields an exponent of $a = -6.01 \pm 0.13$. This is in fairly good agreement with the results in Ref. [172], where -6.26 ± 0.12 was measured. The absolute frequencies agree with an excitation of dimers in our experiments. Comparison with the spectroscopic data in Ref. [172] suggests that predominantly the first vibrational state of the molecules is addressed.

The particular strength of this spectroscopy method for Rydberg molecules is that the resolvable binding energies can be much smaller than, for example, the EIT linewidths, as all light fields are switched off during the dark time. Currently, the lowest detectable binding energy is given by decoherence.

D. Coherent Logic Gate for Light Pulses based on Storage in a BEC

As outlined in Chap. 1, Rydberg EIT is not the only possibility to create interactions between weak light pulses. An alternative strategy is to temporarily convert light pulses into atomic excitations. In atomic ensembles, this conversion can be achieved by storage of light techniques that are based on Raman transitions [174] or EIT. The atomic excitations can then interact with each other. Subsequently, the atomic excitations can be converted back to light. With regard to applicability of this strategy in quantum information applications, it is important to show that all involved processes, that means storage, interaction and retrieval, are coherent. One possible interaction mechanism for atomic excitations are s-wave collisions between pairs of ground-state atoms [65,66]. Based on this, the implementation of a photon-photon quantum gate in a Bose-Einstein condensate (BEC) was proposed in Ref. [66].

In the course of this thesis, experiments were performed that demonstrate the key ingredients of this proposal, namely the interaction between atomic excitations due the elastic collisions and the coherence of the overall process including the creation of the excitation and their conversion to light at the end. This appendix gives an overview over these experiments. They are explained in detail in the dissertation [106]. The results have been published in Ref. [67].

Fig. D.1(a) illustrates the experimental procedure for the implementation of a coherent logic gate. Signal light is stored in a BEC that is prepared in the atomic state $|1,\mathbf{0}\rangle$ with internal state $|1\rangle$ and wave vector $\mathbf{0}$. This is achieved with the help of a control field such that a Raman transition into a second ground state $|2\rangle$ is driven. The signal light is coherently stored in the atomic state $|2,\boldsymbol{k}\rangle$. The momentum $\hbar\boldsymbol{k}$ arises due to the recoil experienced by the atoms during the Raman transfer. A second signal pulse is applied in a different geometry and stored in the atomic state $|2,\boldsymbol{k}+\boldsymbol{q}\rangle$. After the preparation, the populations in the states $|1,\mathbf{0}\rangle$, $|2,\boldsymbol{k}\rangle$ and $|2,\boldsymbol{k}+\boldsymbol{q}\rangle$ are approximately equal.

During the following dark time of 0.4 ms, atomic four-wave mixing (FWM) takes place and a BEC in a new momentum component $|1,\boldsymbol{q}\rangle$ is created. The FWM can be intuitively understood as an atomic scattering process. An atom in state $|1,\mathbf{0}\rangle$ collides with an atom in state $|2,\boldsymbol{k}+\boldsymbol{q}\rangle$. The existing BEC in state $|2,\boldsymbol{k}\rangle$ creates bosonic enhancement for an atom to emerge in this state.

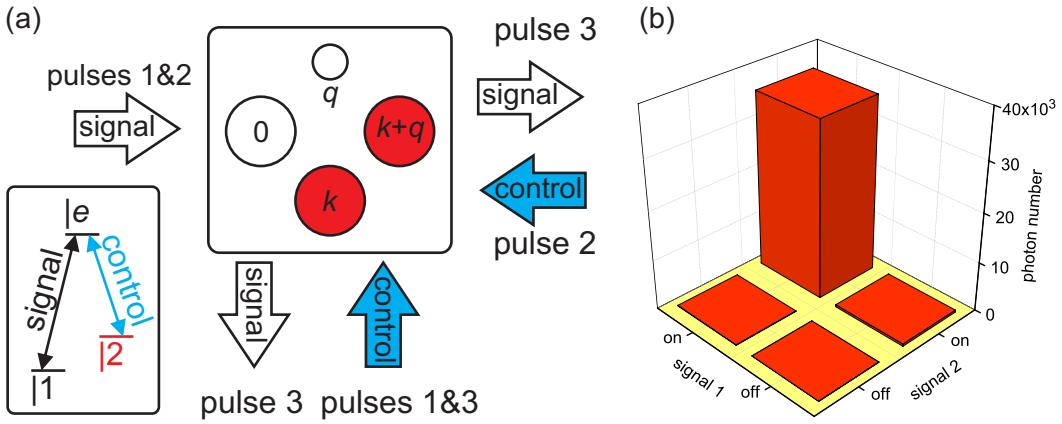

Figure D.1.: Logic gate based on atomic FWM. (a) Experimental scheme. Two Raman pulses are applied, preparing three BECs with momenta $\mathbf{0}$, $\boldsymbol{k}$ and $\boldsymbol{k}+\boldsymbol{q}$. During the subsequent dark time, atomic FWM creates a BEC with momentum $\boldsymbol{q}$. Arrows indicate the propagation direction of the light beams. Circles represent atomic momentum components. The internal states are colour coded: white denotes $|1\rangle$, red denotes $|2\rangle$. A third light pulse with only control light applied retrieves the signal light. The retrieved light will have a component propagating downward if FWM took place. (b) Logic gate. The retrieved photon number propagating downward is shown for four different experimental settings, in which the signal beams during Raman pulses 1 and 2 are turned on or off independently. This demonstrates an AND gate for classical light.

As a consequence of conservation of total momentum and total internal state energy for elastic scattering, the collisional parter is scattered into state $|1,\boldsymbol{q}\rangle$. Conservation of energy requires that the relation $\boldsymbol{k}\cdot\boldsymbol{q}\sim 0$ has to be fulfilled [175, 176]. This corresponds to phase-matching in optical FWM.

After the dark time, the atomic states are mapped back onto light fields. To this end, the BEC is illuminated by a control light pulse. Each atom in internal state $|2\rangle$ is transferred back into internal state $|1\rangle$ in a Raman process under emission of a photon. These Raman processes are bosonically stimulated by the two BECs in the states $|1,\mathbf{0}\rangle$ and $|1,\boldsymbol{q}\rangle$. The stimulated growth of atomic population in these two BEC is called Raman amplification of matter waves (AMW) [177, 178]. Along with the population growth in $|1,\mathbf{0}\rangle$ and $|1,\boldsymbol{q}\rangle$, signal light with two momentum components is emitted, one propagating downward, the other rightward (cf. Fig. D.1(a)).

The downward propagating component is only created if the state $|1,\boldsymbol{q}\rangle$ is populated. This is only possible if atomic FWM has occurred. FWM, however, only takes place if both signal pulses are applied during both Raman pulses. This can be used to realise an AND gate, where the two classical signal pulses are the input and signal light in the downward propagating component is the

output. The experimental results are shown in Fig. D.1(b).

From a theoretical point of view, Raman AMW is is analogous to a stimulated Raman process [178], except that the emission is bosonically stimulated not by application of a second laser beam but by the presence of a second BEC. Hence we expect, that Raman AMW generates light in a phase coherent way with the relative phase of the two BECs determining the phase of the emitted light.

We verify the phase coherence of the retrieved light by creating population in the momentum component $|2, \boldsymbol{k} - \boldsymbol{q}\rangle$. Raman AMW then also generates light from the BECs pair $|1, \mathbf{0}\rangle$ and $|2, \boldsymbol{k} - \boldsymbol{q}\rangle$ which is also emitted into the downward direction. The two light fields interfere on a detector and a beat note is observed which proves the coherence of all involved processes.

Bibliography

[1] J. Bardeen and W. Brattain. The transistor, a semi-conductor triode. *Phys. Rev.* **74**, 230–231 (1948).

[2] J. Haynes and W. Shockley. Investigation of hole injection in transistor action. *Phys. Rev.* **75**, 691–691 (1949).

[3] M. Riordan, L. Hoddeson, and C. Herring. The invention of the transistor. *Rev. Mod. Phys.* **71**, S336–S345 (1999).

[4] R. Landauer. Irreversibility and heat generation in the computing process. *IBM J. Res. Dev.* **5**, 183–191 (1961).

[5] C. H. Bennett. Notes on Landauer's principle, reversible computation, and Maxwell's Demon. *Stud. Hist. Philos. Sci. Part B* **34**, 501–510 (2003).

[6] A. Bérut, A. Arakelyan, A. Petrosyan, S. Ciliberto, R. Dillenschneider, and E. Lutz. Experimental verification of Landauer's principle linking information and thermodynamics. *Nature* **483**, 187–189 (2012).

[7] D. G. Feitelson, *Optical Computing: A Survey for Computer Scientists* (MIT Press, Cambridge, 1988).

[8] H. J. Caulfield and S. Dolev. Why future supercomputing requires optics. *Nat. Photonics* **4**, 261–263 (2010).

[9] K. Jain and G. W. Pratt. Optical transistor. *Appl. Phys. Lett.* **28**, 719 (1976).

[10] D. A. B. Miller. Are optical transistors the logical next step? *Nat. Photonics* **4**, 3–5 (2010).

[11] C. H. Bennett and G. Brassard, Quantum cryptography: Public key distribution and coin tossing, (In *Proc. IEEE Int. Conf. Comput. Syst. Signal Process.* New York, 1984) pp. 175–179.

[12] N. Gisin and R. Thew. Quantum communication. *Nat. Photonics* **1**, 165–171 (2007).

[13] H.-J. Briegel, W. Dür, J. Cirac, and P. Zoller. Quantum repeaters: The role of imperfect local operations in quantum communication. *Phys. Rev. Lett.* **81**, 5932–5935 (1998).

[14] T. D. Ladd, F. Jelezko, R. Laflamme, Y. Nakamura, C. Monroe, and J. L. O'Brien. Quantum computers. *Nature* **464**, 45–53 (2010).

[15] P. Shor, Algorithms for quantum computation: discrete logarithms and factoring, In *Proc. 35th Annu. Symp. Found. Comput. Sci.* IEEE Comput. Soc. Press, 1994, pp. 124–134.

[16] A. Ekert and R. Jozsa. Quantum computation and Shor's factoring algorithm. *Rev. Mod. Phys.* **68**, 733–753 (1996).

[17] L. K. Grover, B. Labs, M. Avenue, and M. Hill. Quantum mechanics helps in searching for a needle in a haystack. *Phys. Rev. Lett.* **79**, 325–328 (1997).

[18] D. P. DiVincenzo, *44th IFF Spring School 2013: Quantum Information Processing* (Forschungszentrum Jülich GmbH, Jülich, ISBN 978-3-89336-833-4, 2013).

[19] M. Saffman, T. G. Walker, and K. Mølmer. Quantum information with Rydberg atoms. *Rev. Mod. Phys.* **82**, 2313–2363 (2010).

[20] H. Haffner, C. Roos, and R. Blatt. Quantum computing with trapped ions. *Phys. Rep.* **469**, 155–203 (2008).

[21] F. A. Zwanenburg, A. S. Dzurak, A. Morello, M. Y. Simmons, L. C. L. Hollenberg, G. Klimeck, S. Rogge, S. N. Coppersmith, and M. A. Eriksson. Silicon quantum electronics. *Rev. Mod. Phys.* **85**, 961–1019 (2013).

[22] L. Childress and R. Hanson. Diamond NV centers for quantum computing and quantum networks. *MRS Bull.* **38**, 134–138 (2013).

[23] V. Dobrovitski, G. Fuchs, A. Falk, C. Santori, and D. Awschalom. Quantum control over single spins in diamond. *Annu. Rev. Condens. Matter Phys.* **4**, 23–50 (2013).

[24] J. A. Jones. Quantum computing with NMR. *Prog. Nucl. Magn. Reson. Spectrosc.* **59**, 91–120 (2011).

[25] M. H. Devoret and R. J. Schoelkopf. Superconducting circuits for quantum information: an outlook. *Science* **339**, 1169–74 (2013).

[26] D. Deutsch. Quantum theory, the Church-Turing principle and the universal quantum computer. *Proc. R. Soc. A* **400**, 97–117 (1985).

[27] M. A. Nielsen and I. L. Chuang, *Quantum Computation and Quantum Information* (University Press, Cambridge, 2000).

[28] M. W. Johnson, M. H. S. Amin, S. Gildert, T. Lanting, F. Hamze, N. Dickson, R. Harris, A. J. Berkley, J. Johansson, P. Bunyk, E. M. Chapple, C. Enderud, J. P. Hilton, K. Karimi, E. Ladizinsky, N. Ladizinsky, T. Oh, I. Perminov, C. Rich, M. C. Thom, E. Tolkacheva, C. J. S. Truncik, S. Uchaikin, J. Wang, B. Wilson, and G. Rose. Quantum annealing with manufactured spins. *Nature* **473**, 194–198 (2011).

[29] T. F. Rønnow, Z. Wang, J. Job, S. Boixo, S. V. Isakov, D. Wecker, J. M. Martinis, D. A. Lidar, and M. Troyer. Quantum computing. Defining and detecting quantum speedup. *Science* **345**, 420–424 (2014).

[30] J. L. O'Brien, A. Furusawa, and J. Vučković. Photonic quantum technologies. *Nat. Photonics* **3**, 687–695 (2009).

[31] T. Pittman, B. Jacobs, and J. Franson. Demonstration of nondeterministic quantum logic operations using linear optical elements. *Phys. Rev. Lett.* **88**, 257902 (2002).

[32] J. L. O'Brien, G. J. Pryde, a. G. White, T. C. Ralph, and D. Branning. Demonstration of an all-optical quantum controlled-NOT gate. *Nature* **426**, 264–267 (2003).

[33] S. Gasparoni, J.-W. Pan, P. Walther, T. Rudolph, and A. Zeilinger. Realization of a photonic controlled-NOT gate sufficient for quantum computation. *Phys. Rev. Lett.* **93**, 020504 (2004).

[34] K. Sanaka, T. Jennewein, J.-W. Pan, K. Resch, and A. Zeilinger. Experimental nonlinear sign shift for linear optics quantum computation. *Phys. Rev. Lett.* **92**, 017902 (2004).

[35] E. Knill, R. Laflamme, and G. J. Milburn. A scheme for efficient quantum computation with linear optics. *Nature* **409**, 46–52 (2001).

[36] D. Petrosyan. Towards deterministic optical quantum computation with coherently driven atomic ensembles. *J. Opt. B* **7**, S141–S151 (2005).

[37] P. Mandel, S. D. Smith, and B. S. Wherret, eds., *From Optical Bistability Towards Optical Computing* (Elsevier Science, Amsterdam, 1991).

[38] R. W. Munn and C. N. Ironside, eds., *Principals and Applications of Nonlinear Optical Materials* (Blackie Academic and Professional, Glasgow, 1993).

[39] N. Matsuda, R. Shimizu, Y. Mitsumori, H. Kosaka, and K. Edamatsu. Observation of optical-fibre Kerr nonlinearity at the single-photon level. *Nat. Photonics* **3**, 95–98 (2009).

[40] T. Guerreiro, E. Pomarico, B. Sanguinetti, N. Sangouard, J. S. Pelc, C. Langrock, M. M. Fejer, H. Zbinden, R. T. Thew, and N. Gisin. Interaction of independent single photons based on integrated nonlinear optics. *Nat. Commun.* **4**, 2324 (2013).

[41] R. Nissim, A. Pejkic, E. Myslivets, B. P. Kuo, N. Alic, and S. Radic. Ultrafast optical control by few photons in engineered fiber. *Science* **345**, 417–419 (2014).

[42] J. Hwang, M. Pototschnig, R. Lettow, G. Zumofen, A. Renn, S. Götzinger, and V. Sandoghdar. A single-molecule optical transistor. *Nature* **460**, 76–80 (2009).

[43] S. Haroche and J.-M. Raimond, *Exploring the Quantum* (Oxford University Press, Oxford, 2006).

[44] A. Reiserer, N. Kalb, G. Rempe, and S. Ritter. A quantum gate between a flying optical photon and a single trapped atom. *Nature* **508**, 237–240 (2014).

[45] T. G. Tiecke, J. D. Thompson, N. P. de Leon, L. R. Liu, V. Vuletić, and M. D. Lukin. Nanophotonic quantum phase switch with a single atom. *Nature* **508**, 241–244 (2014).

[46] I. Shomroni, S. Rosenblum, Y. Lovsky, O. Bechler, G. Guendelman, and B. Dayan. All-optical routing of single photons by a one-atom switch controlled by a single photon. *Science* **345**, 903–905 (2014).

[47] R. Bose, D. Sridharan, H. Kim, G. S. Solomon, and E. Waks. Low-photon-number optical switching with a single quantum dot coupled to a photonic crystal cavity. *Phys. Rev. Lett.* **108**, 227402 (2012).

[48] T. Volz, A. Reinhard, M. Winger, A. Badolato, K. J. Hennessy, E. L. Hu, and A. Imamoglu. Ultrafast all-optical switching by single photons. *Nat. Photonics* **6**, 607–611 (2012).

[49] V. Loo, C. Arnold, O. Gazzano, A. Lemaître, I. Sagnes, O. Krebs, P. Voisin, P. Senellart, and L. Lanco. Optical nonlinearity for few-photon pulses on a quantum dot-pillar cavity device. *Phys. Rev. Lett.* **109**, 166806 (2012).

[50] A. M. C. Dawes, L. Illing, S. M. Clark, and D. J. Gauthier. All-optical switching in rubidium vapor. *Science* **308**, 672–674 (2005).

[51] M. Fleischhauer, A. Imamoglu, and J. Marangos. Electromagnetically induced transparency: Optics in coherent media. *Rev. Mod. Phys.* **77**, 633–673 (2005).

[52] T. H. Hänsch, R. Keil, A. Schabert, C. Schmelzer, and P. Toschek. Interaction of laser light waves by dynamic Stark splitting. *Zeitschrift für Phys.* **226**, 293–296 (1969).

[53] P. E. Toschek, The emergence of electromagnetically induced transparency, In *Slow and Fast Light* (OSA, Washington D.C., DOI:10.1364/SL.2007.SMA3, 2007) p. SMA3.

[54] G. Alzetta, A. Gozzini, L. Moi, and G. Orriols. An experimental method for the observation of r.f. transitions and laser beat resonances in oriented Na vapour. *Nuovo Cim. B* **36**, 5–20 (1976).

[55] E. Arimondo. Coherent population trapping in laser spectroscopy. *Prog. Opt.* **35**, 259 (1996).

[56] K.-J. Boller, A. Imamoglu, and S. Harris. Observation of electromagnetically induced transparency. *Phys. Rev. Lett.* **66**, 2593–2596 (1991).

[57] S. E. Harris, J. E. Field, and A. Imamoglu. Nonlinear optical processes using electromagnetically induced transparency. *Phys. Rev. Lett.* **64**, 1107–1110 (1990).

[58] S. Harris and Y. Yamamoto. Photon switching by quantum interference. *Phys. Rev. Lett.* **81**, 3611–3614 (1998).

[59] H. Schmidt and A. Imamoglu. Giant Kerr nonlinearities obtained by electromagnetically induced transparency. *Opt. Lett.* **21**, 1936 (1996).

[60] M. D. Lukin and A. Imamoglu. Controlling photons using electromagnetically induced transparency. *Nature* **413**, 273–276 (2001).

[61] M. Bajcsy, S. Hofferberth, V. Balic, T. Peyronel, M. Hafezi, A. Zibrov, V. Vuletic, and M. Lukin. Efficient all-optical switching using slow light within a hollow fiber. *Phys. Rev. Lett.* **102**, 203902 (2009).

[62] L. V. Hau, S. E. Harris, Z. Dutton, and C. H. Behroozi. Light speed reduction to 17 metres per second in an ultracold atomic gas. *Nature* **397**, 594–598 (1999).

[63] M. Fleischhauer and M. Lukin. Dark-state polaritons in electromagnetically induced transparency. *Phys. Rev. Lett.* **84**, 5094–5097 (2000).

[64] C. Liu, Z. Dutton, C. H. Behroozi, and L. V. Hau. Observation of coherent optical information storage in an atomic medium using halted light pulses. *Nature* **409**, 490 (2001).

[65] M. Mašalas and M. Fleischhauer. Scattering of dark-state polaritons in optical lattices and quantum phase gate for photons. *Phys. Rev. A* **69**, 061801 (2004).

[66] A. Rispe, B. He, and C. Simon. Photon-photon gates in Bose-Einstein condensates. *Phys. Rev. Lett.* **107**, 043601 (2011).

[67] C. Vo, S. Riedl, S. Baur, G. Rempe, and S. Dürr. Coherent logic gate for light pulses based on storage in a Bose-Einstein condensate. *Phys. Rev. Lett.* **109**, 263602 (2012).

[68] W. Chen, K. M. Beck, R. Bücker, M. Gullans, M. D. Lukin, H. Tanji-Suzuki, and V. Vuletić. All-optical switch and transistor gated by one stored photon. *Science* **341**, 768–770 (2013).

[69] T. F. Gallagher, *Rydberg Atoms* (Cambridge University Press, Cambridge, 1994).

[70] D. Jaksch, J. Cirac, P. Zoller, S. Rolston, R. Cote, and M. Lukin. Fast quantum gates for neutral atoms. *Phys. Rev. Lett.* **85**, 2208–2211 (2000).

[71] M. D. Lukin, M. Fleischhauer, and R. Cote. Dipole blockade and quantum information processing in mesoscopic atomic ensembles. *Phys. Rev. Lett.* **87**, 037901 (2001).

[72] M. Saffman and T. Walker. Creating single-atom and single-photon sources from entangled atomic ensembles. *Phys. Rev. A* **66**, 065403 (2002).

[73] R. Unanyan and M. Fleischhauer. Efficient and robust entanglement generation in a many-particle system with resonant dipole-dipole interactions. *Phys. Rev. A* **66**, 032109 (2002).

[74] D. Møller, L. Madsen, and K. Mølmer. Quantum gates and multiparticle entanglement by Rydberg excitation blockade and adiabatic passage. *Phys. Rev. Lett.* **100**, 170504 (2008).

[75] M. Müller, I. Lesanovsky, H. Weimer, H. P. Büchler, and P. Zoller. Mesoscopic Rydberg gate based on electromagnetically induced transparency. *Phys. Rev. Lett.* **102**, 170502 (2009).

[76] M. Saffman. Efficient multiparticle entanglement via asymmetric Rydberg blockade. *Phys. Rev. Lett.* **102**, 240502 (2009).

[77] H. Weimer, M. Müller, I. Lesanovsky, P. Zoller, and H. P. Büchler. A Rydberg quantum simulator. *Nat. Phys.* **6**, 382–388 (2010).

[78] D. Tong, S. M. Farooqi, J. Stanojevic, S. Krishnan, Y. P. Zhang, R. Côté, E. E. Eyler, and P. L. Gould. Local blockade of Rydberg excitation in an ultracold gas. *Phys. Rev. Lett.* **93**, 063001 (2004).

[79] K. Singer, M. Reetz-Lamour, T. Amthor, L. G. Marcassa, and M. Weidemüller. Suppression of excitation and spectral broadening induced by interactions in a cold gas of Rydberg atoms. *Phys. Rev. Lett.* **93**, 163001 (2004).

[80] T. Liebisch, A. Reinhard, P. Berman, and G. Raithel. Atom counting statistics in ensembles of interacting Rydberg atoms. *Phys. Rev. Lett.* **95**, 253002 (2005).

[81] T. Liebisch, A. Reinhard, P. Berman, and G. Raithel. Erratum: Atom counting statistics in ensembles of interacting Rydberg atoms [Phys. Rev. Lett. 95, 253002 (2005)]. *Phys. Rev. Lett.* **98**, 109903 (2007).

[82] T. Vogt, M. Viteau, J. Zhao, A. Chotia, D. Comparat, and P. Pillet. Dipole blockade at Förster resonances in high resolution laser excitation of Rydberg states of Cesium atoms. *Phys. Rev. Lett.* **97**, 083003 (2006).

[83] R. Heidemann, U. Raitzsch, V. Bendkowsky, B. Butscher, R. Löw, L. Santos, and T. Pfau. Evidence for coherent collective Rydberg excitation in the strong blockade regime. *Phys. Rev. Lett.* **99**, 163601 (2007).

[84] T. Johnson, E. Urban, T. Henage, L. Isenhower, D. Yavuz, T. Walker, and M. Saffman. Rabi oscillations between ground and Rydberg states with dipole-dipole atomic interactions. *Phys. Rev. Lett.* **100**, 113003 (2008).

[85] M. Reetz-Lamour, T. Amthor, J. Deiglmayr, and M. Weidemüller. Rabi oscillations and excitation trapping in the coherent excitation of a mesoscopic frozen Rydberg gas. *Phys. Rev. Lett.* **100**, 253001 (2008).

[86] E. Urban, T. A. Johnson, T. Henage, L. Isenhower, D. D. Yavuz, T. G. Walker, and M. Saffman. Observation of Rydberg blockade between two atoms. *Nat. Phys.* **5**, 110–114 (2009).

[87] A. Gaëtan, Y. Miroshnychenko, T. Wilk, A. Chotia, M. Viteau, D. Comparat, P. Pillet, A. Browaeys, and P. Grangier. Observation of collective excitation of two individual atoms in the Rydberg blockade regime. *Nat. Phys.* **5**, 115–118 (2009).

[88] T. Wilk, A. Gaëtan, C. Evellin, J. Wolters, Y. Miroshnychenko, P. Grangier, and A. Browaeys. Entanglement of two individual neutral atoms using Rydberg blockade. *Phys. Rev. Lett.* **104**, 010502 (2010).

[89] L. Isenhower, E. Urban, X. L. Zhang, A. T. Gill, T. Henage, T. A. Johnson, T. G. Walker, and M. Saffman. Demonstration of a neutral atom controlled-NOT quantum gate. *Phys. Rev. Lett.* **104**, 10503 (2010).

[90] I. Friedler, D. Petrosyan, M. Fleischhauer, and G. Kurizki. Long-range interactions and entanglement of slow single-photon pulses. *Phys. Rev. A* **72**, 043803 (2005).

[91] E. Shahmoon, G. Kurizki, M. Fleischhauer, and D. Petrosyan. Strongly interacting photons in hollow-core waveguides. *Phys. Rev. A* **83**, 033806 (2011).

[92] A. V. Gorshkov, J. Otterbach, M. Fleischhauer, T. Pohl, and M. D. Lukin. Photon-photon interactions via Rydberg blockade. *Phys. Rev. Lett.* **107**, 133602 (2011).

[93] D. Paredes-Barato and C. S. Adams. All-optical quantum information processing using Rydberg gates. *Phys. Rev. Lett.* **112**, 040501 (2014).

[94] J. Otterbach, M. Moos, D. Muth, and M. Fleischhauer. Wigner crystallization of single photons in cold Rydberg ensembles. *Phys. Rev. Lett.* **111**, 113001 (2013).

[95] S. Sevinçli, N. Henkel, C. Ates, and T. Pohl. Nonlocal nonlinear optics in cold Rydberg gases. *Phys. Rev. Lett.* **107**, 153001 (2011).

[96] A. K. Mohapatra, T. R. Jackson, and C. S. Adams. Coherent optical detection of highly excited Rydberg states using electromagnetically induced transparency. *Phys. Rev. Lett.* **98**, 113003 (2007).

[97] J. D. Pritchard, D. Maxwell, A. Gauguet, K. J. Weatherill, M. P. A. Jones, and C. S. Adams. Cooperative atom-light interaction in a blockaded Rydberg ensemble. *Phys. Rev. Lett.* **105**, 193603 (2010).

[98] Y. O. Dudin and A. Kuzmich. Strongly interacting Rydberg excitations of a cold atomic gas. *Science* **336**, 887–889 (2012).

[99] T. Peyronel, O. Firstenberg, Q.-Y. Liang, S. Hofferberth, A. V. Gorshkov, T. Pohl, M. D. Lukin, and V. Vuletić. Quantum nonlinear optics with single photons enabled by strongly interacting atoms. *Nature* **488**, 57–60 (2012).

[100] D. Maxwell, D. Szwer, D. Paredes-Barato, H. Busche, J. Pritchard, A. Gauguet, K. Weatherill, M. Jones, and C. Adams. Storage and control of optical photons using Rydberg polaritons. *Phys. Rev. Lett.* **110**, 103001 (2013).

[101] L. Li, Y. O. Dudin, and A. Kuzmich. Entanglement between light and an optical atomic excitation. *Nature* **498**, 466–469 (2013).

[102] O. Firstenberg, T. Peyronel, Q.-Y. Liang, A. V. Gorshkov, M. D. Lukin, and V. Vuletić. Attractive photons in a quantum nonlinear medium. *Nature* **502**, 71–75 (2013).

[103] S. Baur, D. Tiarks, G. Rempe, and S. Dürr. Single-photon switch based on Rydberg blockade. *Phys. Rev. Lett.* **112**, 073901 (2014).

[104] D. Tiarks, S. Baur, K. Schneider, S. Dürr, and G. Rempe. Single-photon transistor using a Förster resonance. *Phys. Rev. Lett.* **113**, 053602 (2014).

[105] W. K. Wootters and W. H. Zurek. A single quantum cannot be cloned. *Nature* **299**, 802–803 (1982).

[106] C. Vo, *Logikgatter für Lichtpulse basierend auf atomarer Vierwellenmischung in einem Bose-Einstein-Kondensat*, PhD thesis, Max-Planck-Institut für Quantenoptik, Garching and Technische Universität München (2012).

[107] M. G. Lettner, *Ein Bose-Einstein-Kondensat als Quantenspeicher für Zwei-Teilchen-Verschränkung*, PhD thesis, Max-Planck-Institut für Quantenoptik, Garching and Technische Universität München (2011).

[108] J. Gea-Banacloche, Y.-q. Li, S.-z. Jin, and M. Xiao. Electromagnetically induced transparency in ladder-type inhomogeneously broadened media: Theory and experiment. *Phys. Rev. A* **51**, 576–584 (1995).

[109] R. Dicke. Coherence in spontaneous radiation processes. *Phys. Rev.* **93**, 99–110 (1954).

[110] M. Fleischhauer and M. Lukin. Quantum memory for photons: Dark-state polaritons. *Phys. Rev. A* **65**, 22314 (2002).

[111] A. Gorshkov, A. André, M. Lukin, and A. Sørensen. Photon storage in Λ-type optically dense atomic media. I. Cavity model. *Phys. Rev. A* **76**, 033804 (2007).

[112] A. Gorshkov, A. André, M. Lukin, and A. Sørensen. Photon storage in Λ-type optically dense atomic media. II. Free-space model. *Phys. Rev. A* **76**, 033805 (2007).

[113] M. Naraschewski and R. Glauber. Spatial coherence and density correlations of trapped Bose gases. *Phys. Rev. A* **59**, 4595–4607 (1999).

[114] H. A. Bethe and E. E. Salpeter, *Quantum Mechanics of One- and Two-Electron Atoms* (Plenum Publishing Corp., New York, 1977).

[115] W. C. Martin. Series formulas for the spectrum of atomic sodium (NaI). *J. Opt. Soc. Am.* **70**, 784–788 (1980).

[116] W. Li, I. Mourachko, M. Noel, and T. Gallagher. Millimeter-wave spectroscopy of cold Rb Rydberg atoms in a magneto-optical trap: Quantum defects of the ns, np, and nd series. *Phys. Rev. A* **67**, 052502 (2003).

[117] J. Han, Y. Jamil, D. Norum, P. Tanner, and T. Gallagher. Rb nf quantum defects from millimeter-wave spectroscopy of cold ^{85}Rb Rydberg atoms. *Phys. Rev. A* **74**, 054502 (2006).

[118] K. Afrousheh, P. Bohlouli-Zanjani, J. Petrus, and J. Martin. Determination of the ^{85}Rb ng-series quantum defect by electric-field-induced resonant energy transfer between cold Rydberg atoms. *Phys. Rev. A* **74**, 062712 (2006).

[119] T. F. Gallagher. Rydberg atoms. *Rep. Prog. Phys.* **51**, 143–188 (1988).

[120] I. Beterov, I. Ryabtsev, D. Tretyakov, and V. Entin. Quasiclassical calculations of blackbody-radiation-induced depopulation rates and effective lifetimes of Rydberg nS, nP, and nD alkali-metal atoms with n$\leq$80. *Phys. Rev. A* **79**, 052504 (2009).

[121] M. S. Sullivan and B. P. Stoicheff. Scalar polarizabilities and avoided crossings of high Rydberg states in Rb. *Phys. Rev. A* **31**, 2718–2720 (1985).

[122] K. Singer, J. Stanojevic, M. Weidemüller, and R. Côté. Long-range interactions between alkali Rydberg atom pairs correlated to the ns-ns, np-np and nd-nd asymptotes. *J. Phys. B* **38**, 295–307 (2005).

[123] M. Marinescu, H. Sadeghpour, and A. Dalgarno. Dispersion coefficients for alkali-metal dimers. *Phys. Rev. A* **49**, 982–988 (1994).

[124] S. Bhatti, C. Cromer, and W. Cooke. Analysis of the Rydberg character of the 5d7d$^1D_2$ state of barium. *Phys. Rev. A* **24**, 161–165 (1981).

[125] B. Numerov. A method of extrapolation of perturbations. *Mon. Not. R. Astron. Soc.* **84**, 592 (1924).

[126] L. Zimmerman, M. G. Littman, M. M. Kash, and D. Kleppner. Stark structure of the Rydberg states of alkali-metal atoms. *Phys. Rev. A* **20**, 2251–2275 (1979).

[127] A. E. Edmonds, *Angular Momentum in Quantum Mechanics* (Princeton Universtiy Press, Princeton, 1974) 3 ed.

[128] F. Schwabl, *Quantenmechanik für Fortgeschrittene* (Springer, Berlin Heidelberg New York, 2005) 4 ed.

[129] T. Walker and M. Saffman. Consequences of Zeeman degeneracy for the van der Waals blockade between Rydberg atoms. *Phys. Rev. A* **77**, 032723 (2008).

[130] G. Cario and J. Franck. Über Zerlegung von Wasserstoffatomen durch angeregte Quecksilberatome. *Zeitschrift für Phys.* **11**, 161–166 (1922).

[131] T. Förster. Zwischenmolekulare Energiewanderung und Fluoreszenz. *Ann. Phys.* **437**, 55–75 (1948).

[132] A. Derevianko, W. Johnson, M. Safronova, and J. Babb. High-precision calculations of dispersion coefficients, static dipole polarizabilities, and atom-wall interaction constants for alkali-metal atoms. *Phys. Rev. Lett.* **82**, 3589–3592 (1999).

[133] J. Schuster, *Stoßlawinen in einem Bose-Einstein-Kondensat*, PhD thesis, Max-Planck-Institut für Quantenoptik, Garching and Technische Universität München (2002).

[134] A. Marte, *Feshbach-Resonanzen bei Stößen ultrakalter Rubidiumatome*, PhD thesis, Max-Planck-Institut für Quantenoptik, Garching and Technische Universität München (2003).

[135] T. Volz, *Ultracold Rubidium Molecules*, PhD thesis, Max-Planck-Institut für Quantenoptik, Garching, and Technische Universität München (2007).

[136] N. Syassen, *Interacting Feshbach Molecules*, PhD thesis, Max-Planck-Institut für Quantenoptik, Garching and Technische Universität München (2008).

[137] D. M. Bauer, *Optical Control of a Magnetic Feshbach Resonance*, PhD thesis, Max-Planck-Institut für Quantenoptik, Garching and Technische Universität München (2009).

[138] H. J. Metcalf and P. Van der Straten, *Laser Cooling and Trapping* (Springer, Heidelberg, 1999).

[139] D. E. Pritchard. Cooling neutral atoms in a magnetic trap for precision spectroscopy. *Phys. Rev. Lett.* **51**, 1336 (1983).

[140] C. J. Pethick and H. Smith, *Bose-Einstein Condensation in Dilute Gases* (Cambridge University Press, Cambridge, 2002).

[141] R. Grimm, M. Weidemüller, and Y. B. Ovchinnikov. Optical dipole traps for neutral atoms. *Adv. At. Mol. Opt. Phys.* **42**, 95–170 (2000).

[142] S. Dutta, J. Guest, D. Feldbaum, A. Walz-Flannigan, and G. Raithel. Ponderomotive optical lattice for Rydberg atoms. *Phys. Rev. Lett.* **85**, 5551–5554 (2000).

[143] M. Saffman and T. Walker. Analysis of a quantum logic device based on dipole-dipole interactions of optically trapped Rydberg atoms. *Phys. Rev. A* **72**, 022347 (2005).

[144] R. P. Abel, A. K. Mohapatra, M. G. Bason, J. D. Pritchard, K. J. Weatherill, U. Raitzsch, and C. S. Adams. Laser frequency stabilization to excited state transitions using electromagnetically induced transparency in a cascade system. *Appl. Phys. Lett.* **94**, 071107 (2009).

[145] R. W. P. Drever, J. L. Hall, F. V. Kowalski, J. Hough, G. M. Ford, A. J. Munley, and H. Ward. Laser phase and frequency stabilization using an optical resonator. *Appl. Phys. B* **31**, 97–105 (1983).

[146] E. D. Black. An introduction to Pound-Drever-Hall laser frequency stabilization. *Am. J. Phys.* **69**, 79 (2001).

[147] U. Schünemann, H. Engler, R. Grimm, M. Weidemüller, and M. Zielonkowski. Simple scheme for tunable frequency offset locking of two lasers. *Rev. Sci. Instrum.* **70**, 242 (1999).

[148] E. Amaldi and E. Segre. Effect of pressure on high terms of alkaline spectra. *Nature* **133**, 141 (1934).

[149] E. Fermi. Sopra lo spostamento per pressione delle righe elevate delle serie spettrali. *Nuovo Cim.* **11**, 157–166 (1934).

[150] C. Bahrim, U. Thumm, and I. I. Fabrikant. $^3S^e$ and $^1S^e$ scattering lengths for e-+ Rb, Cs and Fr collisions. *J. Phys. B* **34**, L195–L201 (2001).

[151] J. B. Balewski, A. T. Krupp, A. Gaj, D. Peter, H. P. Büchler, R. Löw, S. Hofferberth, and T. Pfau. Coupling a single electron to a Bose-Einstein condensate. *Nature* **502**, 664–667 (2013).

[152] K. Schneider, *Ein Einzel-Photon-Transistor basierend auf Rydberg-Blockade*, Master's thesis, Technische Universität München (2014).

[153] A. Kumar, B. Saha, C. Weatherford, and S. Verma. A systematic study of Hornbeck Molnar ionization involving Rydberg alkali atoms. *J. Mol. Struct. THEOCHEM* **487**, 1–9 (1999).

[154] L. Barbier, M. Djerad, and M. Chéret. Collisional ion-pair formation in an excited alkali-metal vapor. *Phys. Rev. A* **34**, 2710–2718 (1986).

[155] A. Reinhard, K. Younge, T. Liebisch, B. Knuffman, P. Berman, and G. Raithel. Double-Resonance Spectroscopy of Interacting Rydberg-Atom Systems. *Phys. Rev. Lett.* **100**, 233201 (2008).

[156] I. I. Ryabtsev, D. B. Tretyakov, I. I. Beterov, and V. M. Entin. Observation of the Stark-tuned Förster resonance between two Rydberg atoms. *Phys. Rev. Lett.* **104**, 073003 (2010).

[157] J. Nipper, J. B. Balewski, A. T. Krupp, B. Butscher, R. Löw, and T. Pfau. Highly resolved measurements of Stark-tuned Förster resonances between Rydberg atoms. *Phys. Rev. Lett.* **108**, 113001 (2012).

[158] J. Bochmann, M. Mücke, C. Guhl, S. Ritter, G. Rempe, and D. L. Moehring. Lossless state detection of single neutral atoms. *Phys. Rev. Lett.* **104**, 203601 (2010).

[159] M. J. Holland, M. J. Collett, and D. F. Walls. Nonideal quantum nondemolition measurements. *Phys. Rev. A* **42**, 2995–3005 (1990).

[160] O. Mülken, A. Blumen, T. Amthor, C. Giese, M. Reetz-Lamour, and M. Weidemüller. Survival probabilities in coherent exciton transfer with trapping. *Phys. Rev. Lett.* **99**, 090601 (2007).

[161] B. Olmos, W. Li, S. Hofferberth, and I. Lesanovsky. Amplifying single impurities immersed in a gas of ultracold atoms. *Phys. Rev. A* **84**, 041607 (2011).

[162] G. Günter, M. Robert-de Saint-Vincent, H. Schempp, C. S. Hofmann, S. Whitlock, and M. Weidemüller. Interaction enhanced imaging of individual Rydberg atoms in dense gases. *Phys. Rev. Lett.* **108**, 013002 (2012).

[163] G. Günter, H. Schempp, M. Robert-de Saint-Vincent, V. Gavryusev, S. Helmrich, C. S. Hofmann, S. Whitlock, and M. Weidemüller. Observing the dynamics of dipole-mediated energy transport by interaction-enhanced imaging. *Science* **342**, 954–956 (2013).

[164] A. I. Lvovsky, B. C. Sanders, and W. Tittel. Optical quantum memory. *Nat. Photonics* **3**, 706–714 (2009).

[165] Y.-H. Chen, M.-J. Lee, I.-C. Wang, S. Du, Y.-F. Chen, Y.-C. Chen, and I. Yu. Coherent optical memory with high storage efficiency and large fractional Delay. *Phys. Rev. Lett.* **110**, 083601 (2013).

[166] A. Reiserer, S. Ritter, and G. Rempe. Nondestructive detection of an optical photon. *Science* **342**, 1349–1351 (2013).

[167] K. Gheri and H. Ritsch. Single-atom quantum gate for light. *Phys. Rev. A* **56**, 3187–3190 (1997).

[168] V. Parigi, E. Bimbard, J. Stanojevic, A. J. Hilliard, F. Nogrette, R. Tualle-Brouri, A. Ourjoumtsev, and P. Grangier. Observation and measurement of interaction-induced dispersive optical nonlinearities in an ensemble of cold Rydberg atoms. *Phys. Rev. Lett.* **109**, 233602 (2012).

[169] B. He, A. V. Sharypov, J. Sheng, C. Simon, and M. Xiao. Two-photon dynamics in coherent Rydberg atomic ensemble. *Phys. Rev. Lett.* **112**, 133606 (2014).

[170] C. Greene, A. Dickinson, and H. Sadeghpour. Creation of polar and non-polar ultra-long-range Rydberg molecules. *Phys. Rev. Lett.* **85**, 2458–2461 (2000).

[171] V. Bendkowsky, B. Butscher, J. Nipper, J. P. Shaffer, R. Löw, and T. Pfau. Observation of ultralong-range Rydberg molecules. *Nature* **458**, 1005–1008 (2009).

[172] A. Gaj, A. T. Krupp, J. B. Balewski, R. Löw, S. Hofferberth, and T. Pfau. From molecular spectra to a density shift in dense Rydberg gases. *Nat. Commun.* **5**, 4546 (2014).

[173] D. Matsukevich, T. Chanelière, S. Jenkins, S.-Y. Lan, T. Kennedy, and A. Kuzmich. Observation of dark state polariton collapses and revivals. *Phys. Rev. Lett.* **96**, 33601 (2006).

[174] K. F. Reim, J. Nunn, V. O. Lorenz, B. J. Sussman, K. C. Lee, N. K. Langford, D. Jaksch, and I. A. Walmsley. Towards high-speed optical quantum memories. *Nat. Photonics* **4**, 218–221 (2010).

[175] L. Deng, E. W. Hagley, J. Wen, and M. Trippenbach. Four-wave mixing with matter waves. *Nature* **398**, 218–220 (1999).

[176] M. Trippenbach, Y. B. Band, and P. S. Julienne. Theory of four-wave mixing of matter waves from a Bose-Einstein condensate. *Phys. Rev. A* **62**, 023608 (2000).

[177] D. Schneble, G. Campbell, E. Streed, M. Boyd, D. Pritchard, and W. Ketterle. Raman amplification of matter waves. *Phys. Rev. A* **69**, 041601 (2004).

[178] M. Cola and N. Piovella. Theory of collective Raman scattering from a Bose-Einstein condensate. *Phys. Rev. A* **70**, 045601 (2004).

Publications

- Ein Photon schaltet einen optischen Transistor
  S. Baur
  Physik in unserer Zeit. (in press)

- Single-photon transistor using a Förster resonance.
  D. Tiarks, S. Baur, K. Schneider, S. Dürr, and G. Rempe.
  Physical Review Letters **113**, 053602 (2014)

- Single-photon switch based on Rydberg blockade.
  S. Baur, D. Tiarks, G. Rempe, and S. Dürr.
  Physical Review Letters **112**, 073901 (2014).

- Coherent logic gate for light pulses based on storage in a Bose-Einstein condensate.
  C. Vo, S. Riedl, S. Baur, G. Rempe, and S. Dürr.
  Physical Review Letters **109**, 263602 (2012).

Acknowledgments

This thesis would not have been possible without the help and support of many people only some of whom it is possible to thank here.

First and foremost, I would like to thank my supervisor Prof. Dr. Gerhard Rempe for providing me with the opportunity to work in his excellent research group. He cultivated a relaxed yet stimulating environment which was a pleasure to work in. He also allowed me a lot of freedom in my work and encouraged independent thought. Finally, I want to thank him for his continuous and inspiring scientific contributions, and for supporting me and our work in every respect.

I am deeply grateful to our senior scientist at the BEC experiment PD Dr. Stephan Dürr. He has always been an inspiring partner in discussions and I very much appreciate his talent for explaining complex problems clearly and his outstanding pedagogical skills. In particular, he contributed significantly to the development of the theoretical models. I would also like to thank him for proof reading this thesis and giving valuable suggestions for improvements.

Running the experiment would not have been possible without the support of the whole BEC team. I would like to thank Daniel Tiarks for his constant effort during the past two years, in particular during many long days and nights of endless measurements. I would also like to acknowledge the contributions of my predecessor Chris Vo and our postdoc Stefan Riedl at the beginning of this thesis. In addition I would like to thank the Masters students Dominik Fauser, with whom I observed the first tiny Rydberg EIT signals in our apparatus, and Katharina Schneider, with whom I investigated and improved many details of the experiment. I also enjoyed working with our lab students Moritz Müller, Alexander Prehn and Giovanni Girelli who were a breath of fresh air in the lab.

For their invaluable moral support and maintaining BEC social traditions I am eternally grateful to Dr. Matthias Lettner who introduced me to the experiment as a Masters student and Dr. Dominik Bauer. I also very much appreciated the conversations I had with Dr. Stephan Ritter.

Moreover, I thank all members of the Quantum Dynamics Group. In particular I would like to thank our technicians Helmut Stehbeck, Franz Denk, Sepp Bayerl, Thomas Wiesmeier and Tobias Urban, whose professional support was essential for running such a complex experiment. I am indebted to our secretaries Iris Schwaiger and Odette Gori who coordinated an occasionally chaotic environment with such skill. In addition, I would like to thank Andreas Widhopf and Bernhard Neugebauer who ensured that the air conditioning ran reliably.

I would also like to thank Andi with whom I went from the first exercise sheet

at university over the Kazakh steppe and the mountains of the Caucasus and back into neighbouring labs. I am grateful for his many years of friendship.

Last but not least I would like thank my family for the constant support and encouragement throughout this thesis. In particular, I would like thank Siona not only for proofreading this thesis but more importantly for the joyful time outside the lab which helped me to get over any setbacks in the lab very quickly.